Time-Varying Small Antennas for Wideband Applications

MOHSEN SALEHI

Dissertation submitted to the faculty of the Virginia Polytechnic Institute and State University in partial fulfillment of the requirements for the degree of

Doctor of Philosophy
in
Electrical Engineering

Majid Manteghi, Chair
William A. Davis
Gary S. Brown
Ahmad Safaai-Jazi
Werner E. Kohler

NOVEMBER 22, 2013
BLACKSBURG, VIRGINIA

KEYWORDS: Antenna, Direct Modulation, Quality Factor, Small Antenna, Switched Antenna, Switched Resonator, Time Domain, Transient, Wideband

Time-Varying Small Antennas for Wideband Applications

MOHSEN SALEHI

ABSTRACT

A desirable goal in wireless communication systems is to achieve a high-rate data transmission through electrically small antennas. However, the overall transmission bandwidth is limited by the antenna size. As a well-known physical limitation, maximum achievable bandwidth of a small antenna is governed by the fundamental limit which defines a lower bound on the antenna quality factor. This limit is a function of electrical size of the antenna and therefore, as the antenna shrinks in size the bandwidth decreases as well. This dissertation presents a new technique to decouple the impedance bandwidth of a high-Q antenna from the information bandwidth in order to provide a wideband data-transmission. This technique controls the natural resonant frequencies of an electrically small antenna in a time-varying fashion such that ultra-fast frequency-shift keying modulation can be achieved regardless of the narrow bandwidth of the antenna. A major advantage of the proposed technique is that the high-Q property of a miniaturized antenna is a desirable design parameter rather than a limiting factor. Therefore, the antenna size can be reduced as much as required. It is shown that if the fundamental resonance of an antenna is shifted in time, the frequency of the near-zone fields which construct the reactive stored energy, changes momentarily and hence, the radiating fields track any instantaneous variation of the antenna fundamental resonance. This characteristic is utilized to employ a single-mode high-Q antenna in the transient state and modulate the fundamental resonant frequency according to the baseband data information. This approach leads to a new class of compact transmitters with a minimized architecture and high data-rate transmission capability.

Acknowledgements

I am grateful to all the people who encouraged and supported me throughout my academic life. I have a number of individuals to thank for helping me to pursue my PhD. I would like to express my sincere gratitude to my advisor, Dr. Majid Manteghi who helped and guided me throughout my dissertation and gladly offered his knowledge and experience when needed. His trust and support was truly encouraging and helpful.

I would also like to express my special thanks and highest appreciation to Dr. William A. Davis for his generous help, keen insight and for everything he has taught me during the past years.

I would like to thank all the other members of my advisory committee; Dr. Gary S. Brown, Dr. Ahmad Safaai-Jazi and Dr. Werner E. Kohler for their support. I am especially grateful to Dr. Brown and Dr. Safaai-Jazi for the significant contribution they have made in improving my scientific knowledge and I am really thankful for all that I have learned from them.

I would like to thank my colleagues in the Electrical Engineering Department at Virginia Tech, and especially my friends in the Virginia Tech Antenna Group for their plentiful cooperation and all the fun we had together in the last few years.

Finally, I would like to thank my father, mother, brother, and my lovely wife for always standing beside me and providing me with all the support needed to complete my studies.

TABLE OF CONTENTS

LIST OF FIGURES

LIST OF TABLES

Chapter 1

Introduction

1.1 Motivation & Essence of the work

Small antennas with optimized radiation efficiency and bandwidth have remarkable demands in wireless communications. However, it is well-known that small size, high radiation efficiency and wide bandwidth are in contradiction [1, 2]. In other words, these three parameters cannot be optimized simultaneously and a trade-off must be considered. Classical theory of fundamental limit has been extensively studied and it's been generally referred to as Chu's theory [2]. This limit is independent of antenna type and defines a hard bound on the antenna size versus performance. Fundamentally, the maximum achievable bandwidth of an antenna with 100% efficiency is dictated by its size. Therefore, one can reduce the antenna radiation efficiency in order to increase the bandwidth, while maintaining the same size. However, the fundamental limit is based on linear time-invariant (LTI) radiating structures. Consequently, any optimization technique to improve the performance of an LTI antenna with a given size fundamentally cannot extend beyond the physical limit.

In wireless communication systems, the bandwidth is a critical design parameter as the rate of data transmission is limited by the system bandwidth. In addition, it is desirable to shrink the overall system architecture in size, including the antenna. As a result, substantial size reduction along with increased data-rate capacity has been a growing trend in wireless system designs. In applications such as implantable biomedical devices, particularly in devices that interact with nervous systems, it is essential to minimize the antenna size while implementing a wideband transmission capability. Therefore, designing optimized wireless communication systems has drawn a great deal of attention and become a high-demand technology.

This research presents a new technique beyond all conventional approaches proposed in the literature which are mainly focused on different strategies to use the available volume in a most efficient way to realize an ultra-wideband and compact radiator. As a figure-of-merit, all efforts have been carried out to approach Chu's limit and create an efficient radiation mechanism with the widest possible bandwidth according to the fundamental limit. Therefore, an ideal antenna would be a single-mode TM_{01} radiator which uses the entire occupied volume to radiate the available power rather than storing the reactive energy [3]. The traditional definition of impedance bandwidth is based on the amount of reflection at the input terminal of the antenna at different frequencies. This bandwidth is static and the antenna is treated as a single-port (or multi-port) LTI unit. Although tunable antennas are widely used to tune the antenna to the desirable frequency, the bandwidth is still limited by the antenna geometry and size.

The present study uses a time-varying configuration to relocate the antenna poles and modulate its resonant frequency. A switching reactive load, e. g. a capacitor is utilized to change the fundamental natural resonance of the antenna in a way that the amount of stored energy is not disturbed significantly and therefore, the high amount of stored energy in a high-Q antenna is not a limiting factor as the transmitting frequency changes. It is shown that for a high-Q antenna, variation of antenna poles results in simultaneous variation of frequency of the radiated power and hence, the radiation bandwidth is decoupled from the conventional impedance bandwidth. The switching signal is controlled by a sequence of digital data and at each switching state, one bit is transmitted. Theoretically, this configuration allows increasing the bit-rate up to the lower carrier frequency such that a single cycle represents a single bit. This bit-rate will be totally independent from the impedance bandwidth of the antenna and as a result, the narrowband properties of small antennas do not restrict the data rate. Furthermore, since each resonance requires an initial condition to be excited, the need for generating two separate RF signals using VCO is avoided and the antenna can be employed in the transient mode. Interestingly, this technique benefits from a high-Q value which is avoided in a traditional design. Therefore, the antenna can be as small as required without suffering from a limited data-rate.

1.2 Background

1.2.1 Fundamental Limit

The concept of fundamental limits was first investigated by Wheeler [4]. Later, Chu [5] provided an approximate expression with a circuit model. He developed a relationship between the antenna size and its quality factor, Q. The size of an antenna is defined by a sphere with minimum radius, a, which encloses the antenna as shown in Figure 1.1. $k = 2\pi/\lambda_0$ is the free space wave number associated with the radiated or received field. Chu's fundamental limit is given by

$$Q_{Chu} = \frac{1+2k^2a^2}{k^3a^3\left(1+k^2a^2\right)}, \tag{1.1}$$

where Q is the antenna quality factor. This equation directly relates the electrical size of the antenna with its minimum Q. The quality factor, Q, is related to the radiation efficiency, η, and bandwidth, BW, as [3]

$$Q = \eta \frac{VSWR-1}{2BW_{VSWR}\sqrt{VSWR}}. \tag{1.2}$$

Hence, for a 3-dB bandwidth where $VSWR = \left.\frac{1+|\rho|}{1-|\rho|}\right|_{|\rho|=\frac{1}{\sqrt{2}}}$, the minimum Q can be expressed as

$$Q = \eta \frac{1}{BW_{3dB}}. \tag{1.3}$$

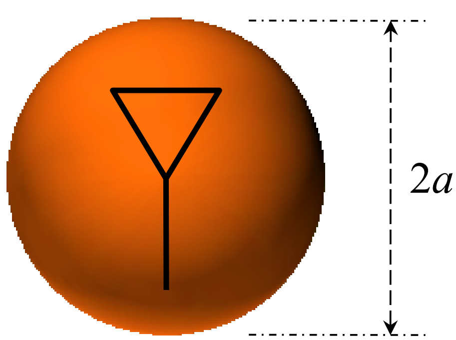

Figure 1.1: Antenna enclosing sphere with radius a.

In parallel with these efforts, Fano [6] and Tanner [7] developed theoretical limitations on the broadband impedance matching. Harrington published his works on the fundamental limits on the gain and bandwidth of directional antennas [8, 9]. Collin developed the fundamental limits based on an evanescent energy concept [10]. Fante extended Collin's work for TE and TM cases [11-14]. There are other researches on the fundamental limits as a continuation of previous investigations [15-18] to enhance Chu's limits and relate it to the theoretical limits of impedance matching. McLean [19] re-examined the approximate Chu's fundamental limits and derived a more accurate form as

$$Q_{McLean} = \frac{1}{(ka)^3} + \frac{1}{ka}. \tag{1.4}$$

Recently in 2011, the exact relation for minimum radiation Q was derived by Davis *et al* of the Virginia Tech Antenna Group (VTAG), as [20]

$$Q_{VTAG} = \frac{1}{(ka)^3}. \tag{1.5}$$

McLean's efforts triggered a new generation of research on the fundamental limits [21-32]. Fundamental limits, based on any of above theories, relate the electrical size of the antenna, *ka*, directly to the quality factor, Q. The antenna characteristics (such as input impedance, directivity, etc.) and its structural material (metal, dielectric, magnetic material, metamaterial, etc.) are not involved in the theoretical formulation of the fundamental limits. Therefore, changing any of these parameters cannot help to improve the antenna bandwidth beyond the traditional fundamental limits.

All theories based on the fundamental limits indicate that for any linear and time-invariant lossless antenna design, Q factor cannot be reduced beyond a limit unless the antenna size is increased. In other words, if the available volume is limited, the bandwidth cannot be improved beyond its limit. Since the rate of data-transmission in a communication system is limited by the antenna bandwidth, this problem becomes significant when a highly-miniaturized antenna is required to transmit information data at a high rate.

Basically, the limiting factor of impedance bandwidth in electrically small antennas is the high amount of stored energy around the antenna region which in turn, increases the Q factor. In contrast with all previous efforts, in this research we take advantage of the intense stored energy in the antenna near-zone rather than trying to reduce it. This way an antenna can be miniaturized as much as desired such that an increased Q factor will not limit the data rate. We demonstrate that in a high-Q antenna, one can change the location of antenna poles and consequently the resonant frequency can be modulated according to a control signal (data). If the near-zone stored energy can be preserved during the switching of resonant frequency, the data-rate can be increased as high as the lower carrier frequency such that a single cycle represents a single bit and the information bandwidth will not be limited by the antenna impedance bandwidth.

1.2.2 Switched Capacitor

A switched capacitor circuit in the basic form is composed of a capacitor and two switches controlled by two non-overlapping clock signals. Kuntz's idea of the analog sample-and-hold [33] was used for the first time as the basis for a new type of analog filter by Fried [34]. Later, Caves [35] called it a switched capacitor filter and Orchard [36] helped to generalize the design for low frequency analog filters. Switched capacitors are generally used to simulate other electronic components and are well-known mostly due to their capability to behave like a resistor. A popular application of switched capacitors is realizing small-size and highly-linear on-chip resistors as real resistive elements are usually bulky and their values vary in different production procedures. Additionally, filters that are made of switched capacitors are accurately tunable by controlling the clock frequency and hence, switched capacitor modules are beneficial for programmable integrated circuit (IC) technologies [37-42].

Figure 1.2(a) shows a switched capacitor circuitry which represents a resistance. The switching signals are shown in Figure 1.2(c). Since the voltage across the capacitor C in Figure 1.2(a) changes between V_1 and V_2, the net transferred electric charge can be expressed as

$$\Delta Q = C(V_1 - V_2) \cdot \tag{1.6}$$

Therefore, the electric current through the switched capacitor during a switching period is given by

$$I = \frac{C(V_1 - V_2)}{T} = f_{CLK}C(V_1 - V_2)\cdot \tag{1.7}$$

Equation (1.7) indicates a relation between voltage and current through a constant term which can be considered as a resistance. The equivalent resistor of the switched capacitor can be expressed as follows:

$$R = \frac{1}{f_{CLK}C}\cdot \tag{1.8}$$

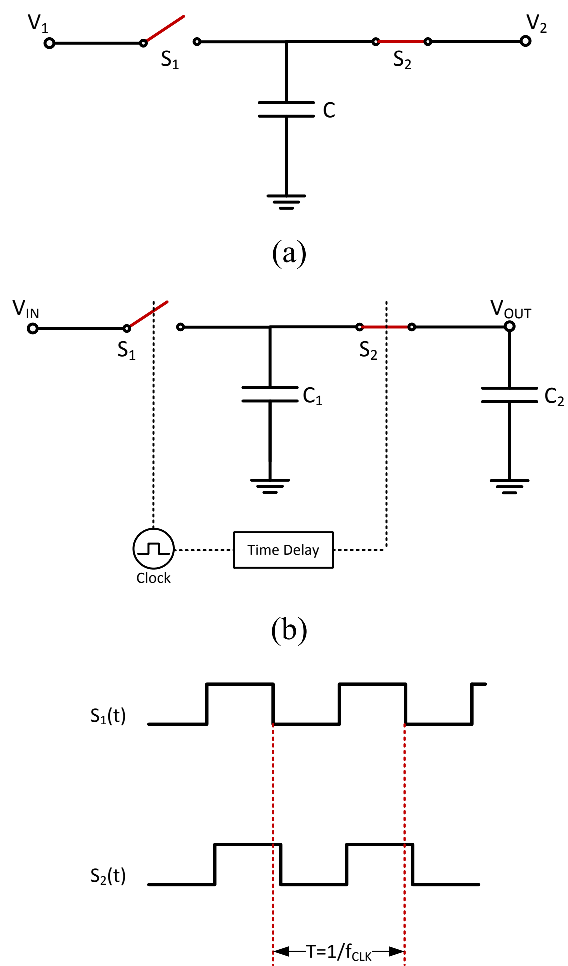

Figure 1.2: Switched capacitor: (a) as an effective resistance, (b) as a low-pass filter, and (c) switching signals.

As (1.8) shows, the resistance is a function of frequency and can be controlled dynamically. This type of resistor has been used extensively in IC filter designs. Figure 1.2(b) shows a simple low-pass filter implemented by a switched capacitor. The cut-off frequency of the filter can be controlled by the clock frequency according to the following relation:

$$\omega_{3dB} = f_{CLK} \cdot \frac{C_1}{C_2} \cdot \tag{1.9}$$

1.2.3 Switched Antenna

The first attempt to use a dynamically switched current as a non-LTI system in an antenna structure to increase the impedance bandwidth was in the early 90's by Joseph Merenda [43-46]. He switched the antenna current between two states, ON and OFF, to synthesize a wideband signal and claimed a significant improvement of the antenna bandwidth. Although he filed four patents on his idea, it took many years to publish his first paper on his antenna [47]. Based on his new approach, the antenna was located between quad-bridge switches, and the desired waveform was synthesized by a sequence of ON and OFF switching states as depicted in Figure 1.3. It has been claimed that the radiation efficiency of the antenna is increased across a wide frequency range. In reality, this design is simply a direct digital synthesizer (DDS), a charge pump/voltage source, and a leaky capacitor/inductor. Therefore, the synthesized signal generated by the DDS radiates through the leaky capacitor/inductor. However, this design requires a switching rate much higher than the frequency of the radiating signal and especially in the microwave regime it turns out to be a challenging design. Also, strong frequency harmonics due to abrupt variations of the voltage across the loop antenna result in spurious radiation and should be taken into account.

A motivating study was reported in 1999 by Fusco [48] which includes a distributed Schottky diode between a patch antenna and ground plane by direct aluminum metallization deposition onto a silicon substrate material. It is shown that by applying different DC bias voltages, the radiation level can be controlled due to the imposed loss (resistive loading). Using this property, Fusco managed to implement a direct amplitude modulation by a narrowband antenna.

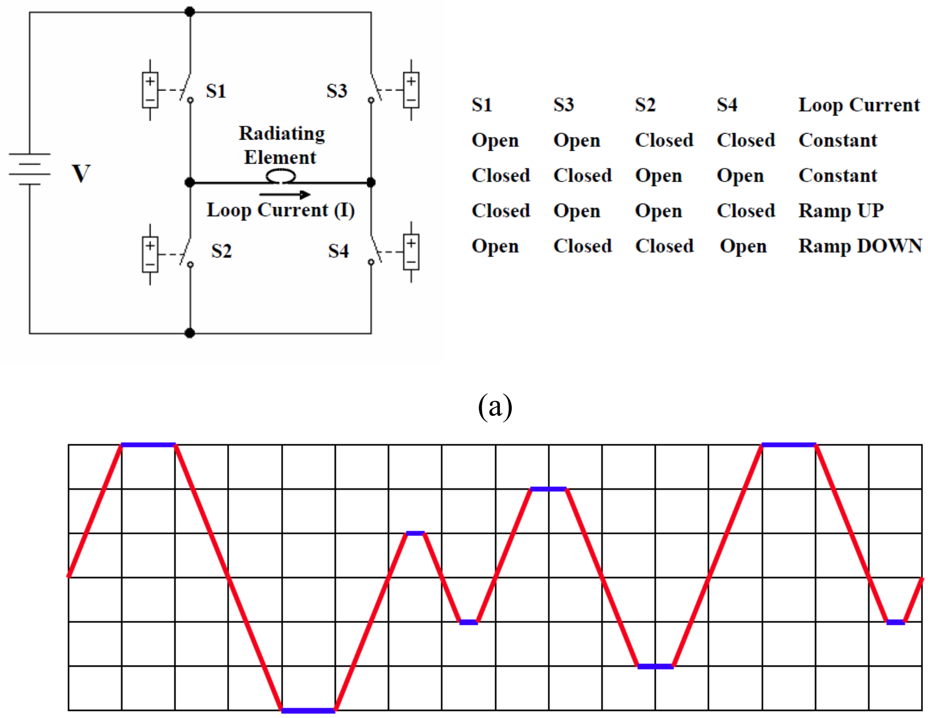

(a)

(b)

Figure 1.3: Switched antenna designed by Merenda [47]: (a) Topology and (b) Synthesized current.

Later, Fusco's work was extended at UCLA [49-54]. They switched the current path of a resonant antenna ON and OFF to generate a fast Amplitude-Shift Keying modulation (ASK). This scenario models the near-field energy as an ideal capacitor which doesn't radiate during the OFF state. This hypothesis is fundamentally incorrect and particularly for high-Q antennas it is not physical to assume that far-field radiation instantaneously vanishes once the current at the input port of the antenna is switched OFF. Their experimental results show that an ASK signal can be transmitted with a data-rate much lower that the carrier frequency. Nevertheless, this type of direct ASK modulation is highly ambiguous since the rising and falling edges of the radiated signal are still ruled by the antenna Q and no true wideband radiation can be created.

A recent publication also perused the concept of direct antenna modulation attempting to increase the information bandwidth by a pulsewidth modulation via a switched antenna [55]. A small antenna is connected directly to a pair of switching transistors and is driven with a pulsewidth modulated HF signal, eliminating the requirement for a frequency-dependent impedance-matching network. The high ringing level and dispersive response of the antenna due to the variations of impedance mismatch factor for different pulsewidths is the major drawback of this work.

There was another attempt to use switches in an antenna structure to increase the bandwidth at Purdue University [56-62]. Their work concentrated on time-varying impedance matching by means of a switched capacitor. This study resulted in realizing a wideband antenna which is able to receive or transmit a short pulse. However, in order to properly switch the capacitor into the circuit to maintain a low VSWR and increase the impedance bandwidth, the received signal should be exactly known in terms of pulse shape, duration and time of arrival. There are some other efforts in the literature that try to increase the bandwidth of the antenna using non-LTI methods [63-67].

In all above efforts, the antenna input current is manipulated in different ways except in [48] which uses a switched resistive load to modulate the radiated power level according to the baseband data signal which is mixed with the carrier signal at the input port of the antenna. It is obvious that as long as the radiation mechanism provided by the antenna structure as a black box remains unchanged, synthesizing the input current using any approach or methodology, ultimately has to deal with the antenna limitations. The proposed work in this dissertation provides a different approach and deals with the electrical properties of the loaded antenna rather than considering a switched current excitation. The baseband information data is used to change the radiation characteristics. Regardless of the antenna impedance bandwidth, a theoretically high rate of data transmission can be achieved. In this method, a small-size and high-Q antenna is represented as a narrowband resonator whose resonant frequency can be controlled by using a switched reactive load; a switched capacitor for example can be used to move the location of antenna poles. This way a “time-varying” radiation can be realized and the antenna characteristics are entirely set in the transient mode. Taking advantage of transient state operation, carrier frequencies can be excited by only an initial current distribution and there is no need to provide RF oscillators. Furthermore, we show that basically any RF part can be dispensed as long as the antenna operates in the transient state and carrier frequencies can be self-generated by the antenna itself as a high-Q resonator. This approach allows making an efficient and wideband data transmission through a highly-miniaturized antenna and deals with the high-Q properties of small antennas as a beneficial point rather than an undesirable limiting factor.

1.3 Overview of the Dissertation

This dissertation is organized into seven chapters. First chapter provides a brief background of previous studies on switched antennas and also essential introductory discussions about the essence of this dissertation and the goals it peruses. Since the present research is principally based on the transient state of small antennas, Chapter 2 is entirely dedicated to a comprehensive investigation on time-domain properties of high-Q antennas. As an example of commonly used low-profile antenna, planar inverted-F antennas (PIFA) are studied in the time domain. It is shown that a natural resonant mode of the antenna can be mimicked by a high-Q RLC resonator not only in terms of frequency-domain characteristics such as input impedance, but also the time-domain parameters of radiated fields such as damping factor and transient damped resonant frequencies are perfectly matched with those of RLC resonators. This analogy between high-Q resonators and small antennas is used to analyze a switched antenna by means of equivalent switched resonator. Chapter 3 discusses the principles of switched resonators and studies the effect of switching a reactive component in a narrowband resonator. Chapter 4 concentrates on switched small antennas as single-mode high-Q resonating structures. However, the impact of switching on the antenna radiation is considered in this chapter. Chapter 5 provides a brief report on the technical showstoppers and suggested solutions toward validation of the proposed technique. In Chapter 6, a very effective and simple method to transmit an RF modulated signal directly through a small antenna by using only baseband information data is proposed. This scheme results in eliminating the RF components required for implementing an FSK modulation such as VCOs. Finally, Chapter 7 summarizes the dissertation and gives the concluding remarks. It also suggests further ideas and shares some thoughts to be used in future research.

Chapter 2

Transient Characteristics of Small Antennas

As the size of an antenna decreases, its Q factor increases. In this chapter, we focus on the transient aspects of high-Q radiators and present a comprehensive investigation on the time-domain behavior of resonant-type antennas. The concept of energy storage and its connection with size and Q factor is described by means of an equivalent circuit of the radial-wave impedance for the fundamental spherical mode. The impact of antenna structure on the field response is studied by analyzing the transient radiation of the Planar Inverted-F Antenna (PIFA) as a typical example of small antennas. Transient mismatch characteristics due to the high amount of stored energy are observed by evaluating the time-domain reflection at the input terminal. Without losing generality, the transient behavior of high-Q antennas can be mimicked by a simple RLC resonator. We show that time-domain characteristics of the fundamental radiated mode are very well matched to that of a high-Q resonator with the same Q and resonant frequency. Early-time response to the Gaussian pulse in the near and far-field is closely observed and its correlation with the exciting pulse is studied. To investigate the effect of switching on the time-domain fields, antennas are fed with a sinusoidal-modulated pulse signal and it is shown that the Q factor and time constant of the fields can be controlled by switching to different source impedances during the OFF-state of the input modulated pulse.

2.1 Introduction

The transient response of antennas becomes significant when antennas are used in a time-varying fashion. Radiation properties of the antennas are usually defined, calculated, and measured in the frequency domain and/or the steady-state time-harmonic regime. Frequency-domain analysis characterizes the antenna irrespective of the physical time-dependent aspects and neglects the transient properties of the antenna. When it is required to switch between different narrowband radiation mechanisms or different sources, e.g. time-varying configurations such as reconfigurable multi-band antennas, switched-beam antennas, direct-modulating antennas, etc. [55, 68-72], it is important to have a comprehensive knowledge of the transient behavior of the antenna. Particularly, if the switching period between different radiating configurations is in the order of the time constant of the system, it is necessary to fully consider the transient response of the antenna. In ultra-wideband systems, switching the antenna may not be a matter of concern because radiation fields track any source variations. In fact, in wideband antennas the amount of non-radiating energy that contributes to the radiation is small and the input power directly couples to the radiating fields. Conversely, small resonant antennas are distinguished by their capability to store a significant amount of reactive energy in the near-field region.

Although there has been a tremendous amount of research on the antenna Q and its correlation with stored energy in the frequency domain [4, 5, 20, 73-82], only a few studies on the time-domain representation of energies are reported [83-89]. The Spherical Wave Expansion (SWE) method is used in [86, 87] to formulate the radiative and reactive pulsed power-flow in the time domain. A general expression for the total electric and magnetic energy generated by an arbitrary source in the time domain is presented in [84, 85]. These reports expound the concept of reactive and radiative energies in time domain. The influence of the antenna structure on modal currents is also perceived by the well-known Theory of Characteristic Modes (TCM) that uses a decomposition methodology to express the total current as a set of current modes that represent the resonances of the antenna according to the boundary conditions [90, 91]. A transfer function for any type of antenna structure may be achieved by using the Singularity Expansion Method (SEM) in time and frequency domains by modeling the antenna based on pole/residue analysis [92-97].

By definition, antenna *Q* factor is the ratio of reactive energy to the radiated or dissipated energy in steady state. Therefore, a high-*Q* antenna tends to store the input energy rather than radiating it. It is a well-understood concept that antenna performance is bounded by the fundamental limit that puts the size, radiation efficiency, and bandwidth of an antenna in contradiction. Although an antenna can be made of very low-loss conductors and dielectrics, radiation resistance decreases as antenna size decreases and hence, realized radiation efficiency is substantially reduced in small-size antennas. Furthermore, in a low-loss antenna structure, bandwidth is limited by the size. The fundamental limit places a lower bound on the *Q* factor of the antenna which is inversely proportional to the impedance bandwidth in narrowband structures. For a high-*Q* antenna, energy can be stored in the form of electric or magnetic energy. Since the near-field of a high-*Q* antenna is highly capacitive (electric antennas, e.g. dipole) or inductive (magnetic antennas, e.g. loop), a significant impedance mismatch occurs when the frequency of the source deviates from that at which the fields resonate; which results in a narrow impedance bandwidth. Hence, it is preferred to achieve a *Q* as low as possible when designing small-size antennas. Far-field response to an input signal is influenced by the *Q* factor of the antenna. In a high-*Q* antenna, an extensive amount of energy must be stored in the near-field before effective far-field radiation begins. Therefore, the transient duration of the far-field response can be defined as the time it takes for the antenna to build up the stored energy. The higher *Q* factor results in a longer time duration for the antenna to reach the maximum radiation efficiency. In a switched-antenna application, this transient effect dominates the performance of the antenna if the switching period is not long enough to let the near-field build up the entire stored energy.

In this chapter, we present a comprehensive study on the transient characteristics of high-*Q* antennas. The radiation mechanism will be explained with the help of a circuit model. As an example of a typical small antenna, the transient response of the Planar Inverted-F Antennas (PIFA) will be discussed based on the *Q* factor and exciting signal. Basic radiation fundamentals are presented in Section 2.2. In Section 2.3, the Gaussian pulse response of PIFAs with different *Q* factors is discussed. A switched antenna with sinusoidal excitation is investigated in Section 2.4.

2.2 Circuit Model of Radiation Mechanism

2.2.1 Spherical Modes

Conventionally, the diameter of a sphere that encloses the antenna is known as antenna size. An ideal antenna is the one that effectively uses the entire enclosing sphere to radiate a TM_{01} mode as the only excited spherical mode. Such an antenna meets the fundamental limit and can be used as a reference to evaluate the figure-of-merit of any small antenna design. Chu introduced an equivalent circuit to represent the radial-wave impedance for spherical modes [5]. Figure 2.1 shows an antenna enclosed by a sphere with radius "a" and the Chu's equivalent circuit for the radial TM_{01} wave impedance. Circuit components are normalized to the far-zone wave impedance, η_0. If ρ is the electrical size of the antenna i.e. $\rho=ka$ where k is wave number in free space, impedance of the shunt inductor L and series capacitor C can be expressed as $j\rho$ and $(j\rho)^{-1}$, respectively. Series capacitor C and shunt inductor L represent the stored energy in the near-field of the antenna. If the electrical size of the antenna is large (ρ>>1), capacitor C approaches short circuit and shunt inductor approaches open circuit. This means a large-size antenna directly interacts with the wave impedance of a travelling wave in free space and the reactive near-field region that stores the energy is small. In other words, an electrically large antenna does not store a considerable amount of energy and has a small Q factor. Conversely, for an electrically small antenna (ρ<<1), the series capacitive reactance is large and the shunt inductive reactance is small. Therefore, combination of the shunt inductor and the wave impedance results in a small resistive part and a large capacitive part in the input impedance of the spherical TM_{01} mode. It means that most of the energy is stored in the near field and a small portion of energy radiates and antenna has a high Q factor. This can be understood easily by looking at the normalized input impedance of the TM_{01} mode as

$$Z_{TM_{01}} = \frac{\rho^2}{1+\rho^2} - j\frac{1}{\rho(1+\rho^2)} \tag{2.1}$$

$$Z_{TM_{01}} \approx \begin{cases} 1 - \dfrac{j}{\rho^3} & ;\ \rho \gg 1 \\ \\ \rho^2 - j\dfrac{1}{\rho(1+\rho^2)} & ;\ \rho \ll 1 \end{cases} . \tag{2.2}$$

Real and imaginary part of the normalized input impedance is shown in Figure 2.2. It shows that for a small-size antenna (*ρ=ka<<1*), the input impedance is extremely capacitive and the real part is small, denoting that the antenna stores a high amount of electric energy. For a magnetic antenna such as a small loop, the fundamental mode is TE_{01} and the circuit model will be dual of TM_{01} mode. Therefore, for a small antenna that excites TE_{01} as the fundamental mode, input impedance is extremely inductive and energy is stored in the form of magnetic energy. The point *ka=1* in Figure 2.2 is known as radian sphere where the real and imaginary parts of the normalized input wave impedance cross at ±0.5 Ω and radiating fields start to decouple from the stored energy. It should be noted that due to the time delay between the near-field and far-field regions, a lossless transmission line should be placed after the wave impedance [3]. Since such a transmission line does not contribute to the *Q* factor, it is not within the scope of this chapter.

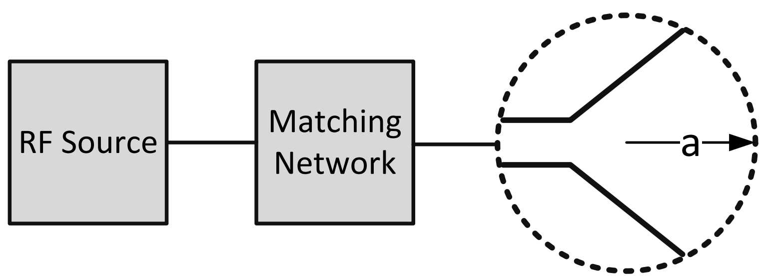

(a)

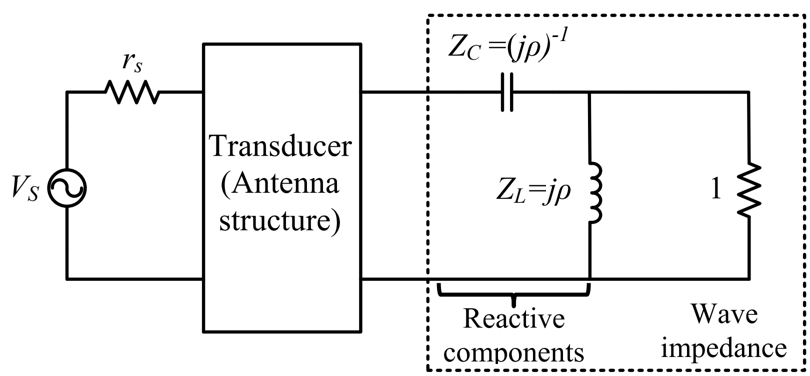

(b)

Figure 2.1: Chu's antenna model: (a) antenna with enclosing sphere of radius *a* and (b) equivalent circuit for normalized wave impedance of fundamental mode (TM_{01}).

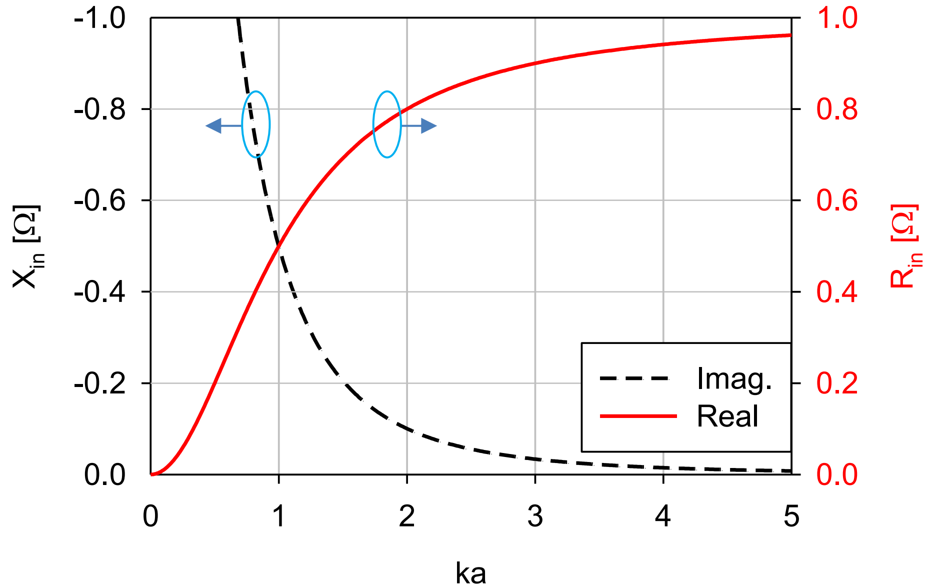

Figure 2.2: Normalized wave impedance for fundamental TM_{01} mode.

Chu's equivalent circuit can be employed to explain the contradiction between size and Q factor (bandwidth) of an arbitrary antenna that excites the TM_{01} spherical mode. The circuit model in Figure 2.1 results in the lower bound of radiation Q for small antennas which is given by [20, 76]

$$Q_{min} = \frac{1}{\rho^3}. \tag{2.3}$$

For higher order modes, more LC pairs are added to Chu's ladder circuit according to the number of excited modes. Hence, stored energy in reactive elements will increase, which in turn increases the Q factor as well.

Chu's circuit model represents the radial spherical modes and provides knowledge about the radiation Q. It characterizes the antenna as a high-pass filter such that each excited mode can be specified with a cut-off frequency.

If we consider the circuit model as a two-port network with a power source with normalized impedance $r_s = \frac{R_s}{\eta_0}$ at the input port and the far-field region represented by the normalized wave impedance as the output port, we can find the voltage transfer function of the fundamental TM_{01} mode. Letting $s = j\rho$, the voltage transfer function can be found as

$$\begin{aligned} H(s) &= \frac{1}{1+r_s} \cdot \frac{s^2}{s^2 + s + \frac{1}{1+r_s}} \\ &= \frac{1}{1+r_s} \cdot \left(1 - \frac{s + \frac{1}{1+r_s}}{s^2 + s + \frac{1}{1+r_s}} \right). \end{aligned} \tag{2.4}$$

Transfer function consists of an entire function representing the transmission of the source signal and a pair of complex conjugate poles representing the far-field transient which is typically an underdamped response. Poles are

$$s_{1,2} = 0.5 \left(1 \pm j \sqrt{\frac{3 - r_s}{1 + r_s}} \right). \tag{2.5}$$

As can be observed from (2.5), the location of the poles is a function of source impedance. This indicates that the source impedance can change the type of the transient response for a given antenna size; for example if $r_s < 3$ as in most practical cases, the transient response will be ringing.

2.2.2 Antenna Structure

Chu's circuit model doesn't deal with the antenna structure. Depending on the antenna geometry, they can be modeled by transmission lines, cavities, etc., with equivalent reactive components that are capable of storing energy. Moreover, some energy can be stored in the matching network. As a result, the location and number of poles in the transfer function will change according to the equivalent components of the antenna structure and matching network. This will affect the overall performance of the antenna. If the antenna is a resonant type, natural resonances of the structure dominate the high-pass behavior of the spherical modes and turn the antenna into a high-Q bandpass configuration. In fact, the antenna structure in Figure 2.1 is a tuning network that adjusts the resonant frequency and consequently modifies the overall Q. In its simplest form, antenna structure can be modeled by a series inductor that tunes the antenna at a desired resonant frequency. Impedance of this tuning inductor can be expressed as

$$Z_{tune} = \frac{j\rho}{\rho_0^2(1+\rho_0^2)}, \tag{2.6}$$

where $\rho_0 = k_0 a$ is the electrical size of the antenna at the tuned resonant frequency. However, a series inductor may not be sufficient to model the entire antenna structure. Depending on the antenna type, the equivalent circuits that represent the antenna structure may differ.

Overall performance of the antenna is a result of coupling between the modal currents on the antenna surface (natural resonances of the antenna structure) and the modal spherical waves. A significant amount of work has been done to obtain a transfer function that mimics the antenna as a black box associating the radiation fields with the input RF signal. One common approach to obtain the transfer function of antennas is using the Singularity Expansion Method (SEM) that utilizes the time or frequency-domain response to model the antenna [92-95]. Since SEM requires the transient response of the antenna in order to model the antenna characteristics, numerical methods in the time domain should be employed to characterize the transient behavior of any arbitrarily shaped antenna [98, 99]. In the next section we use CST Microwave Studio, which includes a commercial time-domain code, to study the transient characteristics of planar inverted-F antennas (PIFA) as an example of widely-used low profile antennas in cellular communications.

2.3 Gaussian Pulse Excitation

2.3.1 Reflection at the Input Terminal

Figure 2.3 shows a traditional PIFA with a ground plane size of half-wavelength at resonant frequency. In order to study the transient response of the fundamental mode (TM_{01}), a Gaussian pulse with a full-width at half-maximum (FWHM) of $\tau_{FWHM} = 800$ ps is chosen to ensure that high order modes are not excited. Four different antennas are designed at the same resonant frequency 530 MHz with different Q factors. Table 2.1 summarizes the physical dimensions and Q factors of the different designs. PIFAs are made of copper with thickness of 0.5 mm and the width of shorting pin for all designs is 3 mm. Q factors are calculated as the ratio of resonant frequency to the 3-dB impedance bandwidth according to the reflected power. Figure 2.4 shows the return loss for different designs.

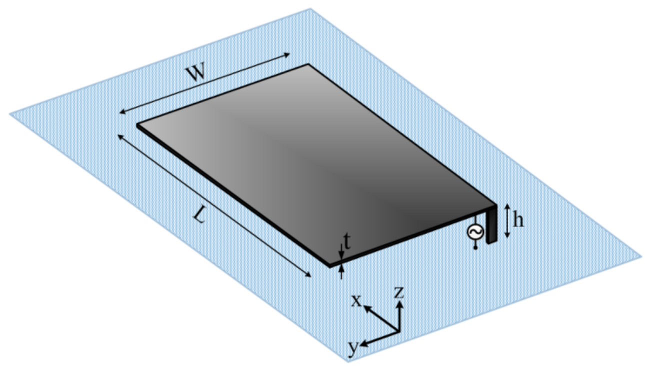

Figure 2.3: Planar inverted-F antenna (PIFA) structure.

Table 2.1: Physical dimensions and *Q* factors of PIFA designs

	Dimensions ($L \times W \times h$) (cm)	Q factor
PIFA 1	9×5×0.3	128
PIFA 2	9×5×0.5	78
PIFA 3	9×4.6×1	36
PIFA 4	5.5×3×5	6.4

Since a high-Q antenna has a highly capacitive or inductive near field, a large mismatch occurs during the excitation period which is conventionally known as "early time". Early-time reflected signals at the input port are shown in Figure 2.5. Depending on the geometry of the antenna and the feeding type, early-time mismatch can be similar to an open or short circuit. For a PIFA, due to the shorting pin which is located near the feeding point, early-time behavior can be seen as a short circuit. However, if the height of the shorting pin increases, input inductance is dominant and the early-time reflection can be approximated as the reflection from an RL circuit as depicted in Figure 2.5. PIFA 4 has a significantly longer shorting pin and the reflected signal approaches that of an inductive impedance. For a differentially-fed antenna such as dipole, early-time reflection would be similar to an open circuit.

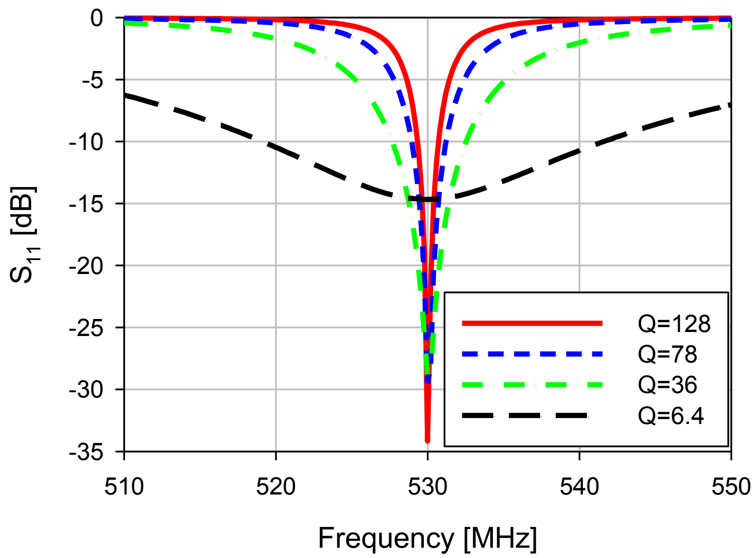

Figure 2.4: Return loss for different PIFA designs.

In fact, due to the high Q of the antenna, only a small portion of the available power leaks into the near field and forms the reactive energy. Since the PIFA is a resonant type antenna, reactive energy is distributed between the excited natural resonances. If the input pulse is wide enough to excite only the fundamental mode, stored energy dissipates at the 1st resonant frequency after the source signal completely dies. Depending on the source impedance, part of the energy reflects back to the source and the rest of the energy radiates. Similar to a narrowband resonator, the rate of the energy dissipation is a function of Q factor. This can be seen in Figure 2.6 that shows the late-time reflection at the input terminal. From Figure 2.6 the fall-time (90 to 10 percent) of the reflected signals can be calculated to be about 170 ns, 100 ns, 48 ns and 8 ns for antenna of 1 to 4, respectively. This time duration can be interpreted as the required time for the antenna to maintain the complete impedance matching once the source is turned on. We will show in Section 2.3.3 that the time constant of the near and far fields is indeed the same as that of the reflected signal at the input port of the antenna.

It should be noted that for differentially-fed antennas such as the dipole, the proper equivalent RLC circuit for the resonant mode would be a series arrangement, because there is no such capacitor parallel to the source which leads to a short circuit in early-time. As a result, the reflected signal at the input port will be in-phase compared to the input pulse, denoting an open circuit behavior in early-time.

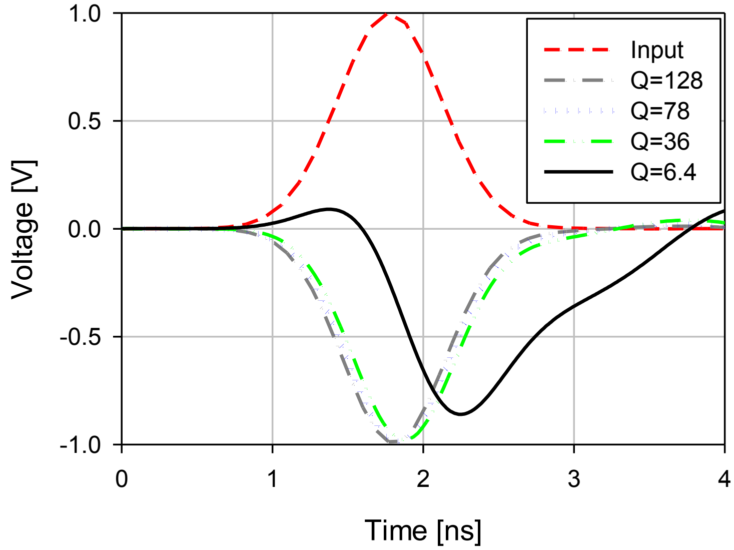

Figure 2.5: Early-time reflected voltages at the input port of different PIFA designs.

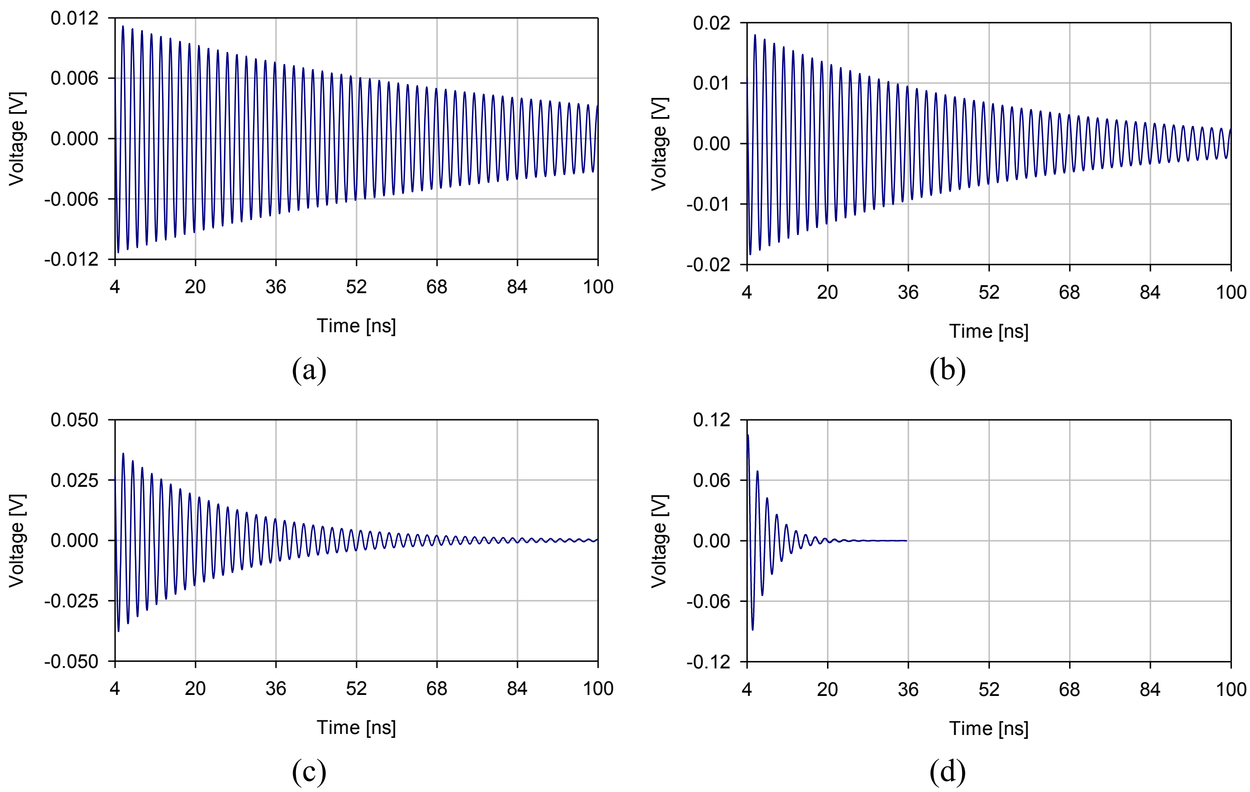

Figure 2.6: Late-time reflected voltages at the input port for (a) PIFA 1, Q=128, (b) PIFA 2, Q=78, (c) PIFA 3, Q=36, and (d) PIFA 4, Q=6.4.

Figure 2.7 shows the input pulse and reflected voltage waveform for a half-wavelength dipole which resonates at 530 MHz. Although dipole bandwidth is usually much wider than a PIFA at the same resonant frequency and therefore, the oscillating tail of the reflected signal decays much faster, the early-time reflection exhibits a very high impedance during the excitation.

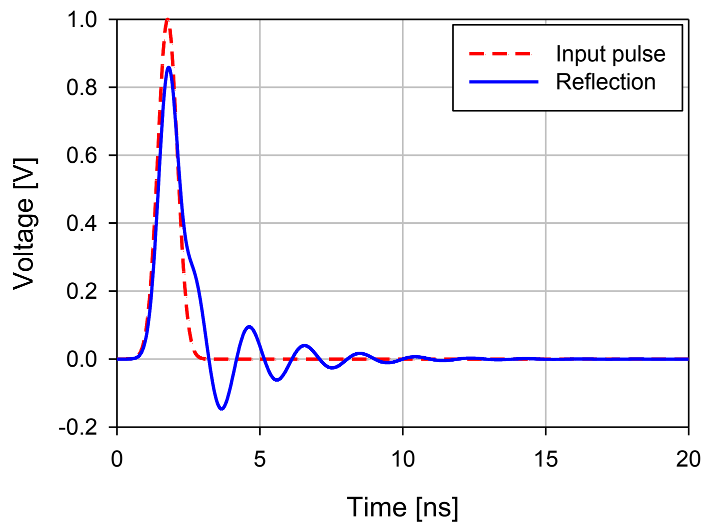

Figure 2.7: Input pulse and reflected voltage waveform for a half-wavelength dipole resonating at 530 MHz.

2.3.2 Far-field and Near-field Response

As was discussed in Section 2.2, spherical modes have high-pass characteristics and all antenna resonances above the cut-off frequency of the fundamental mode exist in the electric field response. However, each excited resonance appears with a different damping factor. Since at higher resonances, electrical size of the antenna is larger, higher order Q factors are greater than Q of the fundamental resonance, results in higher damping factors. As a result, all higher order resonances decay faster compared to the dominant resonance. In order to study the higher order resonances we would feed the antenna with a narrow pulse such that more number of modes are excited. Figure 2.8 shows the simulation set-up for field computation. Four probes are located in the azimuth plane of PIFA 2 ($Q_{fundamental}$=78). The distance of the probes p_1, p_2, p_3 with the ending aperture of the antenna is 1, 10 and 30 mm, respectively. Probe p_4 is used to compute the far field at a distance of 2 m. Figure 2.9 shows the z components of the electric fields at each probe location for an input pulse with a $\tau_{FWHM} = 100$ ps. Regardless of the probe position at which fields are computed, higher order resonances exist at the beginning of all time-domain responses. Each resonance has a unique damping factor which is much larger than that of the fundamental mode. Damping factor for each frequency component can be calculated by singularity expansion method and it is shown that the existence of each resonant frequency and their damping factor is not affected by the distance and angle of measurement position with respect to the antenna origin [92]. Thus, the transient fields are similar in any arbitrary measurement point in terms of time constant associated with each resonant frequency.

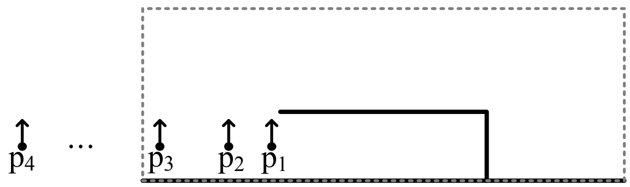

Figure 2.8: Simulation set-up for field computation. z-directed probes p_1 to p_4 are located 1, 10, 30 mm and 2 m away from the radiating aperture of the PIFA.

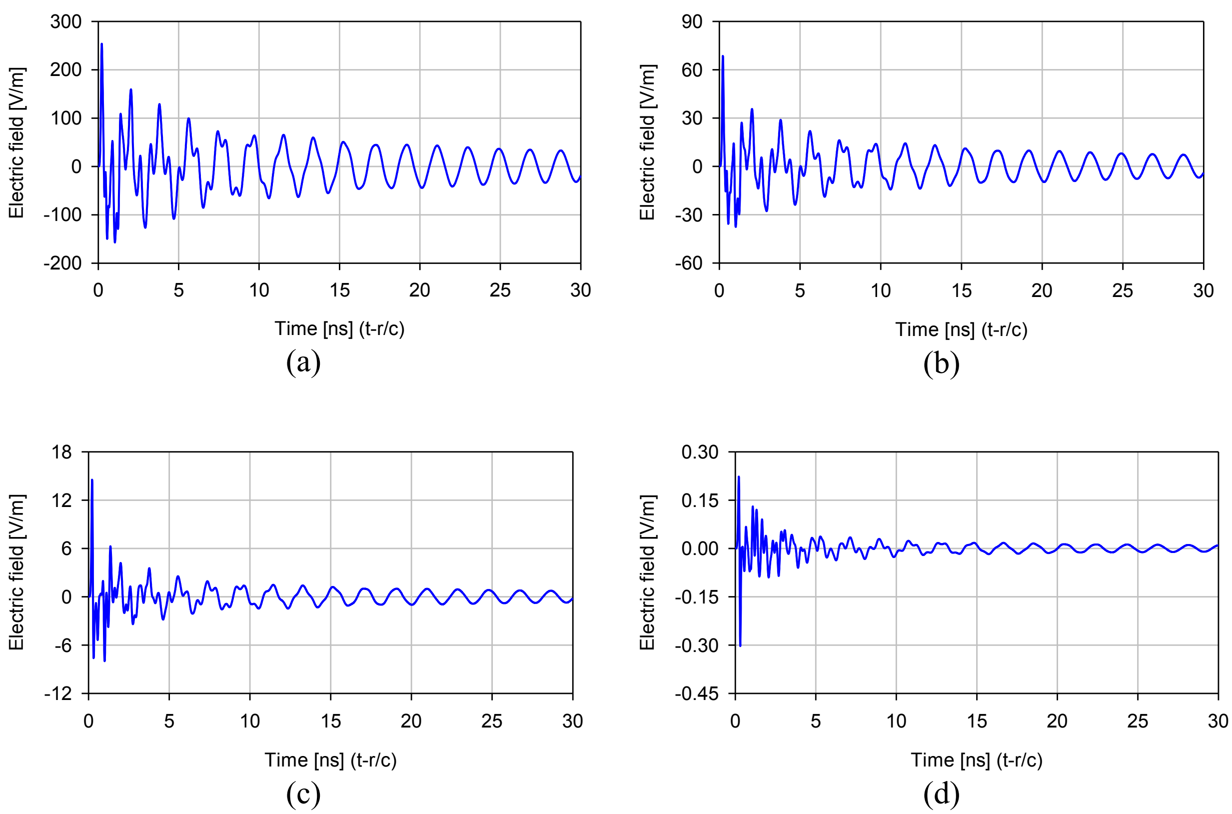

Figure 2.9: Electric fields of the PIFA 2 due to an input Gaussian pulse with $\tau_{FWHM} = 100$ ps, computed at different probe positions: (a) 1 mm, (b) 10 mm, (c) 30 mm and (d) 2 m. (time delays are excluded).

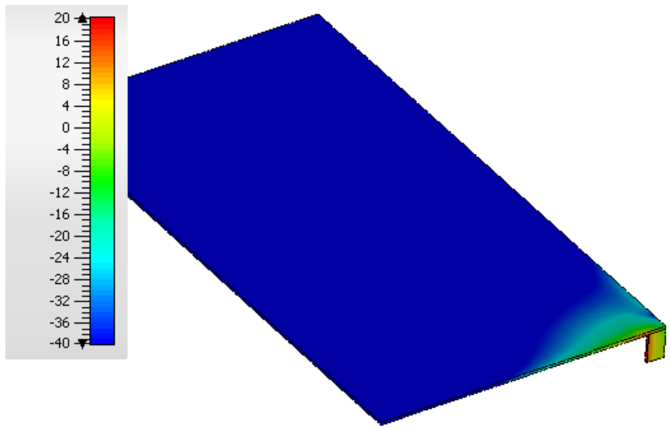

(a)

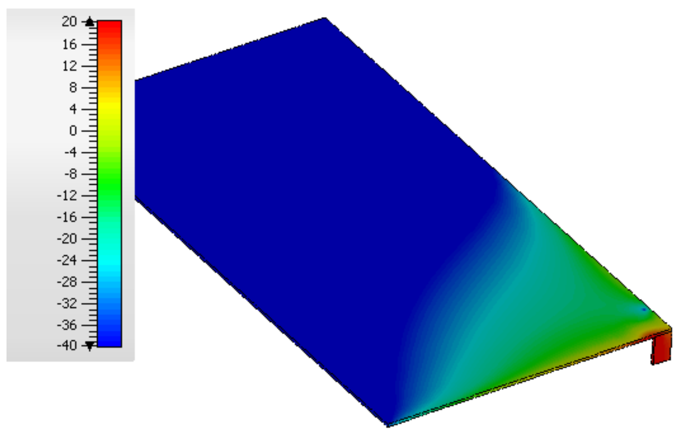

(b)

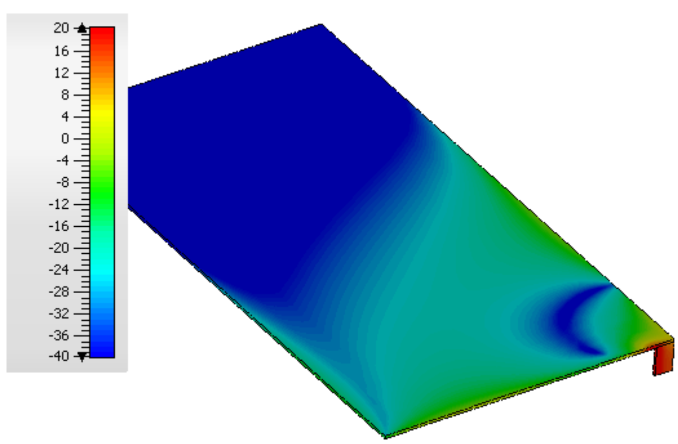

(c)

Figure 2.10: Current distribution on PIFA 2 at different time samples: (a) 180 *ps*, (b) 270 *ps* and (c) 360 *ps*. Color-code bar is in dB scale (dBA/m). Iinput pulse is Gaussian with $\tau_{FWHM} =$ 100 ps.

It is worthwhile to point out that the early-time response of the electric field is a signature of source signal. If the surface current distribution is **J**, electric far-field can be related to the time derivative of current distribution as [88]

$$\mathbf{e}(\mathbf{r},\mathrm{t}) = \frac{\partial}{\partial \mathrm{t}}\left[\frac{\mu}{4\pi r}\int_{S'} \mathbf{J}\left(\mathbf{r}', t - \frac{r - \hat{\mathbf{r}}\cdot\mathbf{r}'}{c}\right) ds'\right]\cdot \tag{2.7}$$

If the input pulse is sufficiently narrow such that the early-time radiation is caused by the travelling current on the antenna surface, boundary conditions at the open end side of the antenna do not contribute to the creation of modal currents and high-pass characteristics of the spherical modes allow transmitting a wideband signal. Hence, a time derivative of the input pulse appears in the far field in early time according to (2.7). Figure 2.10 illustrates the current distribution on the PIFA 2 for three time samples. Since the input pulse ends before the surface current hits the open end of the antenna structure and the natural resonances are formed, early-time response can be approximated by a small dipole that excites the TM_{01} mode. The shape of early-time electric field varies with the distance from the antenna. This can be demonstrated by looking at the time-domain electric field of a Hertzian dipole which is equivalent to the fundamental mode (TM_{01}) fields. If the moment of Hertzian dipole is represented by **P**, electric and magnetic fields is given by [100, 101]:

$$\mathbf{E}\,(\mathbf{r},\omega) = \frac{1}{4\pi\epsilon_0}\left\{k^2(\hat{\mathbf{r}}\times\mathbf{P})\times\mathbf{r}\frac{e^{-jkr}}{r} + [3\hat{\mathbf{r}}(\hat{\mathbf{r}}.\mathbf{P}) - \mathbf{P}]\left(\frac{1}{r^3}+\frac{jk}{r^2}\right)e^{-jkr}\right\} \tag{2.8}$$

$$\mathbf{H}\,(\mathbf{r},\omega) = \frac{ck^2}{4\pi}(\hat{\mathbf{r}}\times\mathbf{P})\frac{e^{-jkr}}{r}\left(1+\frac{1}{jkr}\right)\cdot \tag{2.9}$$

Taking inverse Fourier transform from above expression yields

$$\mathbf{e}(\mathbf{r},t) = \frac{1}{4\pi\epsilon_0}\left\{\frac{(\ddot{\mathbf{p}}(\tau)\times\hat{\mathbf{r}})\times\hat{\mathbf{r}}}{c^2 r} + \frac{3\hat{\mathbf{r}}[\hat{\mathbf{r}}.\dot{\mathbf{p}}(\tau)] - \dot{\mathbf{p}}(\tau)}{cr^2} + \frac{3\hat{\mathbf{r}}[\hat{\mathbf{r}}.\mathbf{p}(\tau)] - \mathbf{p}(\tau)}{r^3}\right\} \tag{2.10}$$

$$\mathbf{h}(\mathbf{r},t) = \frac{1}{4\pi}\left[\frac{\ddot{\mathbf{p}}(\tau)\times\hat{\mathbf{r}}}{cr} + \frac{\dot{\mathbf{p}}(\tau)\times\hat{\mathbf{r}}}{r^2}\right], \tag{2.11}$$

where $\tau = t - \frac{r}{c}$ is retarded time. For a z-directed Hertzian dipole, we have

$$\mathbf{p}(t) = p(t)\hat{\mathbf{z}} \tag{2.12}$$

and the time-domain fields can be expressed as

$$\mathbf{e}(\mathbf{r}, t) = \frac{1}{4\pi\epsilon_0}\left\{\left[\frac{\dot{p}(\tau)}{cr^2} + \frac{p(\tau)}{r^3}\right]2cos\theta\hat{\mathbf{r}} + \left[\frac{\ddot{p}(\tau)}{c^2 r} + \frac{\dot{p}(\tau)}{cr^2} + \frac{p(\tau)}{r^3}\right]sin\theta\hat{\boldsymbol{\theta}}\right\} \tag{2.13}$$

$$\mathbf{h}(\mathbf{r}, t) = \frac{1}{4\pi}\left[\frac{\ddot{p}(\tau)}{cr} + \frac{\dot{p}(\tau)}{r^2}\right] sin\theta\hat{\boldsymbol{\varphi}}. \tag{2.14}$$

In the azimuth plane, θ (or z) component of the electric field for a z-directed Hertzian dipole can be expressed as

$$\mathrm{e}_\theta\ (r, t) = \frac{1}{4\pi\epsilon_0 r}\left(\frac{\ddot{p}(\tau)}{c^2} + \frac{\dot{p}(\tau)}{cr} + \frac{p(\tau)}{r^2}\right), \tag{2.15}$$

where p represents the time-domain electric charge distribution of the dipole. The expression within the parentheses in Equation (2.15) divides the azimuth plane into three sections: quasi-static zone ($1/r^2$ term), induction zone (1/r term) and far-field zone (constant term) as shown in Figure 2.11. It can be seen from (2.15) that in the proximity of the antenna or quasi-static zone, electric field is similar to the surface electric charge. However at intermediate distances or induction zone, electric field is proportional to the derivative of the dipole moment which is equal to the electric current on the dipole. As the probe moves away from the antenna to the far zone, constant term will be dominant and the electric field will be proportional to the second derivative of the dipole moment or first derivative of the current.

Figure 2.12 depicts the early-time electric fields of PIFA 2 at four probe locations. It demonstrates the electric field development when probe moves from near to far distance from the antenna. It can be concluded from (2.7) and (2.15) that fields tend to approach the time derivative of the source current as they are measured from a larger distance from the antenna. For a narrower input pulse, this trend will be closer to the theoretical expectation.

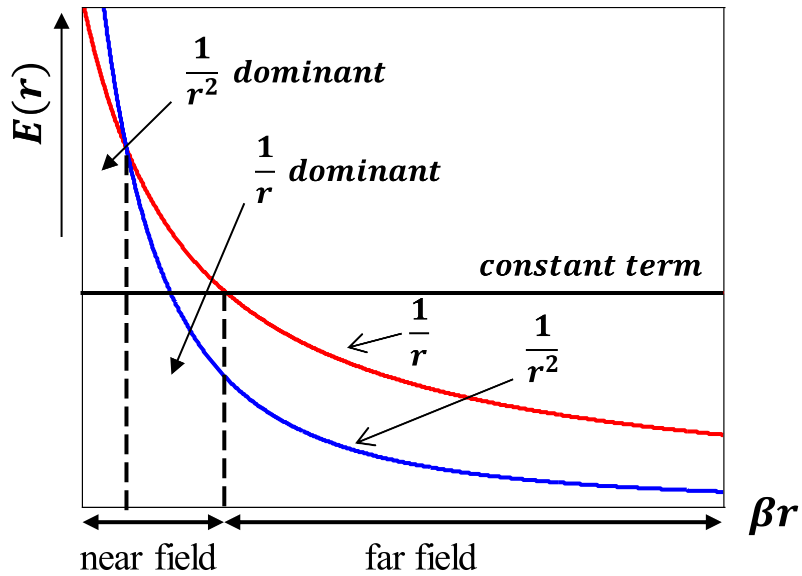

Figure 2.11: Illustration of different field zones around the Hertzian dipole.

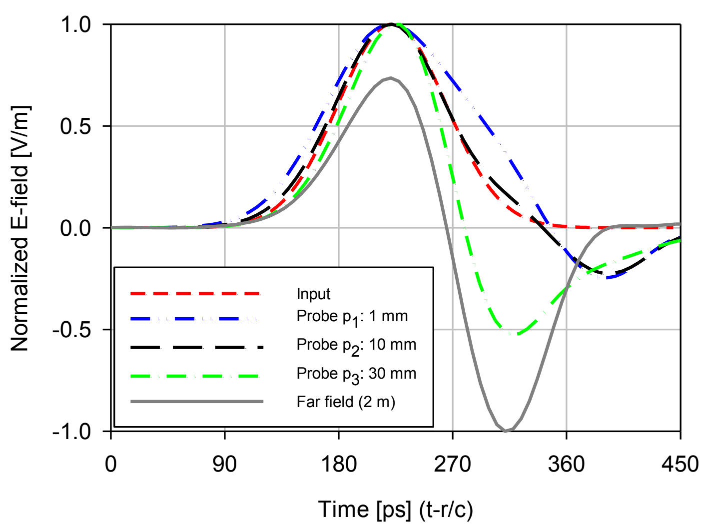

Figure 2.12: Early-time electric fields of the PIFA 2 in the azimuth plane normalized to their peak values.

It would be also interesting to point out that not only the early-time response of the fields is evolving over different zones; the radial energy flow velocity also varies from near field to far field [3, 102].

This velocity can be computed from Kaiser's definition [102] as the ratio of Poynting vector to the total electric and magnetic energy

$$\mathbf{v}\,(\mathbf{r},t)=\frac{\mathbf{S}\,(\boldsymbol{r},t)}{\mathbf{W}\,(\mathbf{r},t)}=\frac{\mathbf{e}(\mathbf{r},t)\times\mathbf{h}(\mathbf{r},t)}{\frac{1}{2}\epsilon_0|\mathbf{e}(\mathbf{r},t)|^2+\frac{1}{2}\mu_0|\mathbf{h}(\mathbf{r},t)|^2}=2\frac{e_\theta h_\varphi\hat{\mathbf{r}}-e_r h_\varphi\widehat{\boldsymbol{\theta}}}{\epsilon_0\left(e_r^2+e_\theta^2\right)+\mu_0 h_\varphi^2}\cdot \tag{2.16}$$

The radial component of the velocity is

$$v_r=\frac{2e_\theta h_\varphi}{\epsilon_0\left(e_r^2+e_\theta^2\right)+\mu_0 h_\varphi^2}\cdot \tag{2.17}$$

Therefore, the normalized velocity of the radial energy flow can be expressed as

$$\frac{v_r}{c}=2\frac{\left[\frac{\ddot{p}(\tau)}{c^2r}+\frac{\dot{p}(\tau)}{cr^2}+\frac{p(\tau)}{r^3}\right]\left[\frac{\ddot{p}(\tau)}{c^2r}+\frac{\dot{p}(\tau)}{cr^2}\right]}{\left[\frac{\ddot{p}(\tau)}{c^2r}+\frac{\dot{p}(\tau)}{cr^2}+\frac{p(\tau)}{r^3}\right]^2+\left[\frac{\ddot{p}(\tau)}{c^2r}+\frac{\dot{p}(\tau)}{cr^2}\right]^2}\cdot \tag{2.18}$$

Figure 2.13 shows the radial energy flow velocity versus time for different positions in the azimuth plane when the dipole moment is a sinusoid with magnitude 1 and frequency 1 GHz. It can be seen than for the observation points close to the dipole (near-field) a pulse of energy is radiated at every half-period. The emitted energy is partly absorbed by the dipole, creating a negative-sign energy velocity. The part of the energy which is not reabsorbed forms the radiation. As the observation point moves away, the amount of backward energy reduces and in the far field, we can see a total radiation without any energy reflection. It is interesting to notice that both backward and forward energy velocity is smaller than the speed of light in the near field and approaches the speed of light in the far field [103]. Equation (2.18) denotes that at the dipole origin (r=0) the energy flow velocity is zero and at a very large distance from the dipole i.e. r=∞ the energy flow velocity approaches the speed of light.

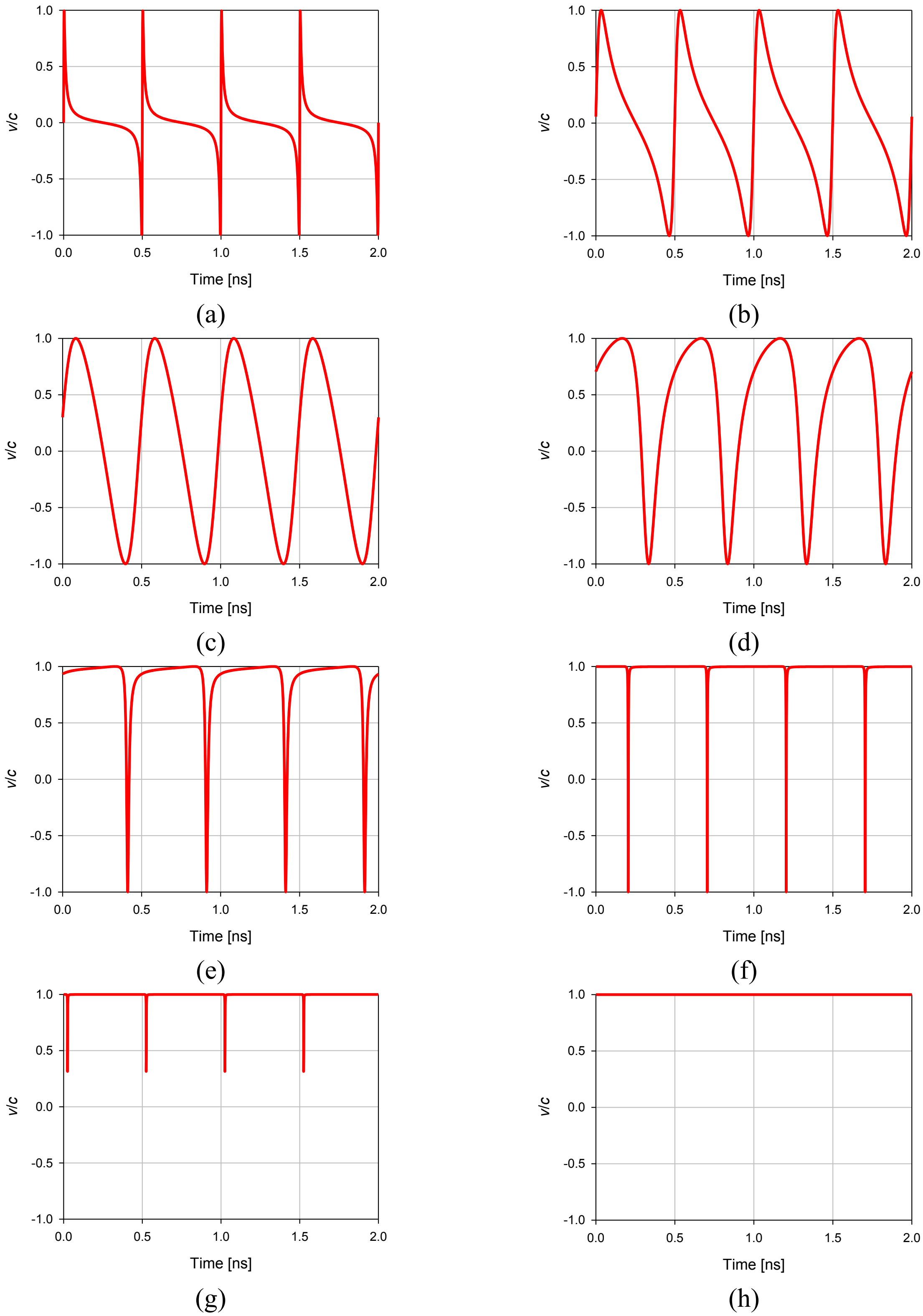

Figure 2.13: Instantaneous radial energy flow velocity in the azimuth plane of a Hertzian dipole with sinusoidal momentum with magnitude 1 and frequency 1 GHz at different positions: (a) $r = \frac{\lambda}{300}$, (b) $r = \frac{\lambda}{30}$, (c) $r = \frac{\lambda}{12}$, (d) $r = \frac{\lambda}{6}$, (e) $r = \frac{\lambda}{3}$, (f) $r = \frac{2\lambda}{3}$, (g) $r = \lambda$, (h) $r = 4\lambda$.

2.3.3 Time Constant of the Fields

To evaluate the time constant of the electric fields of the fundamental mode, we would either filter the electric fields shown in Figure 2.9 to extract the 1st mode or alternatively, we can excite the antennas with a wider input pulse. Generally, high-Q resonant antennas can be modeled by RLC resonators as will be discussed in details in Chapter 4. Therefore, it is convenient to look at the transient response of a high-Q resonator. For a PIFA, we would consider a parallel RLC model because of the short circuit behavior at zero-frequency. The equivalent inductor and capacitor for a parallel RLC resonator with resonant frequency, ω_0, can be expressed as

$$L = \frac{R}{\omega_0 Q} \;\; ; \; C = \frac{Q}{R\omega_0}, \tag{2.19}$$

where $R=R_S||R_L$, R_S and R_L are source and load impedance respectively. For instance, equivalent L and C values for PIFA 1 at f_0=530 MHz can be found equal to 58.651 pH and 1.537 nF. Figure 2.14 compares the return loss and input impedance of PIFA 1 with those of the resonator model. It can be seen that in frequency domain, port characteristics of the antenna is similar to the circuit model. To compare the time-domain behavior of the antenna with that of the circuit model, we would examine the damping factors or time constants of each one. According to the resonator model, the transient response can be written as

$$v_R(t) = \mathrm{V}_0 \cdot \mathrm{e}^{-\alpha t} \sin(\omega_d t), \tag{2.20}$$

where $v_R(t)$ is the voltage at the load and V_0 is determined by initial conditions. The α and ω_d are damping factor and damped resonant frequency, respectively and can be calculated as

$$\alpha = \frac{\omega_0}{2Q} \;\; ; \;\; \omega_d = \omega_0 \sqrt{1 - \frac{1}{4Q^2}}, \tag{2.21}$$

where Q is loaded quality factor and is equal to $(R_S \parallel R_L)\sqrt{C/L}$.

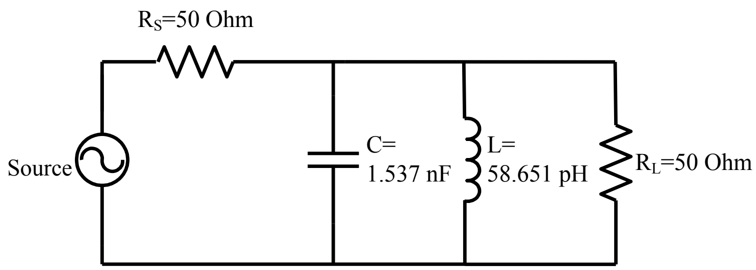

(a)

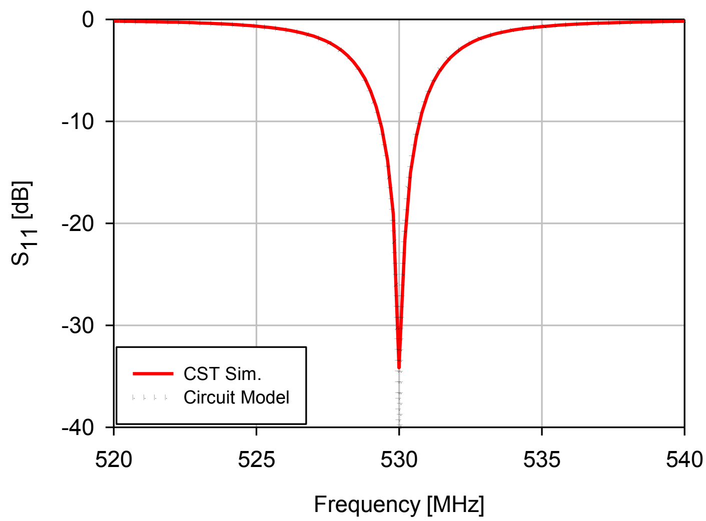

(b)

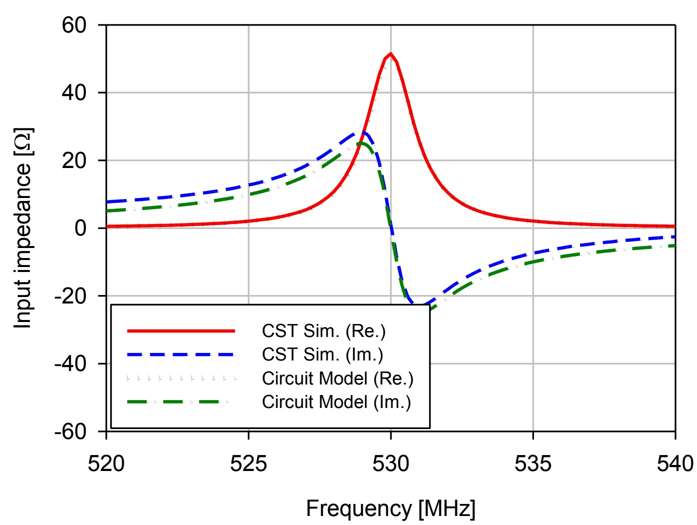

(c)

Figure 2.14: Resonator model for PIFA 1: (a) circuit topology and component values, (b) return loss and (c) input impedance.

For a high-Q resonator (Q>>1), damped resonant frequency can be approximated by steady-state resonant frequency $\omega_0 = 1/\sqrt{LC}$ and the transient voltage at the load can be expressed as

$$v_R(t) = \mathrm{V}_0 \cdot \mathrm{e}^{-\frac{\omega_0}{2Q}t} \sin(\omega_0 t). \tag{2.22}$$

Figure 2.15 and 2.16 show the near-field and far-field of the PIFAs measured by probes p_1 and p_4 due to an input pulse with $\tau_{FWHM} = 800$ ps. For each field representation, envelope is compared to an exponentially decaying function as

$$e(t) = r_{m1,4} e^{\frac{t-t_{d1,4}}{\tau_m}}, \tag{2.23}$$

where τ is equivalent time constant of a parallel RLC resonator and is calculated for each antenna as $\tau_m = \frac{2Q_m}{\omega_0}$. m is the number associated with each antenna according to Table 2.1. The t_d is time delay and r_m is the peak value of each field response. The *"1"* and *"4"* stand for probes p_1 and p_4. In order to exclude the early-time response of the fields from the damped sinusoidal ringing of the transient response, time delay t_d is calculated by adding the duration of the input pulse to the traveling time of the waves from the antenna to the probe location. As depicted in Figure 2.15 and 16, the envelopes of the transient fields agree very well with the described exponential function. This shows a high-Q antenna has the same time-domain properties of a narrowband resonator that operates at the same resonant frequency with an equivalent Q factor. Furthermore, the time constant of the fields agrees with the time constant of the reflected signal at the input terminal as shown in Figure 2.6. However, magnitude of the transient response is a function of probe position, antenna structure, polarization and input power. This magnitude can be computed as the residue of the pole at which antenna response is ringing using SEM [92-95]. Each excited resonance has a particular Q factor and a unique equivalent RLC resonator can be introduced to model each resonant mode separately. It is worthwhile to point out that the spherical radiation modes described in Chu's circuit model should be distinguished from the resonant modes that are modeled by RLC resonators. Since time-domain reflection from the input terminal is an integrated response to the entire excited modes, damping factor (or time constant) for each resonant frequency can be extracted from the reflected signal. Importantly, damping factor is not a space-dependent quantity and hence, does not change in different distances or angles. This can be clearer by looking at the current distribution as the superposition of current modes as follows:

$$\mathbf{J}(\mathbf{r}', t) = \sum_n \mathbf{J}_n(\mathbf{r}') e^{(j\omega_n - \alpha_n)t}, \tag{2.24}$$

where $\mathbf{J}_n(\mathbf{r}')$ is the spatial distribution of current modes and $e^{(j\omega_n - \alpha_n)t}$ is the time-dependent term. Time-domain magnetic vector potential can be expressed as

$$\mathbf{A}(\mathbf{r}, t) = \frac{\mu}{4\pi} \int_{S'} \frac{\mathbf{J}(\mathbf{r}', t - \tau)}{\tau c} ds' \quad ; \tau = \frac{|\mathbf{r} - \mathbf{r}'|}{c} \cdot \tag{2.25}$$

Combining (2.24) and (2.25), $\mathbf{A}$ can be expressed as

$$\mathbf{A}(\mathbf{r}, t) = \frac{\mu}{4\pi} \sum_n e^{(j\omega_n - \alpha_n)t} \int_{S'} \frac{\mathbf{J}_n(\mathbf{r}') e^{-(j\omega_n - \alpha_n)\tau}}{\tau c} ds', \tag{2.26}$$

and the electric field is given by

$$\mathbf{e}(\mathbf{r}, t) = -\frac{\partial}{\partial t} \mathbf{A}(\mathbf{r}, t) + c^2 \int_0^t \nabla\nabla . \mathbf{A}(\mathbf{r}, t') dt' \cdot \tag{2.27}$$

The equation (2.27) consists of spatial and time differential operators. Obviously, any differential or integral operation on $\mathbf{A}(\mathbf{r}, t)$ will keep the time-dependent term, $e^{(j\omega_n - \alpha_n)t}$, unchanged and hence, the electric fields of each resonance at any arbitrary position have the same damping factors, α_n. Therefore, the time-domain reflected signal at the input terminal due to an impulse input contains the complete information about damping factors for all resonant frequencies.

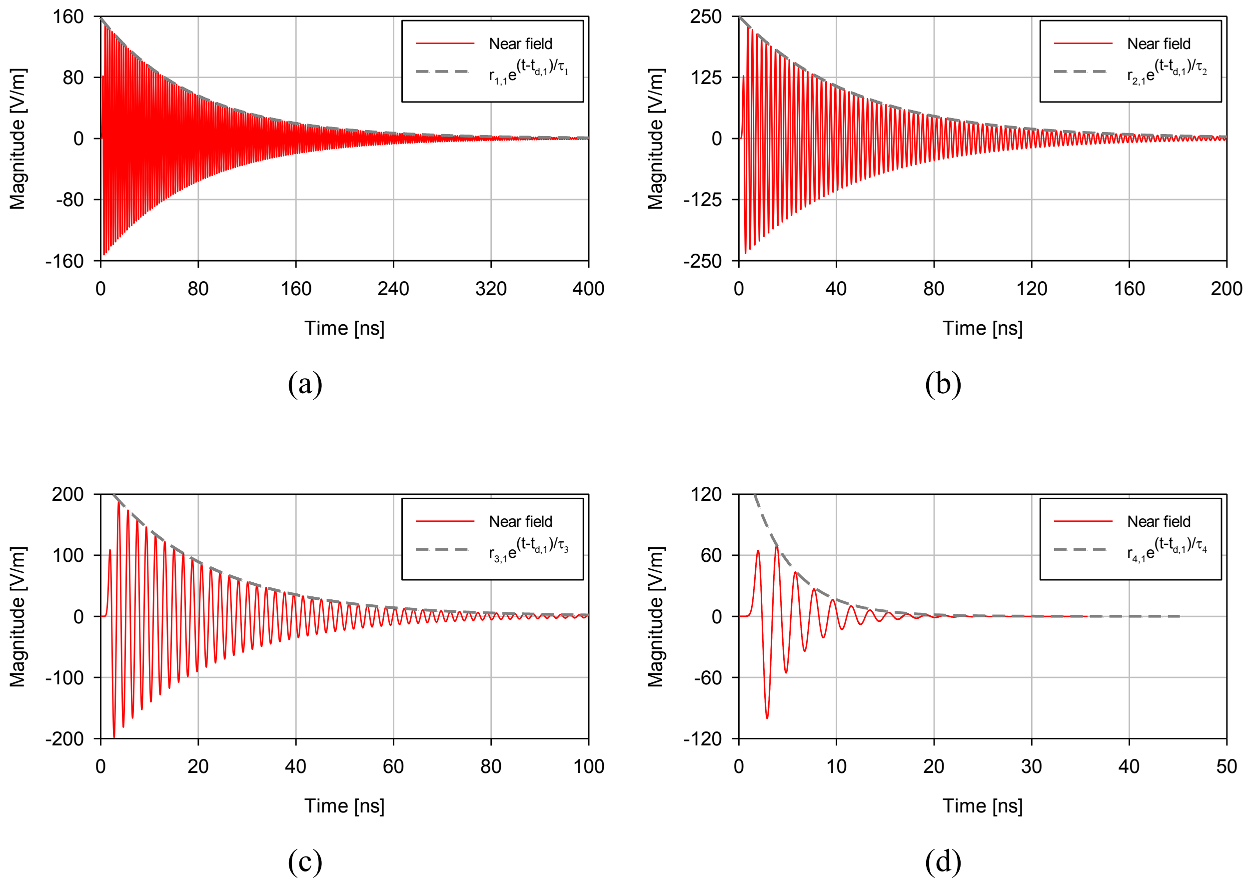

Figure 2.15: Near electric fields calculated at probe p_1 due to an input Gaussian pulse with $\tau_{FWHM} = 800$ ps: (a) PIFA 1, (b) PIFA 2, (c) PIFA 3 and (d) PIFA 4.

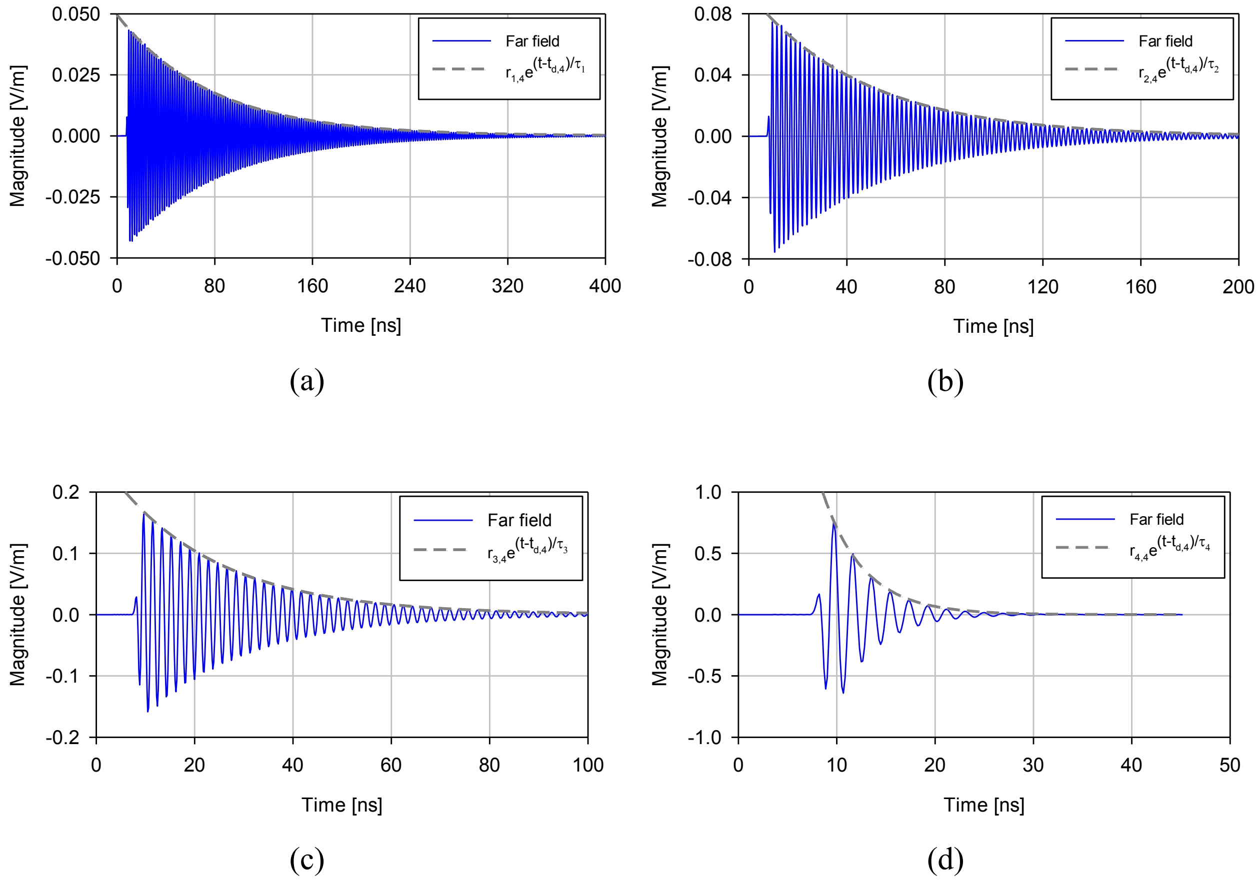

Figure 2.16: Far electric fields calculated at probe p_4 due to an input Gaussian pulse with τ_{FWHM} = 800 ps: (a) PIFA 1, (b) PIFA 2, (c) PIFA 3 and (d) PIFA 4.

Since the time constant of the reflected wave is the same as time constant of the fields, the "matching time" or the required time for a steady-state-matched sinusoidal source to be fully impedance-matched with the input terminal of the antenna can be evaluated by time constant of the fields. Figure 2.17 shows the incident and reflection voltage waveforms for different PIFA designs when excited at 530 MHz. for all cases, the time that takes for the reflected wave to be minimized is exactly equal to the fall or rise time of the electric fields either in the near field or far field.

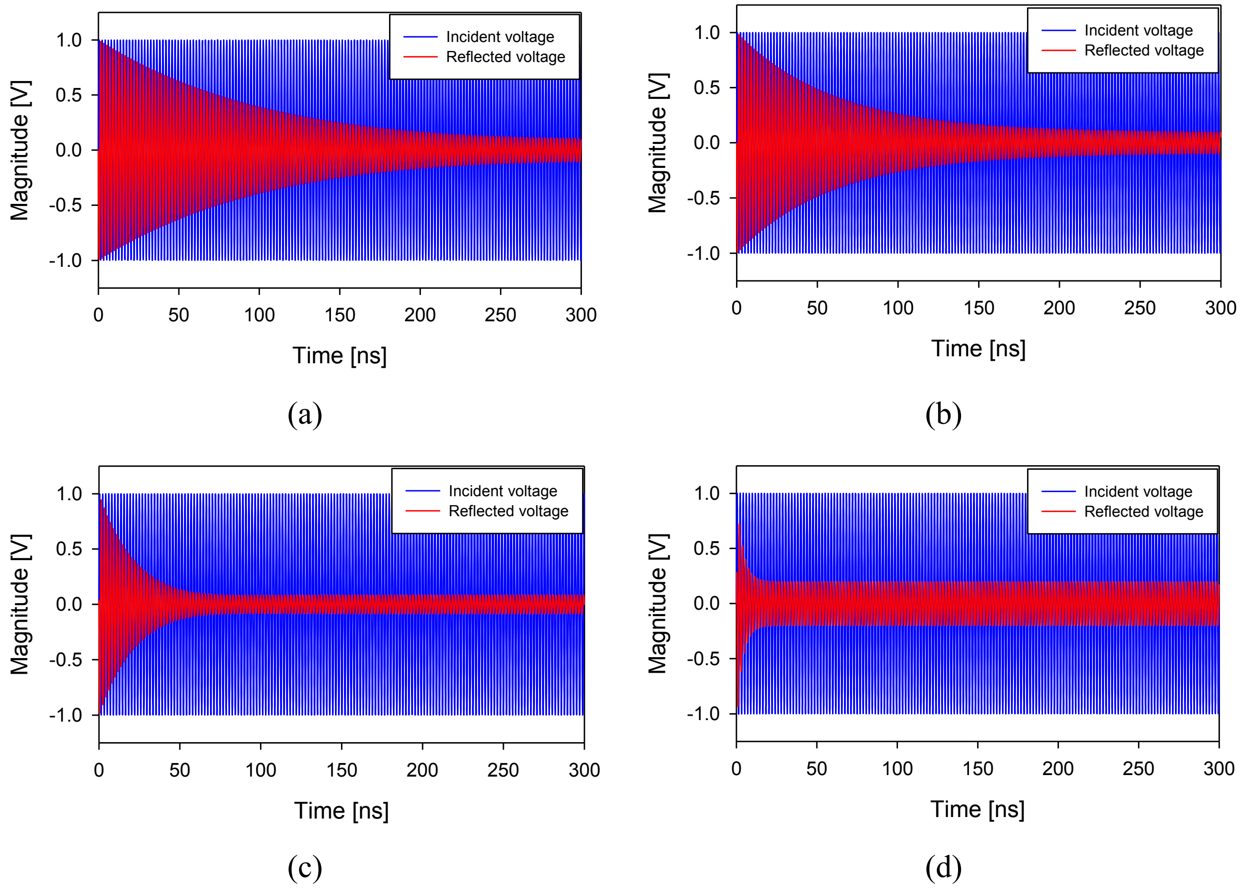

Figure 2.17: Incident and reflected voltage waveforms at the input terminals of: (a) PIFA 1, (b) PIFA 2, (c) PIFA 3, and (d) PIFA 4, when excited at 530 MHz.

2.4 Sinusoidal Pulse Excitation

As discussed in Section 2.3, the transient field response of high-Q antennas can be modeled by an RLC resonator with equivalent resonant frequency and Q factor associated with the excited mode. This equivalence can be used to predict the time-domain response of a high-Q antenna when excited with sinusoidal pulses. Since the time constant of the fields is a function of loaded Q, source impedance impacts the time constant. Figure 2.18 shows two different approaches to feed the antenna with a sinusoidal pulse train. Figure 2.18(a) depicts a modulated source with a matched impedance at the resonant frequency. In Figure 2.18(b), source is modulated by using a switch and therefore, during the OFF-state of the switch, Q is not loaded by the source impedance and the antenna operates as a switched-Q resonator. This is shown in Figure 2.19 that compares the electric fields radiated by PIFA 3 which is fed by a switching source and a modulated source. A small measuring dipole is located in azimuth plane at half a meter away from the antenna to capture the electric field and fields are normalized to the peak values. In Figure 2.19(a), a single period of the electric field is shown where the exciting signal is a sinusoidal pulse starting at 0 and ending at 150 ns. Figure 2.19(b) shows the electric field for a switching source configuration as illustrated in Figure 2.18(b) where a continuous sinusoidal signal is switched off at 150 ns. For both cases, rise-time of the fields is identical and time constant is $\tau_3 = \frac{2Q_3}{\omega_0}$. However, since in the switching source configuration, Q is doubled due to disconnecting the source impedance, time constant of the field is doubled as well.

Figure 2.20 displays a prototype of PIFA 3 and the measured return loss. The antenna is connected to a single pole-double throw switch (ADG918 from Analog Devices) which switches the input port of the antenna between an RF source and a chip resistor as depicted in Figure 2.21. Due to the loading effect of the switch and the insertion loss which is about 0.5 dB at 530 MHz, the measured Q factor is reduced to 12.1. Figure 2.22 shows the time-domain voltage waveforms received by a small measuring dipole at a distance of half-meter from the antenna. The dipole is connected to a high impedance oscilloscope and measures the antenna response to a 530 MHz sinusoidal pulse with duration of 100 ns. Figure 2.22 shows the received voltages for r=50 Ω and r=∞ (open circuit) as well as the exponential functions based on (2.23) in which, the time constant $\tau = \frac{2Q_{meas}}{\omega_0}$ is calculated using the measured Q factor. It can be clearly seen that the envelopes of the measured waveforms agree with the analytical functions extracted from the circuit model.

It is also possible to lower the time constant of the fields by switching to a smaller resistance during the time that source is disconnected as depicted in Figure 2.21. A single pole-double throw switch is used to switch between the source and a resistor, r, at t=150 ns. According to the circuit equivalence presented in Section 2.3, Q factor after switching can be approximated by

$$Q_r = \frac{r \parallel 50}{R_s \parallel 50} Q_{R_S}, \tag{2.28}$$

for R_S=50 Ω, (2.28) can be simplified as

$$Q_r = \frac{2r}{r+50} Q_{50\,\Omega}. \tag{2.29}$$

Figure 2.23 shows the electric fields for r=10, 30, 100 and 300 Ω. It should be noted that (2.29) is valid only if r is sufficiently large such that $Q_r \gg 1$ and antenna can be modeled by a high-Q RLC circuit. Figure 2.24 compares the computed Q from full-wave simulation with Q_r. They merge around Q=25 (r=20 Ω) and both converge to 2×Q_{50}=72 as r→∞, as predicted in (2.29). Therefore, as described in Section 2.2, source impedance can move the location of antenna poles and control the time constants of the fields. This phenomenon becomes significant where a fast switching mechanism along with a desirable transient response is required.

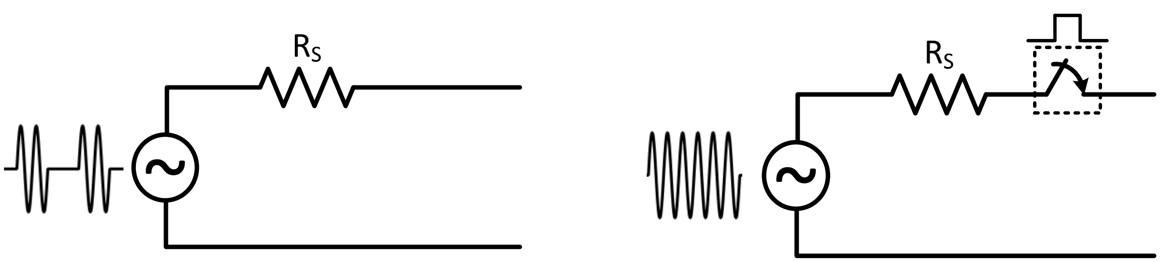

(a) (b)

Figure 2.18: Feeding port for sinusoidal pulse excitation: (a) pulse modulated sinusoid and (b) switching sinusoid.

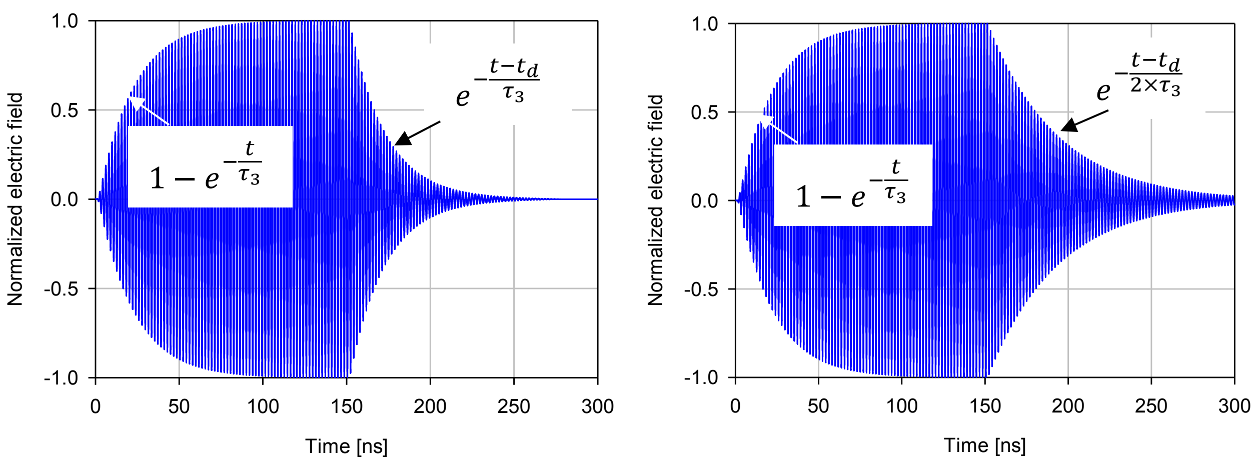

(a) (b)

Figure 2.19: Electric field radiated by feeding the PIFA 3 with (a) modulated sinusoid and (b) switching sinusoid. Pulse width is 150 ns starting from 0, for both cases.

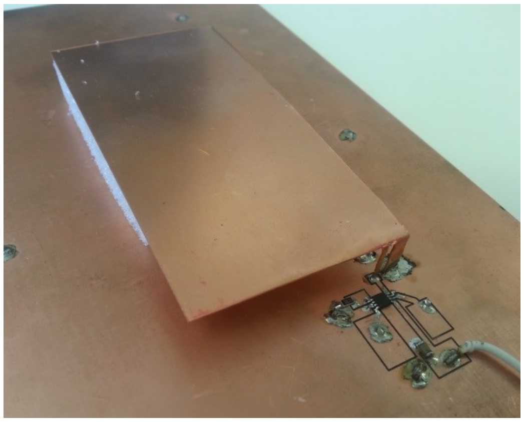

(a)

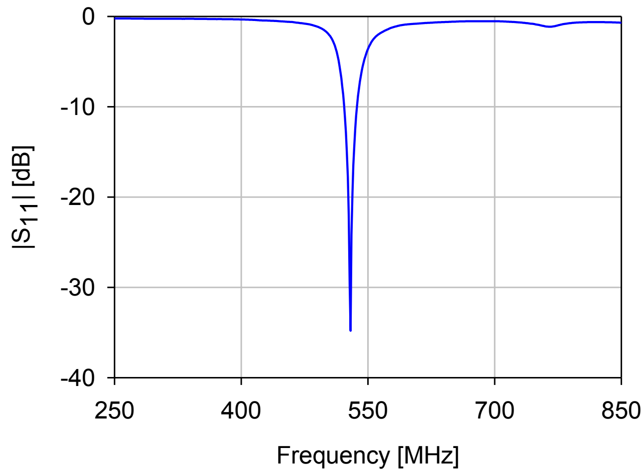

(b)

Figure 2.20: (a) Prototype of PIFA 3 and (b) measured return loss.

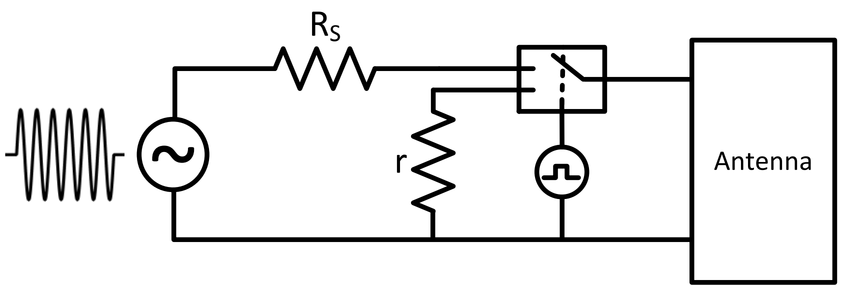

Figure 2.21: Measurement and simulation set-up to study the impact of source impedance on Q factor.

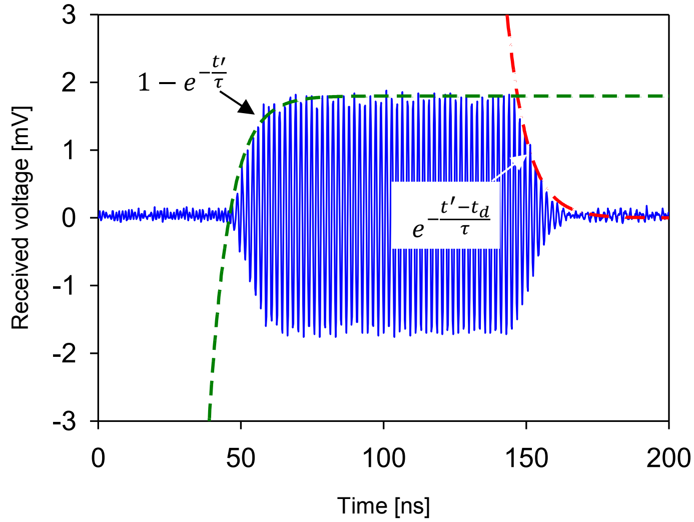

(a)

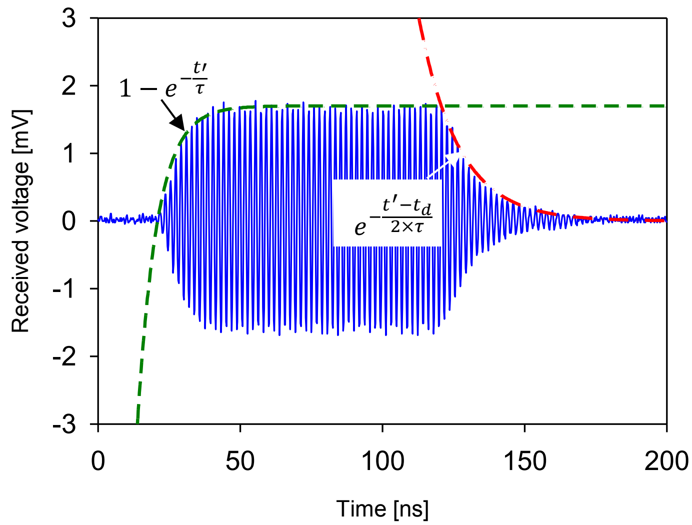

(b)

Figure 2.22: Measured voltage received by a small dipole from PIFA 3 fed by a sinusoidal pulse with duration of 100 ns and (a) r=50 Ω, and (b) r=∞. t' is delayed time according to starting time for each waveform.

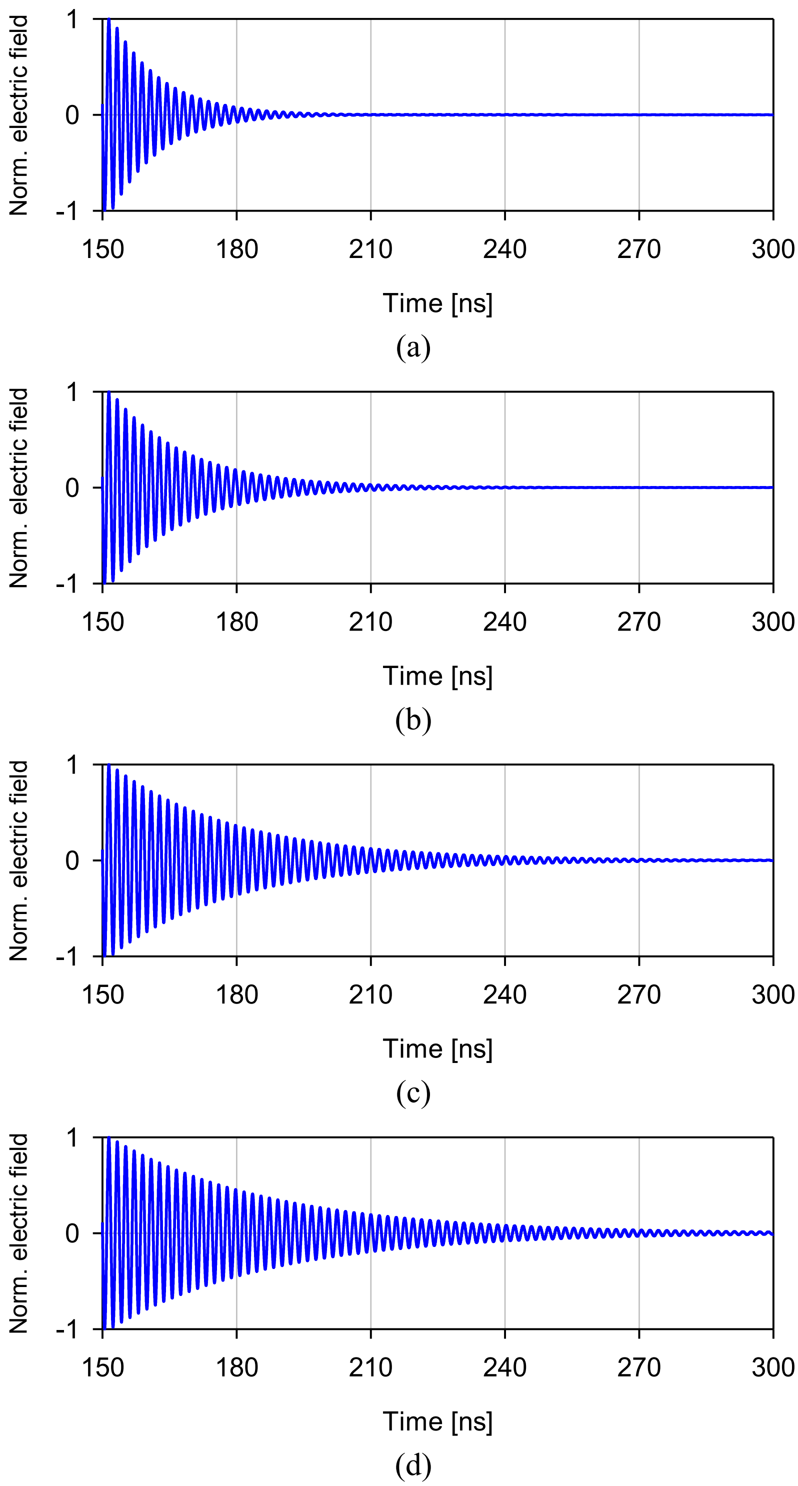

Figure 2.23: Normalized *z* components of the electric fields for different *r* values measured in the azimuth plane at 0.5 m from the PIFA 3: (a) r=10 Ω, (b) r=30 Ω, (c) r=100 Ω and (d) r=300 Ω.

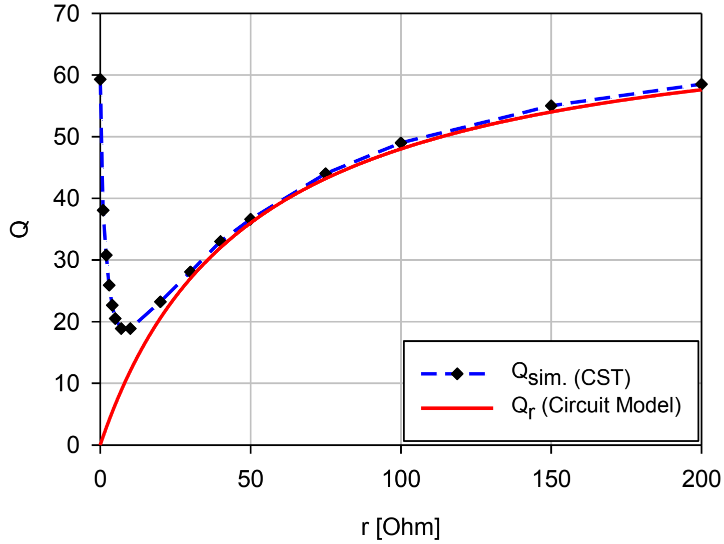

Figure 2.24: Comparison between Q factors calculated based on simulated fields during the source-OFF state according to set-up in Figure 2.21 (dashed blue) and Equation (2.29) (solid red), vs. different r values.

2.5 Chapter Summary

Energy storage mechanism in antennas was explained based on circuit model and the impact of antenna size on the amount of stored energy was illustrated. It was shown that in contrast to the UWB structures, high-Q antennas have a relatively large time constant that is an important factor to be considered in time-varying applications. Time constant and Q factors associated with fundamental mode for different PIFA designs were compared to those of an equivalent RLC resonator and it was shown that for Q>>1, there is an excellent agreement between them. Therefore, time-dependent properties of high-Q antennas can be accurately predicted by their equivalent resonator circuit. The effect of input pulse on the excited modes and early-time response of the fields was also studied and it was shown that the early-time response is a signature of exciting pulse and appears as a copy of input current in the near-field and changes to the time derivative of the input current in the far-field. Furthermore, the transient response to a sinusoidal-modulated pulse was investigated and the impact of source impedance on the time constant and Q factor of the fields was studied.

Chapter 3

Principles of Switched Resonators

Switching a reactive component in a network rearranges the location of the poles and hence, one should expect the variation of damping factor and resonant frequency after the switching instant. Since the input impedance of a switched resonator changes due to the change of a reactive component, the resonator will be tuned out with respect to the source frequency and the input impedance deviates from the matching condition. In this chapter, the transient behavior of an LC resonator with a switched capacitor or inductor is studied. It is demonstrated that switching a reactive component, namely a capacitor, in a high-Q resonator with proper switching rate can preserve the stored energy and couple it onto a different frequency. Switching boundaries are found by continuity of electric charge and magnetic flux. It is shown that if the switching time is synchronous with zero-crossing of the voltage waveform across the switched capacitor or current flowing in the inductor, impulsive components can be avoided and continuity of electric charge and magnetic flux is satisfied without energy dissipation. We use this property to realize a simple binary frequency-shift keying (FSK) modulator with no switching loss.

3.1 Introduction

Switched circuits are distinguished by their time-varying characteristics. The time-varying properties of switched circuits have been utilized in a wide range of applications such as time-varying matching networks, reconfigurable networks, tunable filters, power convertors, and phase shifters [61, 104-110]. Although most switched circuits are traditionally analyzed in a steady-state fashion, there are some reports that present an analytical transient representation for switched circuits [111-117]. The most important consideration in analyzing a switched network is the switching boundaries. Due to the momentary change in stored energies caused by switching the reactive components such as inductors and capacitors, impulsive terms may appear in the solution domain in order to satisfy electric charge and magnetic flux conservation [115]. The main focus of published reports is to find consistent initial conditions for capacitors and inductors and analyze the circuit based on conventional integration method. Even though these efforts are mostly concentrated on providing an efficient model to analyze any arbitrary switched network, they do not give a comprehensive correlation between the concept of energy conservation in time and frequency domains.

In a fully impedance-matched network that consists of reactive elements, any change in the topology of the network may result in shifting the network poles. Pole variation, in turn, causes impedance change at the input port of the network. After the switching instant, the new topology interacts with an independent source as a mismatched component. Depending on the new impedance matrix of the network, part of the incoming energy reflects back to the source and a portion of the energy leaks into the network. However, since the switching imposes initial conditions in reactive components, stored energy is exponentially dissipated in resistive elements. The decay rate in the stored energy is dictated by the new poles which are determined by the new topology after the switching. In other words, the stored energy in the reactive components at source frequency (before switching) will be dissipated in the resistive loads at the new resonant frequency after the switch changes the topology of the circuitry. For transient analysis, if we consider the circuit to be source-free after the switching instant, the stored energy decays exponentially with a decay rate inversely proportional to the new Q factor of the circuit.

In this chapter, a simple LC resonator with a switched capacitor (or inductor) is analyzed. Initial conditions after the switching instant are found using continuity of electric charge and magnetic flux. If the resonator operates in single-mode before and after the switching, the stored energy shifts to a secondary frequency as soon as the capacitance or inductance values change. It is shown that in order to prevent impulsive components in the currents or voltages, switching must occur when the voltage across the capacitor or current flowing in the inductor are zero. Additionally, a high isolation between the two frequencies should be maintained through the impedance mismatch to prevent frequency mixing. This can be achieved by either increasing the difference between the two resonant frequencies or using high-Q resonators. Furthermore, the property of energy shifting in frequency domain can be used to create a frequency-shift keying (FSK) modulation using a switched resonator.

Section 3.2 presents the fundamental concepts of capacitive switching and Section 3.3 discusses the switched-inductor resonators. In Section 3.4, we propose an FSK modulation technique by applying a pulse train as the switching signal. Experimental results are also used to validate the feasibility of the proposed idea.

3.2 Fundamentals of Switched-Capacitor Resonators

Figure 3.1 shows an LC-tank as a resonating structure connected to a resistive load. A single-tone sinusoidal signal, $v_{inc}(t)$, is incident to the input port of the resonator with characteristic impedance Z_0. A voltage-controlled switch is used to change the capacitor from C_1 to C_1+C_2 at $t=t_s$. Incident sinusoidal signal is at resonant frequency of the resonator, $\omega_1=1/\sqrt{LC_1}$. Assuming that the load is matched to the characteristic impedance Z_0, the reflection coefficient at the input port is zero and the voltage at the load in the steady-state is

$$v_R(t) = v_{inc}(t) \ ,(t < t_s) \tag{3.1}$$

At $t=t_s$, C_2 is added to the circuit and changes the resonant frequency of the LC-tank. As a result, the input port will be mismatched with respect to the characteristic impedance, Z_0, and part of the power reflects back to the source. Thus, voltage at the load resistor and input current for $t > t_s$

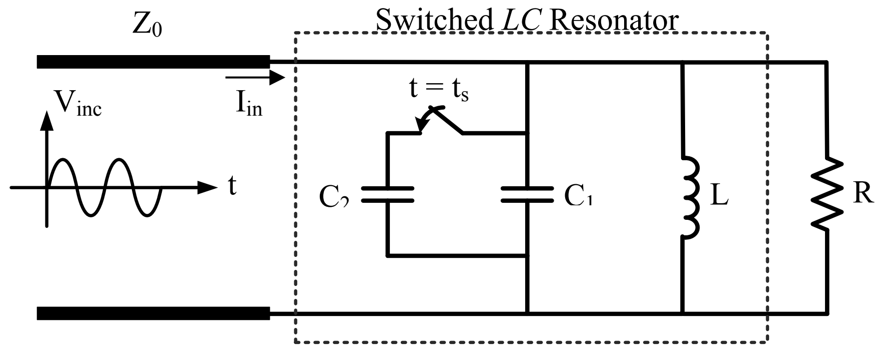

Figure 3.1: Configuration of switched resonator with an incident sinusoidal signal traveling along a transmission line.

can be expressed as sum of the steady-state incident and reflected signals, $v_{ref}(t)$, as

$$v_R(t) = v_{inc}(t)+v_{ref}(t) \tag{3.2}$$

$$i_{in}(t) = \frac{1}{Z_0}\left[v_{inc}(t)-v_{ref}(t)\right]\cdot \tag{3.3}$$

By eliminating $v_{ref}(t)$ from (3.2) and (3.3), we can write the load voltage in terms of input current and incident signal as

$$v_R(t) = 2v_{inc}(t) - Z_0 i_{in}(t), \tag{3.4}$$

where

$$i_{in}(t) = i_C(t) + i_L(t) + i_R(t), \tag{3.5}$$

and $i_C(t)$ represents the current in the switched capacitor. Since the capacitance is time-varying, one can write the relation between the voltage and current of the capacitor as

$$i_C(t) = \frac{dq(t)}{dt} = \mathrm{C(t)}\frac{dv_R}{dt} + v_R(t)\frac{dC(t)}{dt}, \tag{3.6}$$

where $q(t)$ is the total electric charge in the capacitors. Equation (3.6) indicates that a step-like variation in the value of capacitor at the switch-ON time, i.e., $C(t) = C_2 \cdot u(t - t_s) + C_1$ results in an instantaneous current as

$$i_C(t) = \mathrm{C(t)}\frac{dv_R}{dt} + v_R(t_s).\, C_2\delta(t - t_s). \tag{3.7}$$

Equation (3.7) describes the presence of an impulsive component in the capacitor current when an ideal switch is applied to the capacitor. Magnitude of this impulsive component is a function of instantaneous voltage across the capacitor and the value of switched capacitor C_2. On the other hand, at the switch-ON time, t_s, electric charge continuity implies

$$q(t_s^+) = q(t_s^-) \tag{3.8}$$

or

$$C_1 v_R(t_s^-) = (C_1 + C_2) v_R(t_s^+). \tag{3.9}$$

Therefore, the load voltage right after the switching instant can be expressed as

$$v_R(t_s^+) = \frac{C_1}{C_1 + C_2} v_R(t_s^-). \tag{3.10}$$

This discontinuity in the voltage results in a discontinuity in stored electric energy which is a result of using an ideal switch. To satisfy the electric charge continuity, an instant reduction in stored electric energy occurs in the LC-tank right at the switching moment. Ratio of this energy reduction can be written as

$$\frac{\mathcal{E}_e(t = t_s^+)}{\mathcal{E}_e(t = t_s^-)} = \frac{\frac{1}{2}(C_1 + C_2)\, {v_C}^2(t_s^+)}{\frac{1}{2} C_1 {v_C}^2(t_s^-)} = \frac{1}{1 + \frac{C_2}{C_1}} \tag{3.11}$$

This reduction in stored electric energy is a result of voltage drop at the switching moment which is necessary to satisfy the continuity of electric charge.

In addition, boundary value for the inductor current, I_0, can be obtained using the continuity of magnetic flux, φ, as

$$\varphi(t_s^+) = \varphi(t_s^-), \tag{3.12}$$

or

$$L_1 i_L(t_s^-) = L_1 i_L(t_s^+), \tag{3.13}$$

thus

$$i_L(t_s^+) = i_L(t_s^-). \tag{3.14}$$

Therefore magnetic flux continuity requires the current in the inductor to be continuous at the switching moment and hence, energy interaction occurs only between the switched capacitor and the source. For a larger switched capacitor C_2, energy reduction will be more significant according to (3.11). However, if the switching time is synchronous with the zero-crossing of the incident signal, impulsive term in (3.7) will vanish; i.e. if $v_C(t_s) = 0$ then at the switching moment instantaneous electric charge in the capacitor is zero and all stored energy is accumulated in the inductor in the form of magnetic energy. Therefore, the amount of stored energy will be preserved and won't be disturbed by the switching procedure. This energy will be dissipated in the resistive load at a secondary resonant frequency after the switching instant.

For $t > t_s$, voltage at the load is composed of two frequency components. The first component is a leakage from the incident signal at frequency $\omega_1 = 1/\sqrt{LC_1}$ which is mismatched to the input impedance of the resonator. Magnitude of this component is dictated by the mismatch factor. The second frequency component ω_2 is due to a transient response produced by initial conditions of the inductor and capacitor in a source-free RLC circuit. Since we are interested in shifting the stored energy into the frequency ω_2 after the switching instant, leakage from the incident signal should be minimized. It is obvious that the maximum mismatch can be achieved by choosing the capacitor C_2 such that ω_2 is far enough from ω_1 or alternatively, if the resonator has a high Q factor and bandwidth is sufficiently narrow, a large mismatch factor can be achieved by a small frequency deviation. If the incident signal is $v_{inc}(t) = V_s \sin(\omega_1 t)$ and total capacitance is represented by $C_{tot} = C_1 + C_2$ such that $\omega_2 = 1/\sqrt{LC_{tot}}$, the leakage voltage at the load can be expressed as

$$V_{leak}(\omega_1) = \frac{V_s}{1 + j\frac{Q_2}{2\omega_1\omega_2}(\omega_1^2 - \omega_2^2)}, \tag{3.15}$$

thus

$$v_{leak}(t) = \frac{V_s}{\sqrt{1 + N^2}} si\,n(\omega_1 t - tan^{-1} N), \tag{3.16}$$

where

$$N = Q_2 \cdot \frac{\omega_1^2 - \omega_2^2}{2\omega_1\omega_2}. \tag{3.17}$$

The unloaded quality factor, Q_2, in (3.17) is calculated at ω_2. Equation (3.16) denotes that the magnitude of the leaked signal at the source frequency, ω_1, is inversely proportional to the Q factor of the resonator multiplied by difference of squares of resonant frequencies. As previously mentioned, for a high-Q resonator, source is well-isolated from the load after switch-ON time and the only significant frequency at the load is ω_2.

Figure 3.2 shows a simple RLC resonator and its equivalent topology before and after the switching. The RLC circuit with a switched capacitor is fed by a matched source (R_L=R_S) at frequency $f_1 = 1/2\pi\sqrt{L_1 C_1}$. At t=t_s, the capacitor C_2 is added to C_1 which was resonating together with the inductor L. The switched capacitor will change the steady-state resonant frequency to $f_2 = 1/2\pi\sqrt{L_1(C_1 + C_2)}$ where the new input reactance is zero and hence, the source will be mismatched with respect to the input impedance of the new circuit topology. If the mismatch factor is high enough, the source will be totally isolated from the resonator. However, the stored energy in the capacitor and inductor before the switching instant will be discharged to the load at a different frequency which is determined by the switched capacitor as illustrated in Figure 3.2(c) which shows the equivalent topology of the circuit after the switching moment.

The voltage across the load according to the equivalent topology in Figure 3.2(c) can be expressed as

$$v_R(t') = \mathrm{e}^{-\alpha t'}[V_1 \sin(\omega_d t') + V_2 \cos(\omega_d t')], \tag{3.18}$$

where $t' = t - t_s$. The α and ω_d are damping factor and damped resonant frequency, respectively, given by

$$\alpha = \frac{\omega_2}{2Q_2} \quad ; \quad \omega_d = \omega_2\sqrt{1 - \frac{1}{4{Q_2}^2}}\,. \tag{3.19}$$

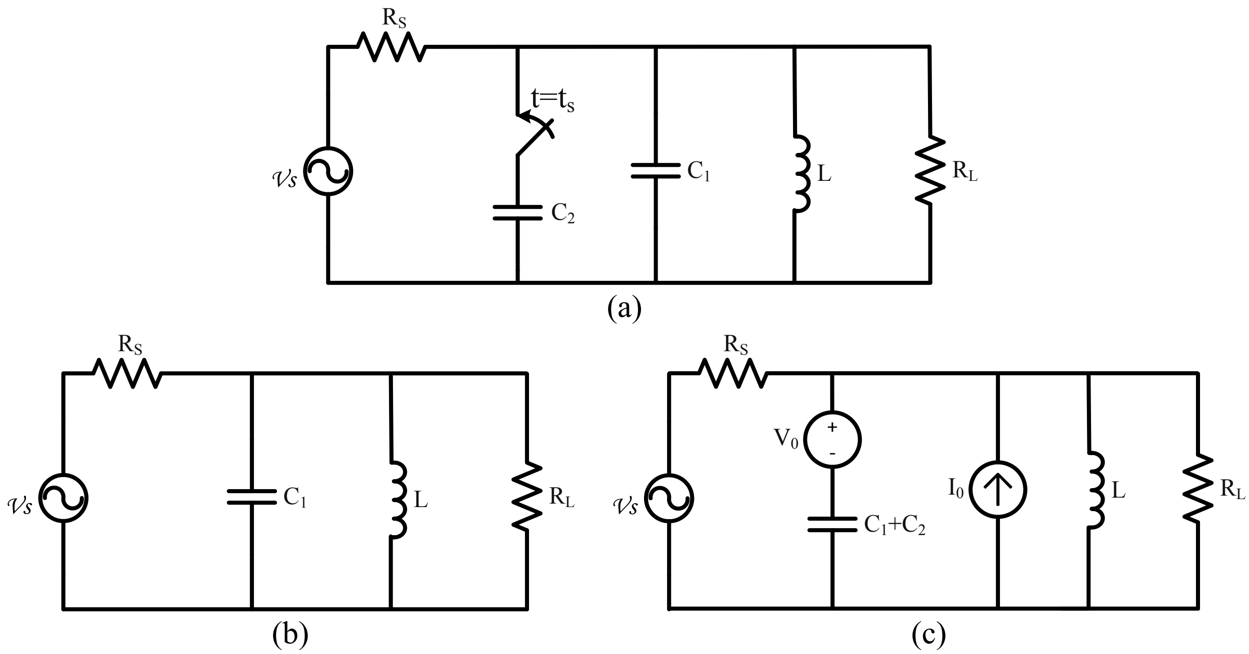

Figure 3.2: (a) Topology of the switched RLC circuit fed by a matched source (R_L=R_S) at frequency f_1 and its equivalent topologies: (b) before and (c) after the switching moment.

For a high-Q resonator (Q_2>>1), damped resonant frequency can be approximated by steady-state resonant frequency $\omega_2 = 1/\sqrt{L(C_1 + C_2)}$

$$\omega_d \approx \omega_2\,\cdot \tag{3.20}$$

The voltages V_1 and V_2 are determined by initial conditions

$$V_1 = \frac{1}{\omega_d}\left(\alpha V_0 + \frac{I_0}{C}\right) \quad ; \quad V_2 = V_0, \tag{3.21}$$

where C is total capacitance, C_1+C_2, and Q_2 is the loaded quality for $t > t_s$. Initial voltage of the capacitor, V_0, and initial current of the inductor, I_0, can be calculated using continuity of electric charge and magnetic flux as shown in (3.10) and (3.14) to give

$$V_0 = v_R(t_s^+) = \frac{C_1}{C_1 + C_2} v_R(t_s^-), \tag{3.22}$$

$$I_0 = I_L(t_s^+) = I_L(t_s^-). \tag{3.23}$$

According to (3.22), a voltage discontinuity occurs across the capacitors to compensate the abrupt variation of the capacitance. The voltage discontinuity in turn, imposes an energy loss in the capacitors. Therefore, by switching a capacitor at $t=t_s$, part of the electric stored energy in the capacitor dissipates in the source impedance. Since the inductor current is continuous according to (3.14), stored magnetic energy is not interrupted at the switching time and therefore, the amount of energy reduction can be expressed as the variation of stored electric energy

$$\begin{aligned} \Delta W = \Delta W_e = W_e|_{t=t_s^+} - W_e|_{t=t_s^-} &= \frac{1}{2} C_1 |v_R(t_s^-)|^2 - \frac{1}{2}(C_1 + C_2)|v_R(t_s^+)|^2 \\ &= \frac{1}{2} C_1 |v_R(t_s^-)|^2 \left(\frac{1}{1 + C_1/C_2}\right). \end{aligned} \tag{3.24}$$

Equation (3.24) suggests that if $v_R(t_s^-) = 0$, entire stored energy will be preserved. Therefore, one may set the switching time such that the voltage across the capacitor is zero and the current of the inductor is at maximum at the switching moment. Assuming t_s is synchronous with zero-crossing of the incident signal, initial values for voltage and current can be found as

$$V_0 = 0 \;\; ; \;\; I_0 = \frac{V_s}{2L\omega_1} \cdot \tag{3.25}$$

Initial conditions in (3.25) together with (3.21) and (3.18) yield the voltage at the load,

$$v_R(t') = \frac{V_s}{2LC\omega_1\omega_d} e^{-\alpha t'} \sin(\omega_d t') = \frac{V_s}{2} \frac{{\omega_2}^2}{\omega_1\omega_d} e^{-\frac{\omega_2}{2Q_2}t'} \sin(\omega_d t') \cdot \tag{3.26}$$

By substituting (3.20) into (3.26), (3.26) can be simplified to give

$$v_R(t') = \frac{\omega_2}{\omega_1} e^{-\frac{\omega_2}{2Q_2}t'} \left[\frac{V_s}{2}\sin(\omega_2 t')\right]. \tag{3.27}$$

Equation (3.27) depicts that for zero-crossing switching boundary, the first peak after switching occurs at $t = t_s + T_2/4$ and takes a value of $\frac{\omega_2}{\omega_1} e^{-\frac{\pi}{4Q_2}} V_s/2$ that can be approximated by $\frac{\omega_2}{\omega_1} V_s/2$ for a high-Q resonator. Since the amplitude of the steady-state voltage before the switching is equal to $\frac{V_s}{2}$, the ratio of two consequent peaks before and after the switching instant is equal to the ratio of frequencies

$$\frac{V_{peak(>t_s)}}{V_{peak(<t_s)}} \approx \frac{f_2}{f_1} \cdot \tag{3.28}$$

For a maximum initial value, first peak occurs at t_s^+ and its value is $\frac{C_1}{C_1+C_2} = \left(\frac{f_2}{f_1}\right)^2$. If the switching instant is matched with zero-crossing of the voltage, total dissipated energy for $t > t_s$ can be calculated as

$$\begin{aligned} E_{diss} &= \frac{1}{R}\int_0^\infty {v_R}^2(t')dt' = \frac{1}{R}\left(\frac{\omega_2}{\omega_1}\right)^2 {V_s}^2 \frac{2{Q_2}^3}{\omega_2\left(1+4{Q_2}^2\right)} \\ &\approx \frac{1}{R}\left(\frac{\omega_2}{\omega_1}\right)^2 {V_s}^2 \frac{Q_2}{2\omega_2} \cdot \end{aligned} \tag{3.29}$$

Replacing $\frac{Q_2}{\omega_2}$ and $\left(\frac{\omega_2}{\omega_1}\right)^2$ with $R(C_1 + C_2)$ and $\frac{C1}{C1+C2}$, respectively, the total dissipated energy yields

$$E_{diss} = \frac{1}{2} C_1 V_s^2 \cdot \tag{3.30}$$

Equation (3.30) indicates that the total dissipated energy in the load after the switching instant is equal to the stored energy before the switching. Thus, if switching occurs when instantaneous voltage across the capacitor is zero, entire stored energy will be dissipated in the resistive load and there will be no energy loss due to the switching. The switching loss for the case that voltage is at maximum can be evaluated as

$$\begin{aligned} switching\ loss &= \frac{1}{R}\int_0^\infty \left[v_R^2(t')|_{V_0=0} - v_R^2(t')|_{V_0=V_{max}} \right] dt' \\ &= \frac{1}{2} C_1 V_s^2 - \frac{1}{2} C_1 V_s^2 \left(\frac{C_1}{C_1 + C_2}\right) = \frac{1}{2} C_1 V_s^2 \left(\frac{C_2}{C_1 + C_2}\right). \end{aligned} \tag{3.31}$$

Figure 3.3 shows the simulation set-up and results using Agilent Advanced Design System (ADS) software. Component values are chosen to have two resonant frequencies f_1=500 MHz and f_2=300 MHz with Q_1=119 and Q_2=198 before and after the switching, respectively. A single-pole single-throw voltage-controlled switch is used to switch the capacitor C_2. A step function signal $u(t-t_s)$ is employed to trigger the switch at t_s. The source is a sinusoidal at 500 MHz with an amplitude of 2 *V*. Figure 3.3(b) shows the load voltage at t_s=400 *ns* and t_s=400.5 *ns* which correspond to the zero and maximum crossing of the voltage, respectively. As is depicted in Figure 3.3(b), right after the switching instant the voltage waveform at the load shifts to the new resonant frequency, 300 MHz. Also, the magnitude of first peaks for each case agrees with predicted values in (3.10).

Figure 3.4 compares the leakage voltage at the source frequency with the second resonant frequency by decomposing the total voltage in frequency domain and taking each component back to the time domain. As predicted in (3.16), magnitude of the source frequency component after the switching is about 5 mV. Note that Q in (3.16) is unloaded because the source impedance is not included in calculations. Time constant for the second frequency is $\tau = \frac{2Q_2}{\omega_2}$. Therefore, a fall-time from 90% to 10% of the peak voltage can be calculated as $2.2\tau \approx 460\ ns$ which agrees with the simulation results. If the time constant is sufficiently large compared to the duty cycle of the switching pulse, such that certain amount of energy is maintained during the switch-ON state, we are able to switch between two frequencies according to a sequence of binary bits that are triggering the switch signal and therefore, realize a simple FSK modulator. This requires a high-Q resonator such that fall-time is long enough to support the lower limit of required bit-rate. In Section 3.4, a binary FSK modulation using a double-leveled switched capacitor will be discussed.

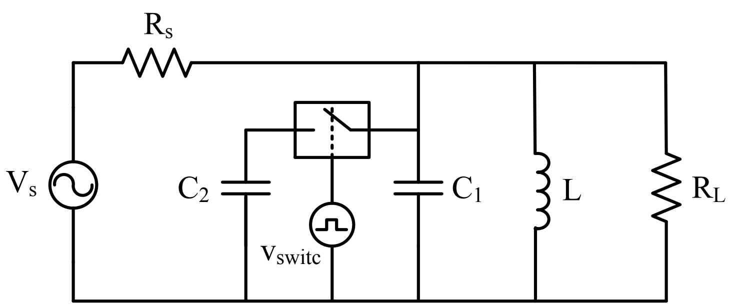

(a)

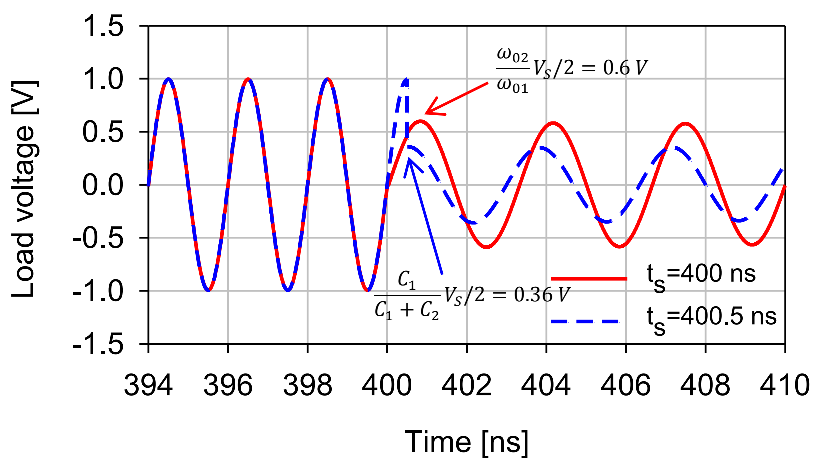

(b)

Figure 3.3: ADS simulation set-up and results: (a) topology of simulated resonator with component value C_1=1.51 nF, C_2=2.69 nF, L=67 pH and $R_S = R_L$=50 Ω, and (b) load voltage around the switching instant.

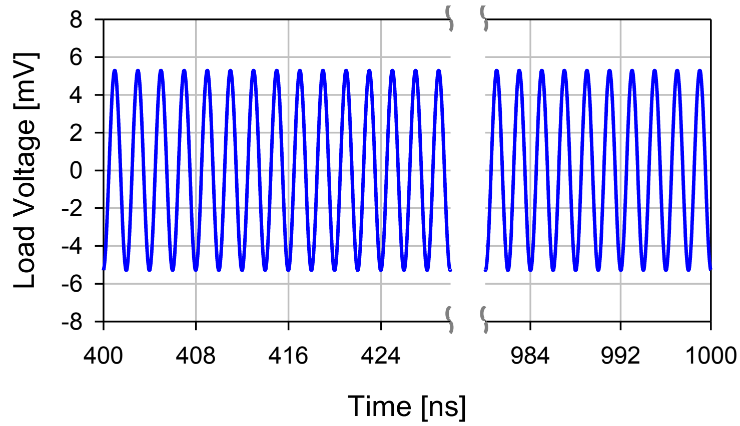

(a)

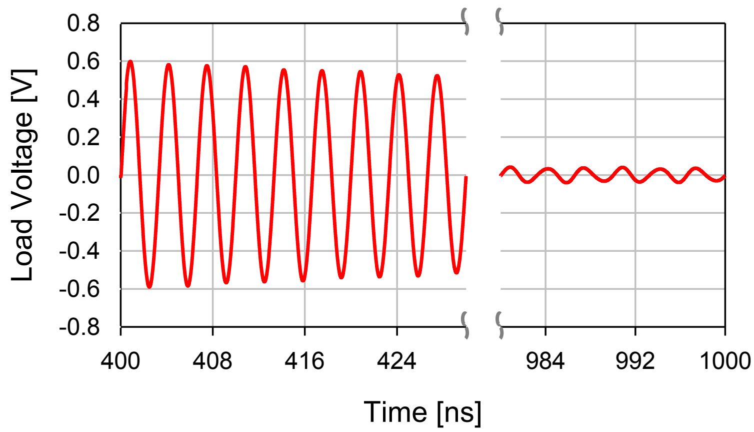

(b)

Figure 3.4: Decomposed load voltage after the switching for resonator in Figure 3: (a) 300 MHz component and (b) 500 MHz component.

3.3 Switched-Inductor Resonator

A similar methodology can be applied to a switched-inductor in order to characterize the impact of switching on the voltages and currents. In a switched-inductor circuit, switching boundary conditions may be determined by the continuity of magnetic flux within the inductors. Figure 3.5 shows a series RLC circuit with a switched inductor. Either L_1 or L_1+L_2 contribute to the resonance at each switching state. In contrast with a parallel switched capacitor circuit, the current is the switched parameter in a series arrangement. Therefore one may consider the continuity of magnetic flux to find the initial values as follows:

$$\varphi(t_s^+) = \varphi(t_s^-) \tag{3.32}$$

or

$$L_1 i_L(t_s^-) = (L_1 + L_2) i_L(t_s^+), \tag{3.33}$$

thus

$$i_L(t_s^+) = \frac{L_1}{L_1 + L_2} i_L(t_s^-). \tag{3.34}$$

The drop of current magnitude at the switching instant imposes a switching loss which appears as a power-drop at the load. Figure 3.6 shows the current when the inductor L_2 is switched in at the maximum current instant. The component values are L_1=1.014 uH, L_2=1.8 uH, C=0.1 pF, and R_S=R_L= 50 Ω. These values result in Q factors equal to 63.7 and 106.1, corresponding to resonant frequencies 500 MHz and 300 MHz, before and after the switching. According to (3.34), the ratio of currents after and before the switching moment is about 0.36 which can be seen in Figure 3.6. The source voltage is a 500 MHz sinusoidal with magnitude 1.

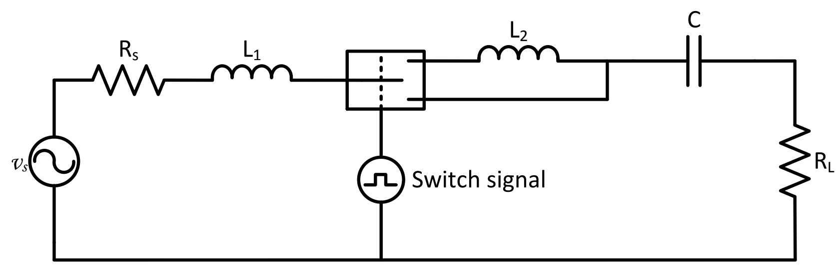

Figure 3.5: Topology of a series switched-inductor circuit.

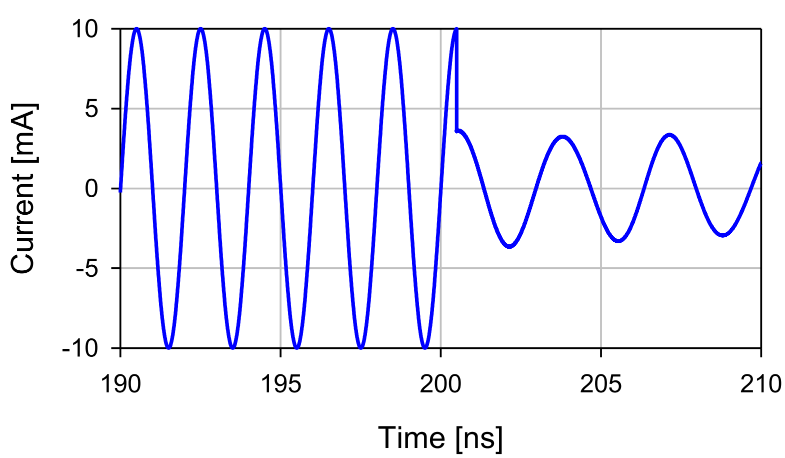

Figure 3.6: Current waveform of the switched-inductor when switched at the maximum current.

Analogous to the switched-capacitor circuit, switching loss can be avoided by synchronizing the switching moments with the current zero-crossing. Figure 3.7 illustrates this case: at the switching instant current waveform changes the frequency from 500 MHz to 300 MHz (Figure 3.7(b)). The transient current at 300 MHz decays with a damping factor equal to $\frac{\omega_2}{2Q_2}$ (Figure 3.7(c)) and once its magnitude is small enough, the leaked current from the source at 500 MHz becomes noticeable (Figure 3.7(d)). Eventually, when the transient 300 MHz component completely dies, the only current component is the source leakage at 500 MHz which is a result of impedance mismatch (Figure 3.7(e)).

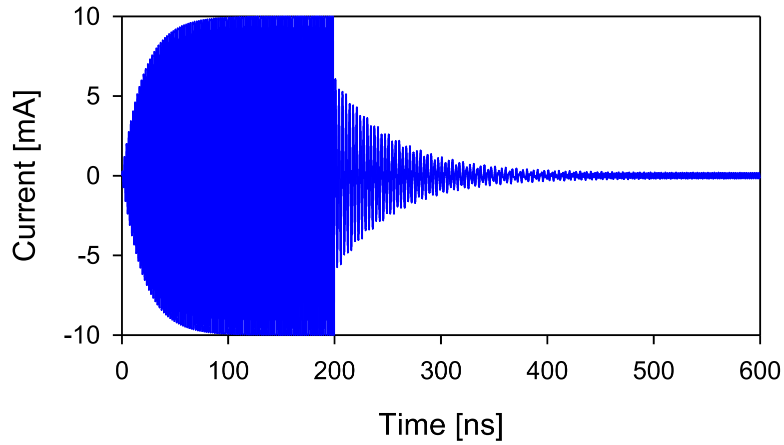

(a)

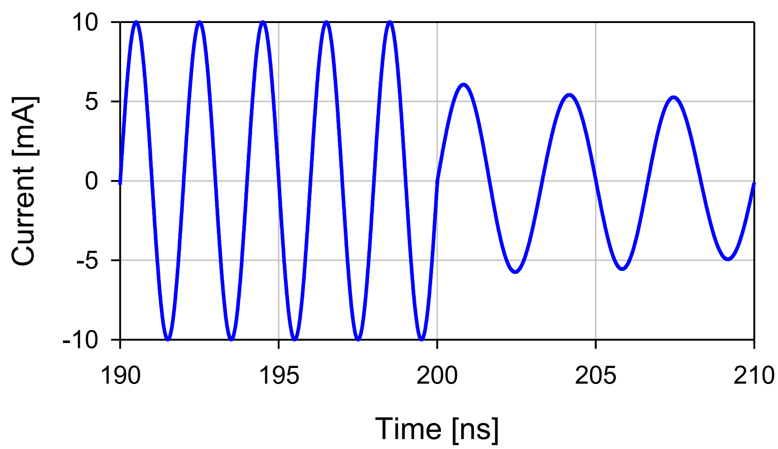

(b)

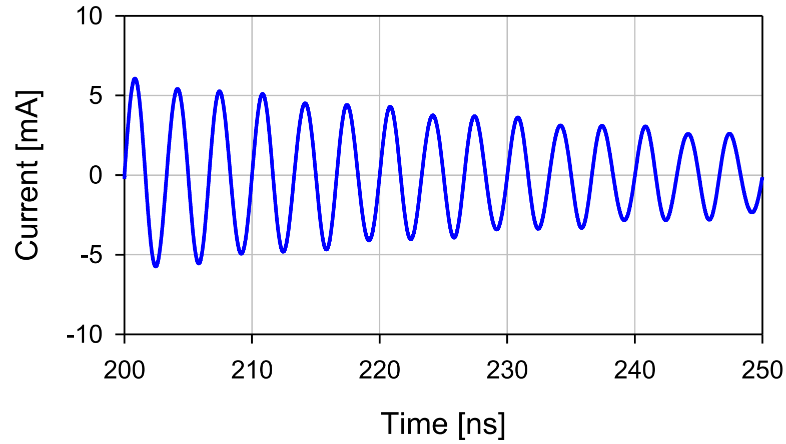

(c)

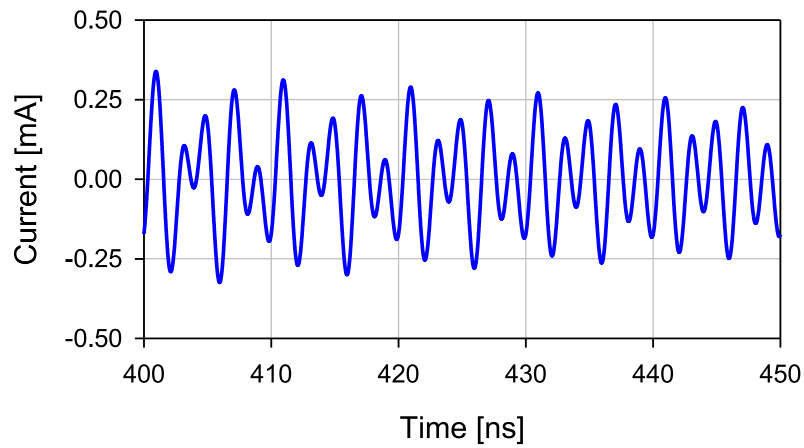

(d)

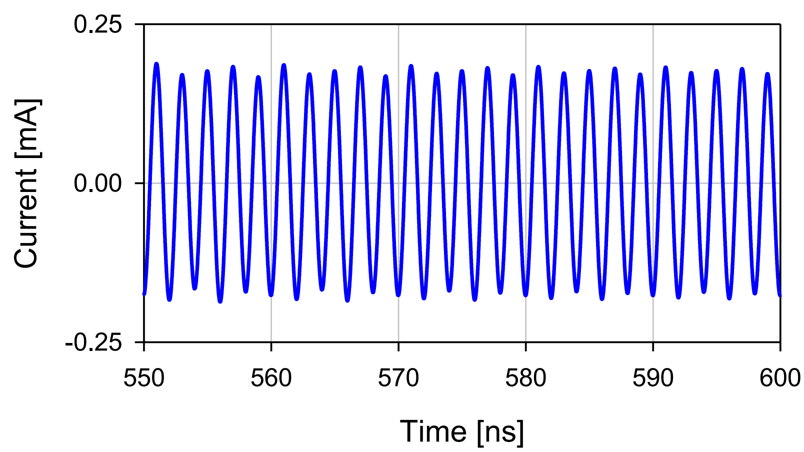

(e)

Figure 3.7: Current waveform of the switched-inductor when switched at current zero-crossing: (a) entire waveform, (b) around the switching instant, (c) transient current at 300 MHz, (d) combination of two frequency components, and (e) leaked current from the source due to impedance mismatch.

3.4 A Binary Frequency-Shift Keying Modulator

In Section 3.2, a switched-capacitor resonator with a step function as the switch signal was analyzed. Decay rate for the source-free frequency component depends on Q factor of the resonator. For a high-Q resonator, we can switch between the source and secondary frequency by using a pulse train as the switch signal and implement a frequency modulation. As discussed previously, in order to preserve the stored energy, switching must be synchronous with zero-crossings of both frequency components. Therefore, both resonant frequencies should be an integer multiplication of the switching frequency. Assuming that duty cycle of the modulating pulse is %50, each pulse represents a pair of 0 and 1 with bit duration of T_b, where $2T_b$ is the pulse period. In order to generate orthogonal FSK signals, separation between frequencies should be an integer multiplication of switching frequency $f_s = 1/ T_s$ [118]. For the resonator in Figure 3.3, examples of switching frequencies that meet all the mentioned considerations are 10, 20, 50 and 100 MHz. Figure 3.8 shows the FSK signals for different switching frequencies. Since each switching pulse represents a pair of 0 and 1, bit-rate is twice of switching frequency. In fact, by using a fast switching mechanism, a simple narrowband RLC resonator excited by a single-tone source can be employed to generate a high data-rate FSK signal. 1st frequency is the same as the source frequency and 2nd frequency can be tuned by the switched capacitor. Moreover, by using a variable capacitor such as a varactor diode, one can easily tune the 2nd frequency. Figure 3.9 shows a measurement set-up for validating the proposed technique. A PIN diode (Avago Tech, HSMP-482B) with 9 ns nominal reverse recovery time is used to create a shunt RF switch. The resonator is made of surface mount components with values 2 nF, 3 nF, 1 nH and 50 Ω for C_1, C_2, L and R_L, respectively. Measured resonant frequencies are about f_1=115 and f_2=70 MHz. the resonator is fed by a 70 MHz sinusoidal source and input power is 8 dBm. Figure 3.10 shows the time-domain measurement results where switching frequency is 2.8 MHz. Although PIN diode switch has a low reverse recovery time, but the fall-time and rise-time of the pulse generator limits the switching speed. Low Q factor of the circuit components is also another non-ideal aspect that affects the measurement. However, it can be seen in Figure 3.10 that the oscillation frequency shifts from source frequency 70 MHz to 115 MHz and decays exponentially. A faster switching configuration with high-Q circuit components can be used to increase the bit rate of the FSK signal with slight variations in the magnitude.

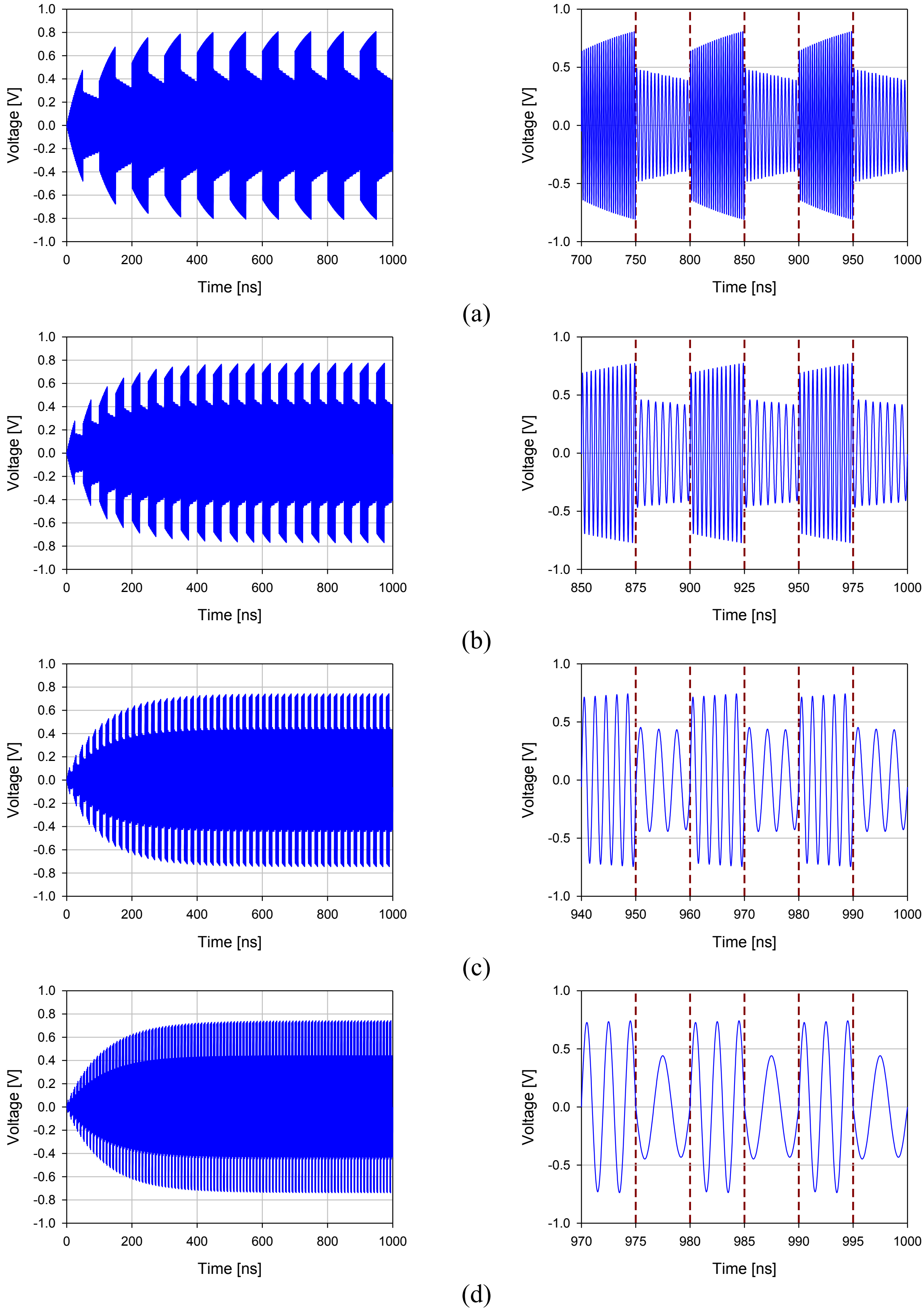

Figure 3.8: FSK signals generated by different switching frequencies: (a) f_{switch}=10 MHz, (b) f_{switch} =20 MHz, (c) f_{switch}=50 MHz, (d) f_{switch}=100 MHz.

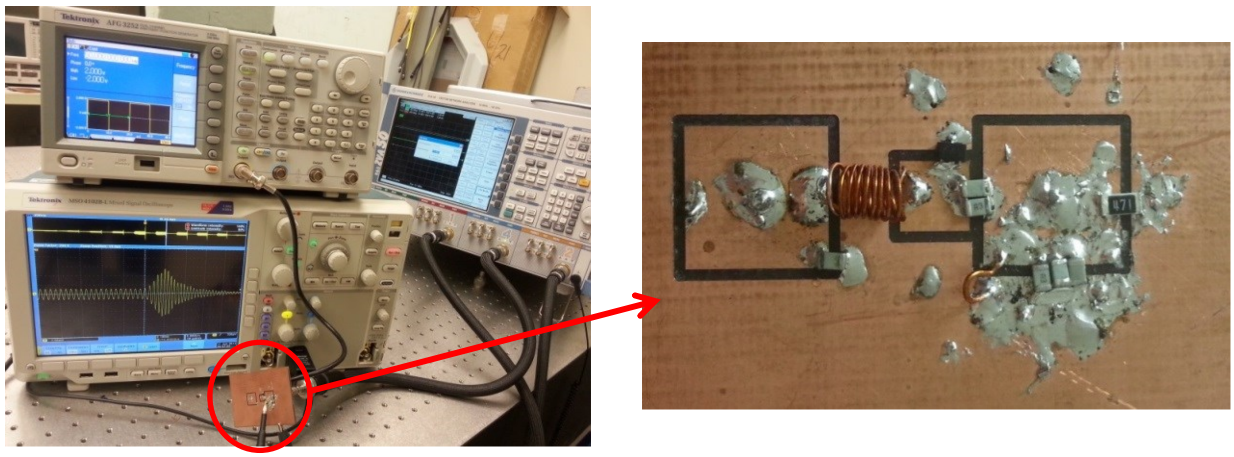

Figure 3.9: Measurement set-up: switching pulse is generated by a Tektronix AFG3252 signal generator and a VNA (R&S ZVA50) is used as RF source. Time-domain signals are measured by a Tektronix MSO4102 oscilloscope.

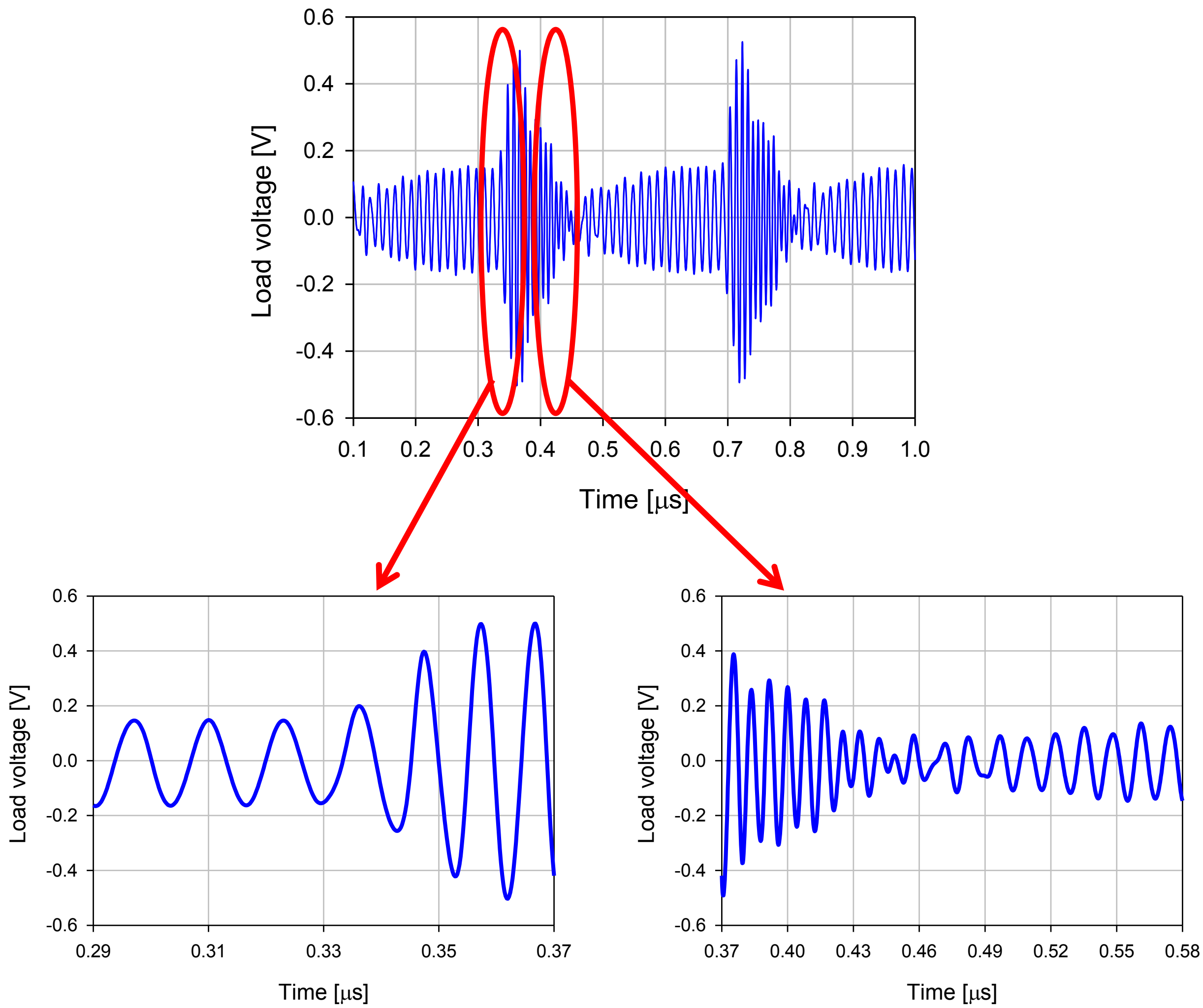

Figure 3.10: Measured voltage at the load.

3.5 Chapter Summary

A transient analysis for high-Q resonators with switched capacitor/inductor was presented in this chapter. Electric charge and magnetic flux continuity were used to find the switching boundary conditions and it was shown that part of the stored energy is momentarily reduced to satisfy the continuity requirements. If switching occurs at the moment that the capacitor is at rest and entire energy is in the form of magnetic energy stored in the inductor in a switched-capacitor circuit (or vice versa for a switched-inductor circuit), the total energy can be preserved. After the switching instant, the energy is shifted to a new frequency due to the topology change in the resonator and is dissipated in the resistive load at the new frequency. This phenomenon was employed to realize an FSK modulation by means of a switched capacitor. It was shown that a bit-rate equal to twice of the switching frequency can be achieved provided that the decaying factor of the transient response is sufficiently small. Experimental results were also presented for validation.

Chapter 4

Switched Antennas I: Theory&Simulations

The rate of wireless data transmission is limited by the antenna bandwidth. In this chapter, an efficient technique to realize a high-rate direct binary FSK modulation by using the transient properties of high-Q antennas is presented. It is shown that if the natural resonance of a narrowband resonant-type antenna is switched at a high rate, the radiating signal follows the variation of resonant frequency and provides a high-rate data-transmission regardless of the narrowband characteristics of the antenna. The bit-rate in this method is dictated by the switching speed rather than the impedance bandwidth. Since the proposed technique employs the antenna in a time-varying arrangement, carrier frequencies are not required to be simultaneously within the antenna bandwidth. When demanded, the antenna is tuned to the required carrier frequency according to a sequence of digital data. Moreover, if the switching frequency is properly chosen such that the amount of stored energy in the near-zone is not dramatically disturbed, any variation in the antenna resonance will instantaneously appear in the far-field radiation due to the previously accumulated energy in the near field. Therefore, depending on the Q factor and switching speed, radiation bandwidth of the antenna can be improved independently from the impedance bandwidth. Furthermore, we show that a single RF source is sufficient to excite both carrier frequencies and the need for a VCO is obviated.

4.1 Introduction

Wireless communication techniques have been widely developed during the past decades due to their extensive applications. One desirable characteristic of most wireless systems is a wide bandwidth. Although there have been lots of studies on different techniques to broaden the bandwidth of small antennas, the antenna bandwidth strictly follows the fundamental physical limit. It is well-understood that in linear time-invariant (LTI) structures, antenna bandwidth is in contradiction with the size and hence, small-size antennas suffer from narrow bandwidth [76, 119, 120]. This problem becomes significant when a high-rate data-transmission is required along with a very small-size antenna. Therefore, designing ultra-wideband (UWB) antennas which are capable of transmitting high data-rate information while occupying a small volume, is one of the challenges that has drawn a great deal of attention [65, 121-131]. For instance, biomedical implants are among the most critical devices that are required to be shrunk in the size while transmitting high data-rate information. Particularly, devices that interact with the nervous systems such as cochlear and visual prostheses need to transmit a large amount of data in order to provide high-resolution sensing for the user [132-134]. Even though a high data-rate can be achieved in broadband systems by increasing the carrier frequency, in low-frequency applications such as biomedical implantable devices, wideband data-transmission remains an open challenge.

The technique proposed in this chapter employs an antenna in a time-varying fashion such that the data-rate is not correlated to the traditional definition of the impedance bandwidth. We show that for a high-Q antenna, if the fundamental natural resonance is shifted over the time, electromagnetic fields that construct the stored energy in the near-zone simultaneously shift to a new resonant frequency. Since the radiative power is tightly coupled to the stored energy of the antenna, far-field radiation responds to any abrupt variation of the antenna resonant frequency provided that the total stored energy doesn't decay significantly. Therefore, if the resonant frequency of the antenna is switched at a high rate, a fast frequency-shift keying (FSK) modulation can be realized directly from the antenna. We also show that a high-Q antenna can be used in the transient mode by imposing initial conditions on the current distribution and therefore, a single RF source is sufficient to excite both resonant frequencies when operating in the transient mode. Hence, an FSK signal can be generated and transmitted by exciting the antenna by only a single-tone source without needing to use a VCO.

To demonstrate this idea, we utilize a high-Q miniaturized antenna loaded by switched capacitors as tuning elements. Similar to a switched resonator, the frequency can be modulated by the switching signal which is coded by a sequence of digital data and an FSK modulation can be generated directly by the antenna. The maximum realized bit-rate is therefore a function of switching rate rather than impedance bandwidth of the antenna.

In Section 4.2, we follow the analogy between a resonant-type antenna and its equivalent circuit model in the time-domain which was introduced in Chapter 2. In Section 4.3 a direct modulation technique using a digitally driven switched antenna is presented. A new class of loop antenna suitable for the proposed direct modulation technique is introduced in Section 4.4. Section 4.5 studies the reflection due to the switching. The impact of non-ideal (lossy) components is investigated in Section 4.6. A straightforward approach is presented in Section 4.7 to achieve switched antenna. Full-wave simulations in this chapter are carried out by CST Microwave Studio while Agilent ADS is used to perform the transient circuit simulations.

4.2 Circuit Model for Small Antennas

Modeling the antennas by lumped-element equivalent circuit has been extensively studied. Wheeler [135] introduced the concept of RLC circuit equivalence in a parallel or series arrangement for TM_{01} and TE_{01} modes, respectively. Schaubert [136] applied Prony's method to Time-Domain Reflectometer (TDR) data to synthesize a rational function with real coefficients that describes the input impedance of the antenna as the summation of poles. Schelkunoff [137] introduced a general representation of impedance functions based on an arbitrary number of resonant frequencies and developed a wideband equivalent circuit. Kim and Ling [138] used a rational-function approximation in conjunction with Cauchy method [139] to find the coefficients by using the frequency-domain data. Also, the Singularity Expansion Method (SEM) [140] and Method of Moments (MoM) [141] have been used to derive equivalent circuit for antennas. Many different approaches to find broadband equivalent circuit for antennas have been proposed as well [142-147].

Nevertheless, high-Q small antennas excite only one spherical mode and input impedance can be matched only at the fundamental resonant frequency. A self-resonant small antenna can be represented by an RLC circuit. As demonstrated in Chapter 2, although an equivalent circuit is found by mimicking the input impedance of the antenna by that of an RLC circuit, transient properties of the radiated fields such as damping factor (or time constant) are also similar to those of the circuit model. Since the radiation resistance of the antenna is lumped into a resistor, one can compare the radiated fields of an antenna excited at the nth resonant mode with the load voltage of an equivalent RLC circuit that is tuned to the resonant frequency of the antenna and resembles the antenna input impedance. Figure 4.1 shows an antenna that operates in a single resonant mode (nth mode) and its equivalent circuit with the same input impedance. Current distribution on the antenna surface for the tuned mode can be expressed as

$$\mathbf{J}_n(\mathbf{r}', s) = \frac{\mathbf{J}_n(\mathbf{r}')}{(s - s_n)(s - s_n^*)}, \tag{4.1}$$

where s_n and s_n^* are the unloaded conjugate poles associated with the nth resonance of the antenna and $\mathbf{J}_n(\mathbf{r}')$ is the spatial current distribution of the nth resonance.

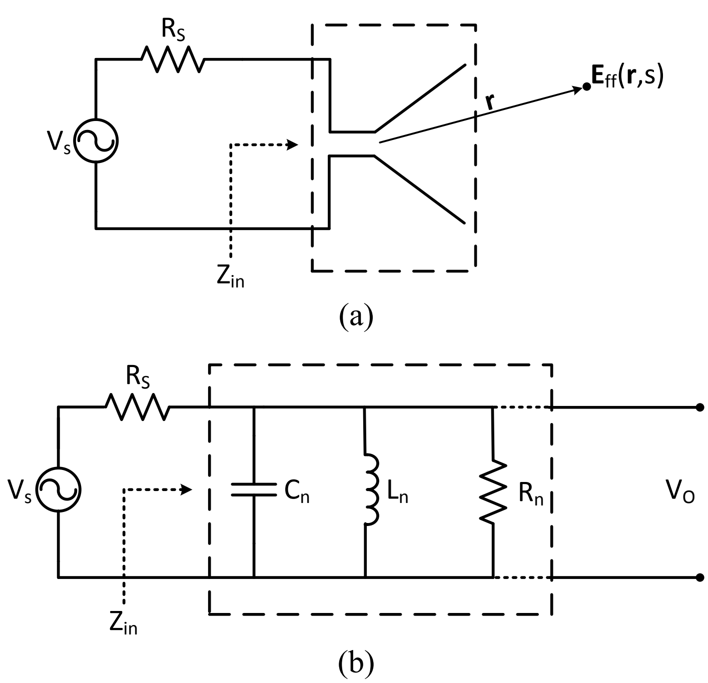

Figure 4.1: (a) A single-mode excited antenna and (b) equivalent circuit model.

Assuming that the current distribution for the nth mode is known, electric far field can be expressed as

$$\begin{aligned}\mathbf{E}_{n}(\mathbf{r},\mathrm{s}) &= \frac{\mu}{4\pi r}\int_{S'} \mathrm{s}.\,\mathbf{J}_{n}\,(\mathbf{r}',s\,)e^{-\frac{r-\hat{\mathbf{r}}\cdot\mathbf{r}'}{c}s}dS \\ &= \frac{\mu}{4\pi r}\frac{s}{(s-s_n)(s-s_n^*)}\int_{S'} \mathbf{J}_{n}(\mathbf{r}')e^{-\frac{r-\hat{\mathbf{r}}\cdot\mathbf{r}'}{c}s}dS'.\end{aligned} \tag{4.2}$$

Equation (4.2) implies that the electric field in the far zone has the same poles as the surface current as it is also shown in details in the theory of singularity expansion method [92]. These poles can be found by using the equivalent RLC circuit as depicted in Figure 4.1(b). Input current and the input impedance of the RLC circuit is

$$I_{in} = \frac{V_s}{R_s + Z_{in}} \tag{4.3}$$

$$Z_{in} = \frac{s/C}{(s-s_n)(s-s_n^*)}, \tag{4.4}$$

where

$$s_n = -\frac{\omega_{0n}}{2Q_n} + j\omega_{0n}\sqrt{1-\frac{1}{4{Q_n}^2}}. \tag{4.5}$$

The ω_{0n} and Q_n are the resonant frequency and unloaded Q factor of the circuit and are defined as

$$\omega_{0n} = \frac{1}{\sqrt{L_n C_n}} \quad ; \quad Q_n = R_n C_n \omega_{0n} \tag{4.6}$$

The load voltage can be now given by

$$V_o = Z_{in}.I_{in} = \frac{\frac{1}{R_s C}s.V_s}{(s-s_{n_{loaded}})(s-s_{n_{loaded}}^*)} \tag{4.7}$$

where loaded poles are

$$s_{n_{loaded}} = -\frac{\omega_{0n}}{2Q_{n_{loaded}}} + j\omega_{0n}\sqrt{1 - \frac{1}{4Q_{n_{loaded}}^2}} \tag{4.8}$$

The $Q_{n_{loaded}}$ is loaded quality factor and is equal to $Q_{n_{loaded}} = (R_n \parallel R_s)C_n\omega_{0n}$. Equation (4.8) gives the electric far-field poles of any arbitrary small antenna that operates in single mode at resonant frequency, ω_{0n}, with corresponding Q factor, $Q_{n_{loaded}}$. The equivalent circuit model can be constructed based on simulated or measured input impedance. Since the poles of the modal currents are preserved in the far zone, the equivalent circuit can be employed to evaluate the transient characteristics of the antenna in the far field. Even though the circuit model doesn't account for the time delay, free-space loss or directional aspects of the radiation such as polarization and directivity, however these parameters don't contribute to the radiation poles and affect only the residue of each pole, i.e. magnitude of the electric fields. Moreover, electric near-field can be also represented by the same poles. Generally, if the current distribution is expanded by the antenna natural poles, any time-derivation or integration of Maxwell's equations will not impact the location of the poles. In other words, damping factor of the fields for each resonant mode is identical at any measurement point.

Equation (4.8) suggests that the damping factor for the electric fields of the nth resonance is equal to

$$\alpha_n = \frac{\omega_{0n}}{2Q_{n_{loaded}}}. \tag{4.9}$$

In small antennas with Q>>1, Q can be well approximated by the inverse of 3-dB impedance bandwidth as [5]

$$Q_{n_{loaded}} = \frac{1}{BW_{3dB}} = \frac{f_{0n}}{\Delta f_{n_{3dB}}}, \tag{4.10}$$

where $\Delta f_{n_{3dB}} = f_{H-3dB} - f_{L-3dB}$. Equation (4.9) implies that damping factor is inversely proportional to the loaded Q of the antenna. Since at higher order resonances electrical size of the antenna i.e. ka is larger, Q factor will be smaller [20]. Therefore, the lowest damping factor is associated with the fundamental mode. By combining Equations (4.9) and (4.10) one finds

$$\alpha_n = \pi . \Delta f_{n_{3dB}}. \tag{4.11}$$

Equation (4.11) shows that the damping factor of the nth resonant field can be found by knowing the absolute 3-dB bandwidth of the antenna. It should be emphasized that Equation (4.11) is based on the equivalent circuit model and is valid only if the antenna is narrowband such that Equation (4.10) holds, which is the case in a typical small-size antenna.

In order to validate Equation (4.11) we shall study the time-domain electric fields of two typical resonant-type antennas: dipole and Planar Inverted-F Antenna (PIFA). In Chapter 2 an extended explanation was presented about the similarity between PIFAs damping factor and their equivalent circuit model. Here we add two more demonstration using a PIFA and a dipole at a different resonant frequency. Figure 4.2 shows the antenna structures. The dipole is a half-wavelength center-fed with a diameter of 0.2 mm and the dimensions of the PIFA are $L \times W \times h$=13cm×7cm×5cm on a 0.3λ×0.6λ ground plane. Both antennas are designed to resonate at 300 MHz. To excite the antennas, a power source matched to 50 Ω with a Gaussian pulse voltage is used in the simulations. As shown in Figure 4.3(a), the full-width at half-maximum (FWHM) of the input pulse is chosen to be $\tau_{FWHM} = 1.35$ ns to ensure that high order modes are not excited and only the fundamental resonance contributes to the radiation. Figure 4.3(b) shows the return loss for each antenna. According to Equation (4.10), Q factors of the dipole and PIFA can be found about 3.9 and 22, respectively. Based on the circuit model, i.e. Equation (4.9) or (4.11), damping factor of the radiated fields for the dipole and PIFA is $\alpha_{dipole} = 0.23\ /ns$ and $\alpha_{PIFA} = 0.04\ /ns$.

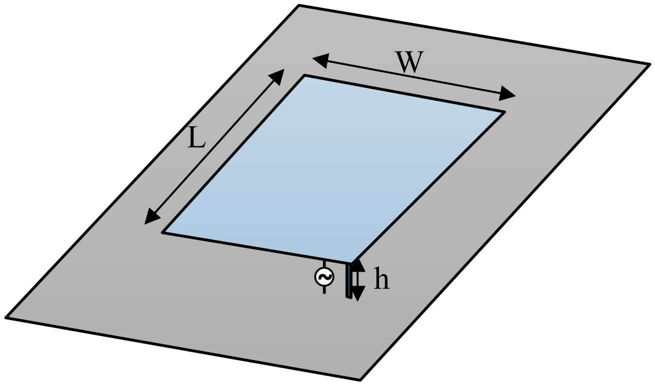

(a)

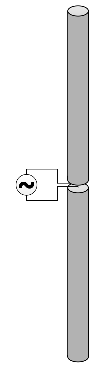

(b)

Figure 4.2: Simulated antenna structures: (a) PIFA and (b) half-wavelength center-fed dipole antenna.

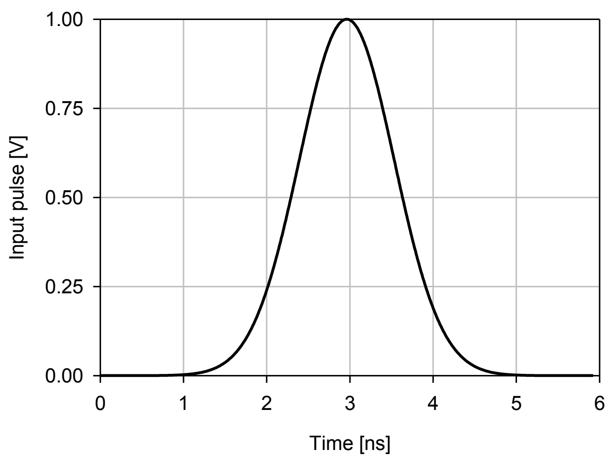

(a)

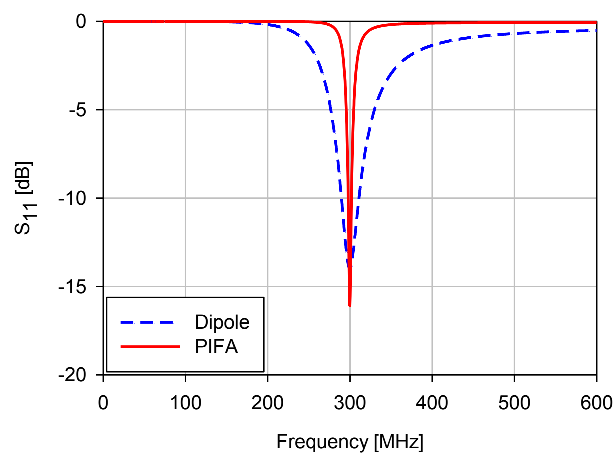

(b)

Figure 4.3: (a) Input Gaussian pulse used to excite the PIFA and dipole, and (b) Simulated return loss for the PIFA and dipole.

Figure 4.4 shows the time-domain z-component of the electric fields in the azimuth plane of each antenna which is measured at a distance of 2 meters from the antennas. For comparison, the decaying exponential function, $E_0 e^{-\alpha(t-t_d)}$, is shown as well. E_0 is the magnitude of the field at the first peak and t_d accounts for the travelling time delay and is set to the first peak time. As illustrated in Figure 4.4, damping factor of the electric fields agrees with that of predicted by Equation (4.11). Moreover, Equation (4.8) indicates that the damped resonant frequency of the circuit model (transient oscillations) is approximately equal to the steady-state resonant frequency if Q>>1.

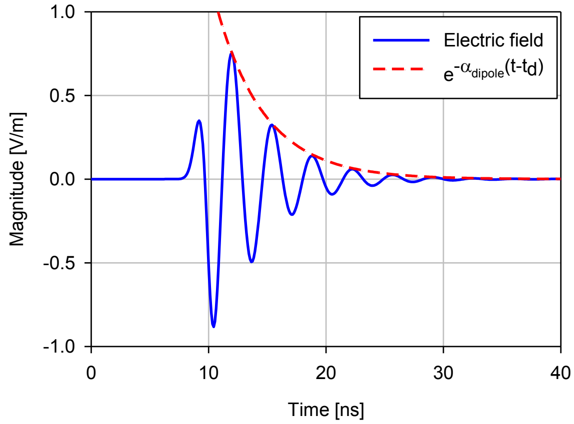

(a)

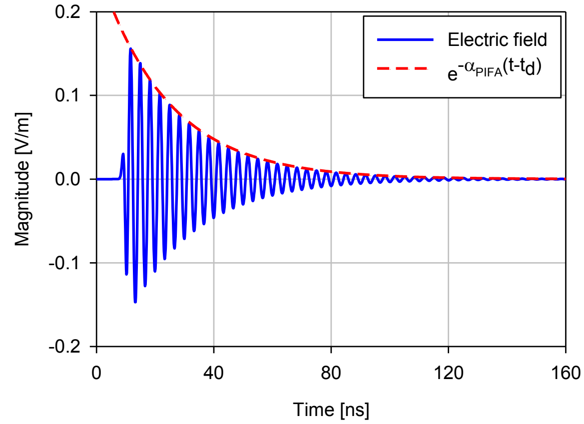

(b)

Figure 4.4: Time-domain z-component of the electric fields in the azimuth plane measured at 2 m from the antennas: (a) dipole and (b) PIFA.

4.3 Direct FSK Modulation Using a Narrowband Switched-Antenna

As discussed in Section 4.2, a single-mode small antenna can be modeled by an RLC resonator that mimics the antenna in both time and frequency domain. As a result, the switched-capacitor technique presented in Chapter 3 can be applied to a small antenna in order to realize a high bit-rate direct FSK modulation. The purpose of employing the switched-capacitor technique to create a direct antenna modulation is to decouple the data-rate from the antenna bandwidth similar to the resonator case [148]. Figure 4.5 shows the block diagram of the direct BFSK modulation. Two capacitors, C_1 and C_2 are used to tune the antenna at f_1 and f_2, respectively. The antenna is fed at f_1 and a single pole-double throw (SPDT) switch controlled by the data sequence is used to switch between the resonant frequencies.

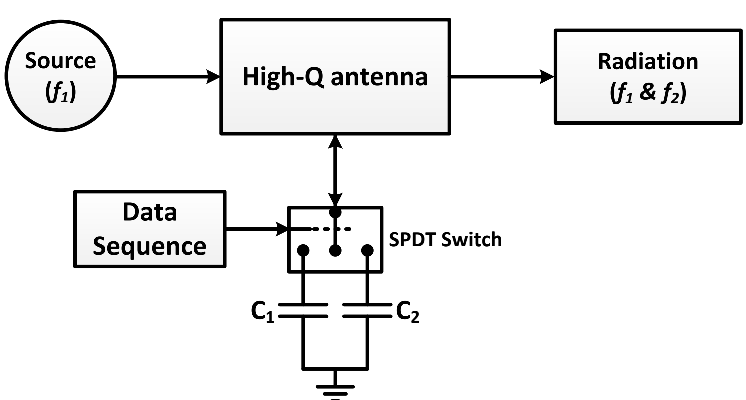

Figure 4.5: Block diagram of the proposed direct BFSK modulation.

Starting at t=0, C_1 loads the antenna and reactive energy begins to build up at frequency f_1. A portion of the energy is stored in C_1 and the rest is stored in the near zone of the antenna. At the moment of zero-crossing of the capacitor voltage, the switch changes its state to connect C_2 and shifts the fundamental natural resonance of the antenna to f_2. Hence, the antenna will operate in the transient mode and radiating fields shift to f_2. Since the capacitor C_1 doesn't face a voltage discontinuity, the stored electric energy is not disturbed and if the capacitor is high-Q, the entire stored energy is preserved until the next cycle of charging. Depending on time constant of the fundamental resonance, after several cycles stored energy in the near-field and capacitors builds up to its maximum. During the transient operation of the antenna, the stored energy within the near-field decays slightly and provides the radiative power. The amount of energy decay depends on the Q factor of the antenna. Therefore, if the antenna has a high Q, total amount of near-field stored energy will not change dramatically and the bandwidth of the antenna will be decoupled from the stored energy, i.e. any abrupt variation in the surface current distribution will appear in the far-field momentarily (transmission delay is ignored). By using a pulse train as the switch control signal where a pair of "0" and "1" can be represented by each pulse cycle, f_1 associated with C_1 represents a "1" and C_2 associated with f_2 represents a "0".

4.4 Switched Electrically-Coupled Loop Antenna (ECLA)

In contrast with the resonator, an antenna may excite higher-order modes. Even though the higher-order modes have larger damping factors, part of the input power may couple to these modes and high-order resonances appear in the radiating fields. A small antenna typically excites the fundamental mode; however, for switching application an antenna structure with only one excited natural resonance is required. Recently, an electrically-coupled loop antenna (ECLA) has been introduced as a dual for planar inverted-F antenna (PIFA) [149]. Since ECLA uses an electrically coupled feeding mechanism, further impedance matching is not required and the antenna can be highly miniaturized. As a result, the antenna operates with a single resonance and a high Q factor. In addition, ECLA shows a good radiation efficiency compared to its counterpart, PIFA. These considerations make the ECLA a suitable choice for the proposed modulation technique.

Figure 4.6 shows the structure of ECLA. The antenna is fed via a capacitive plane (W_f) which is used to match the input impedance. The loop ($L\times H\times W$) resonates along with a tunable capacitive gap (h_c) that tunes the resonant frequency and miniaturizes the antenna.

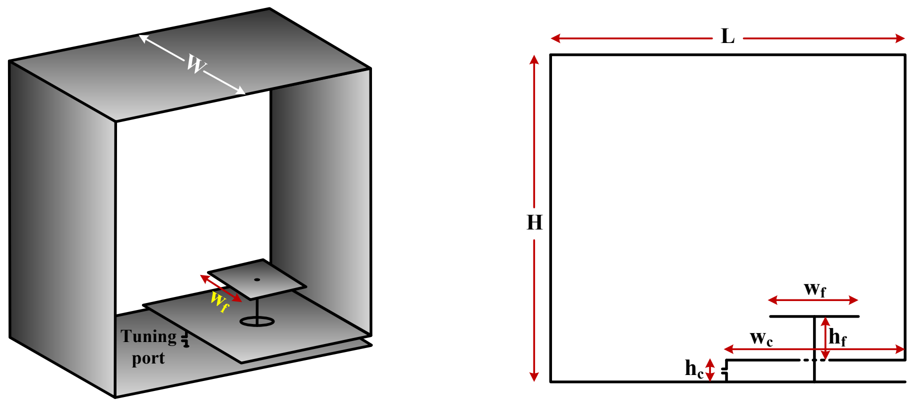

(a) (b)

Figure 4.6: Structure of the electrically-coupled loop antenna (ECLA): (a) perspective view and (b) side view.

Ease of fabrication and measurement is another advantage of ECLA. Since the impedance matching is carried out by a moving capacitive plate, an excellent matching can be achieved as a post-fabrication procedure. Figure 4.7 shows different prototypes of ECLA with measured return loss. Physical dimensions of different designs are listed in Table 4.1. The electrical size of the antennas (diameter of the enclosing sphere) is $\frac{\lambda}{25}, \frac{\lambda}{18}$ and $\frac{\lambda}{52}$ for ECLA 1, ECLA 2 and ECLA 3, respectively. Simulated gain pattern of three prototypes are shown in Figure 4.8. One can see that the doughnut-shape radiation pattern is similar to a magnetic dipole as a dual of loop antenna. The simulated gain for three designs are about -0.8 dB, -0.6 dB and -15 dB for ECLA 1, ECLA 2 and ECLA 3, respectively.

Table 4.1: Physical dimensions of different ECLA designs

	L (mm)	H (mm)	W (mm)	w_f (mm)	w_c (mm)	h_f (mm)	h_c (mm)	f (MHz)
ECLA1	18	11	16	8	10	1	1.5	634
ECLA2	47	42	15	6	8	0.2	1.5	263
ECLA3	100	105	16	12	80	4	0.2	40

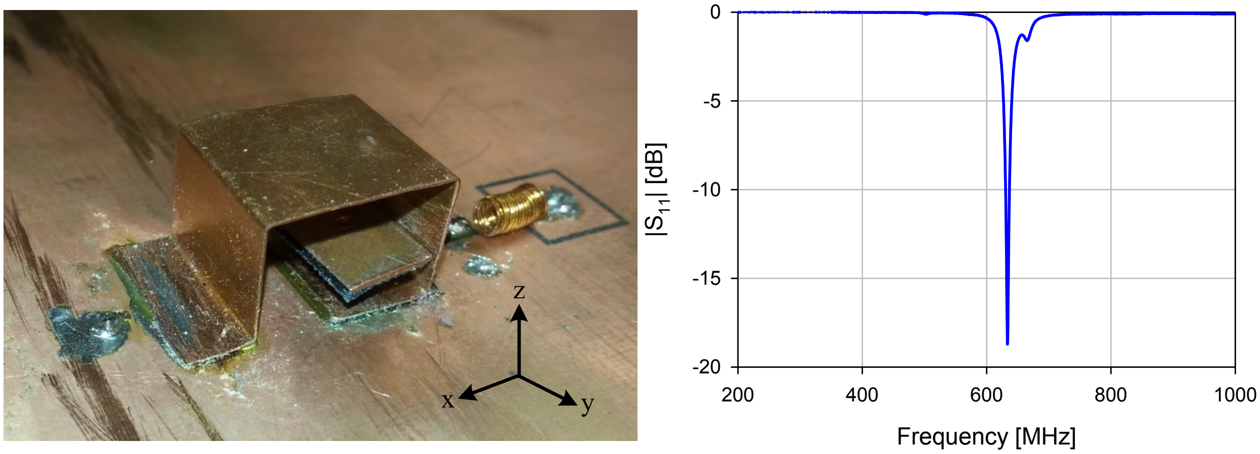

(a)

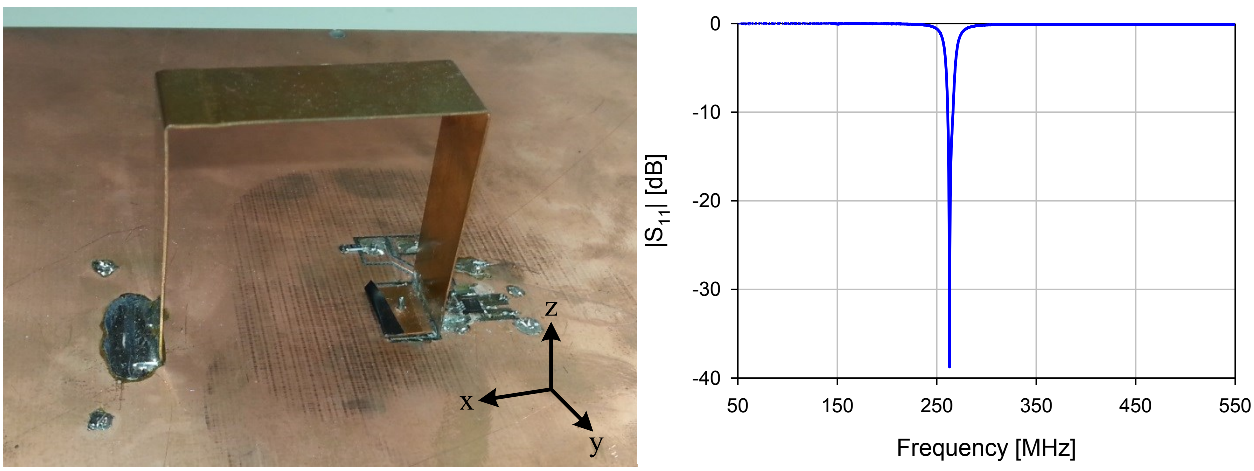

(b)

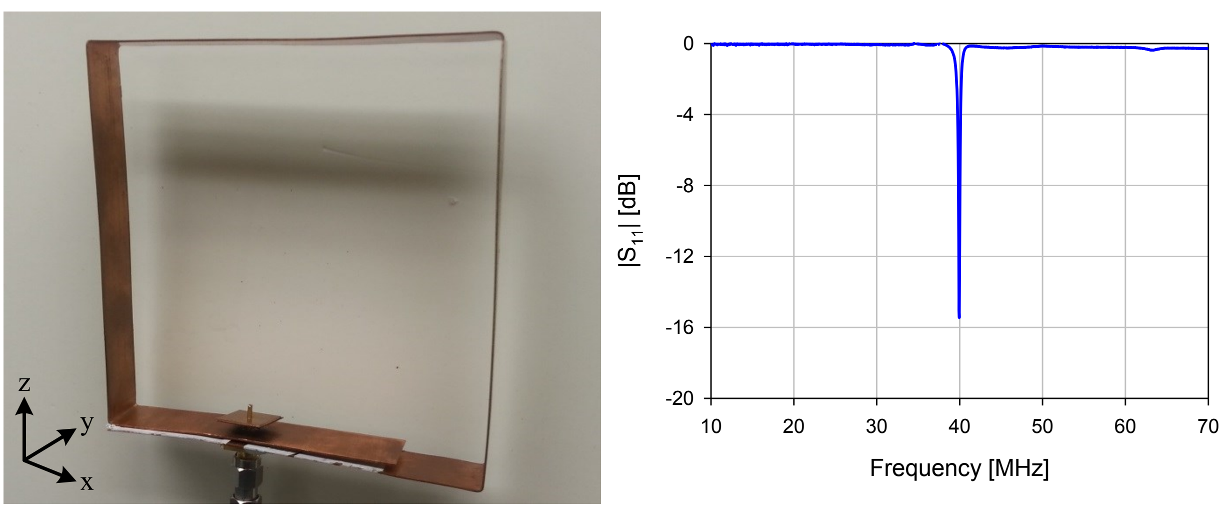

(c)

Figure 4.7: Different prototypes of ECLA and their measured return loss: (a) ECLA 1, (b) ECLA 2, and (c) ECLA 3.

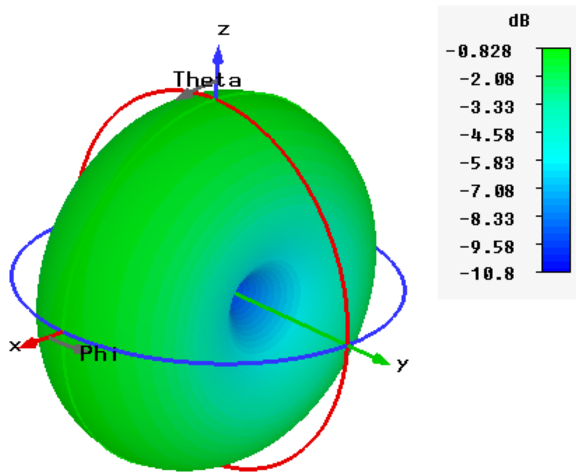

(a)

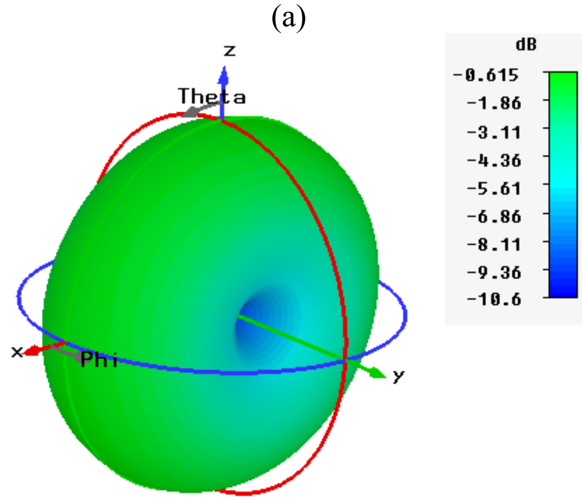

(b)

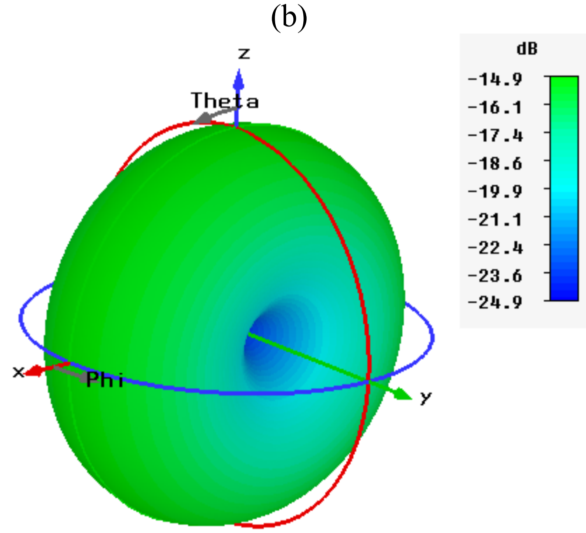

(c)

Figure 4.8: Simulated gain pattern of three ECLA designs: (a) ECLA 1, (b) ECLA 2, and (c) ECLA 3.

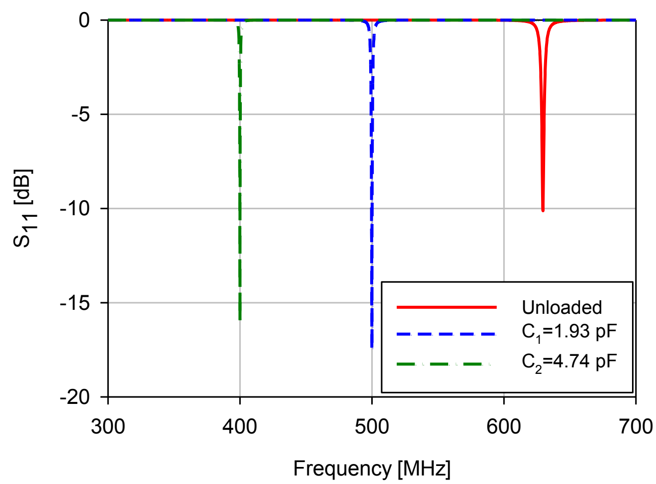

Figure 4.9: Simulated return loss of an ECLA with L=H=20 mm, W=15 mm, w_f = 3.2 mm, h_c =0.5 mm, w_c = 10 mm and h_f =2.5 mm.

In order to change the resonant frequency, the tuning port is located at the edge of the capacitive gap. Therefore, a switched capacitor can be placed in parallel with the capacitive gap and contribute to the antenna resonance. Figure 4.9 shows the simulated return loss of an ECLA with L=H=20 mm, W=15 mm, w_f = 3.2 mm, h_c =0.5 mm, w_c = 10 mm and h_f =2.5 mm. The unloaded antenna resonates at f_0 =630 MHz with 1.65 MHz 3-dB bandwidth ($Q_0 \approx 382$). The electrical dimension of the unloaded antenna is 0.04λ×0.04λ×0.03λ. By loading the antenna with two capacitors C_1 = 1.93 pF and C_2 = 4.74 pF, the resonant frequency can be tuned at f_1 =500 MHz and f_2 =400 MHz with 3-dB bandwidth of B_1 =1.6 MHz and B_2 =0.8 MHz (Q_1 = 312.5 and Q_2 = 500). Figure 4.10 shows the simulation set-up for the switched antenna. A small dipole is placed 1 meter away from the antenna in the E-plane to measure the electric field. The measuring dipole is aligned with the co-pol direction and terminated by a 100 KΩ resistor. As discussed in Chapter 3, in order to preserve the stored energy in the capacitors, switching moment must be synchronous with the zero-crossing of the capacitors voltage. This requires the resonant frequencies to be integer multiples of the switching frequency. It should be pointed out that due to the transmission-line delay, voltage zero-crossings may not be in-phase with the source. This can be compensated by delaying the switch signal such that the switching moment coincides with the voltage zero-crossing of the capacitors. Figure 4.11 shows the voltage of the capacitors in conjunction with the switching signal at 50 MHz. Since the distance between the feeding and tuning ports is small, transmission-line delay would not be remarkable with this antenna configuration.

The switching signal is a two-level voltage waveform. “0” indicates the OFF state of the switch which is associated with the capacitor C_1 and frequency f_1, while “1” indicates the ON state of the switch which puts the capacitor C_2 in charge of the transient radiation at frequency f_1. Figure 4.12 shows the received signal by the measuring dipole for four different switching frequencies: 10, 25, 50 and 100 MHz. Since each pulse represents two bits, the bit-rate is twice the switching frequency. It can be seen that regardless of the extremely narrow bandwidth of the antenna, bit-rate can be as high as required. This achievement is mainly due to two factors. Firstly, the time-varying property of the antenna obviates the need for covering the carrier frequency deviation, $\Delta f = f_2 - f_1$. In other words, the antenna is instantaneously tuned to f_1 and f_2 when logic “0” and “1” are to be transmitted, respectively. Secondly, since the loading capacitors change the natural resonances of the antenna, near- field reactive energy switches between different frequencies. After several switching cycles the stored energy reaches a maximum and afterwards, the fields shift between two resonant frequencies due to the variation of the antenna resonant frequency. The nature of this frequency shifting arises from the variation of antenna poles and is not linked to the input terminal of the antenna where impedance bandwidth is defined. Therefore, if the antenna is sufficiently high-Q and the switching moment is properly chosen such that during the transient mode the stored energy doesn’t discharge dramatically and remains close to its maximum, the conventional impedance bandwidth will not be coupled to the radiation bandwidth and the antenna is able to respond to any fast frequency shifting caused by switching the natural resonances of the antenna.

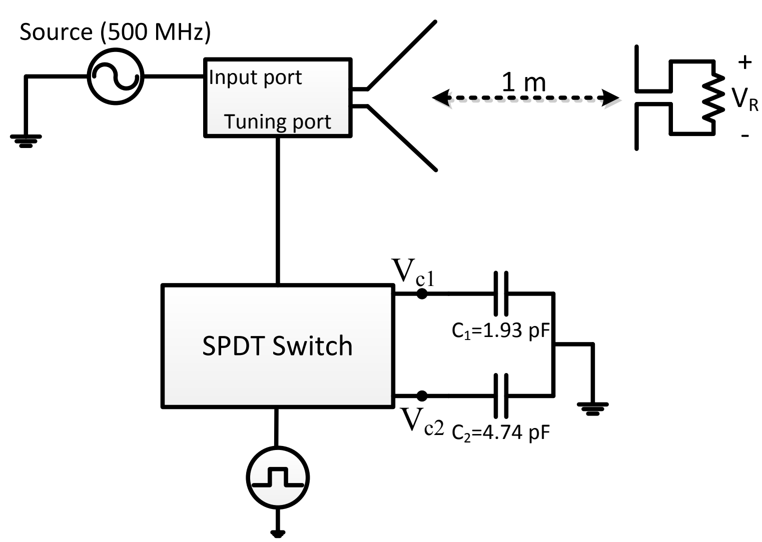

Figure 4.10: Simulation set-up for the switched antenna.

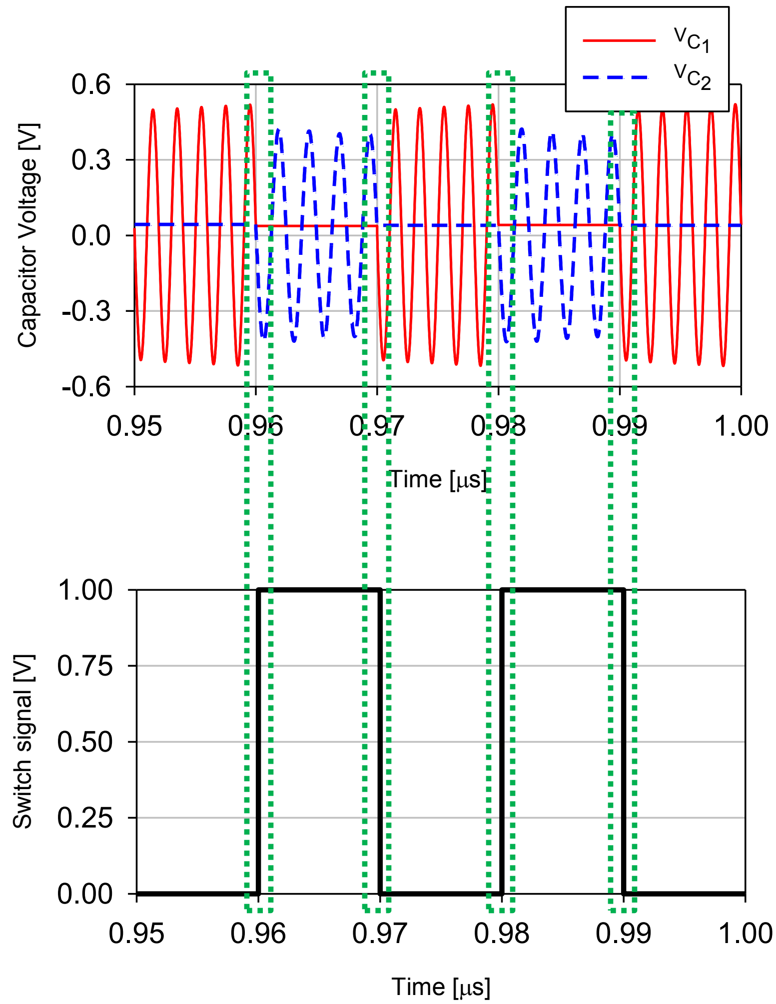

Figure 4.11: Voltage of the capacitors in conjunction with switching signal at 50 MHz.

4.5 Reflection at the Input Port

In order to study the effect of switching at the input port of the antenna, we would observe the time-domain reflected signals. To carry out this study, a directional coupler can be used to simulate the reflection and decompose the reflected waveform into its constituting frequency components. Figure 4.13(a) shows a three-section directional coupler on an FR4 substrate with 1 mm thickness which is simulated in Agilent ADS. Figure 4.13(b) shows the scattering parameters of the directional coupler. The coupling factor at 400 MHz and 500 MHz is between -17.5 dB ~ -15.7 dB while the isolation is -73 dB ~ -70 dB. By terminating the coupling and isolation ports by match loads and feeding the antenna by through port, as depicted in Figure 4.14, we can measure the reflected voltage waveform from the antenna.

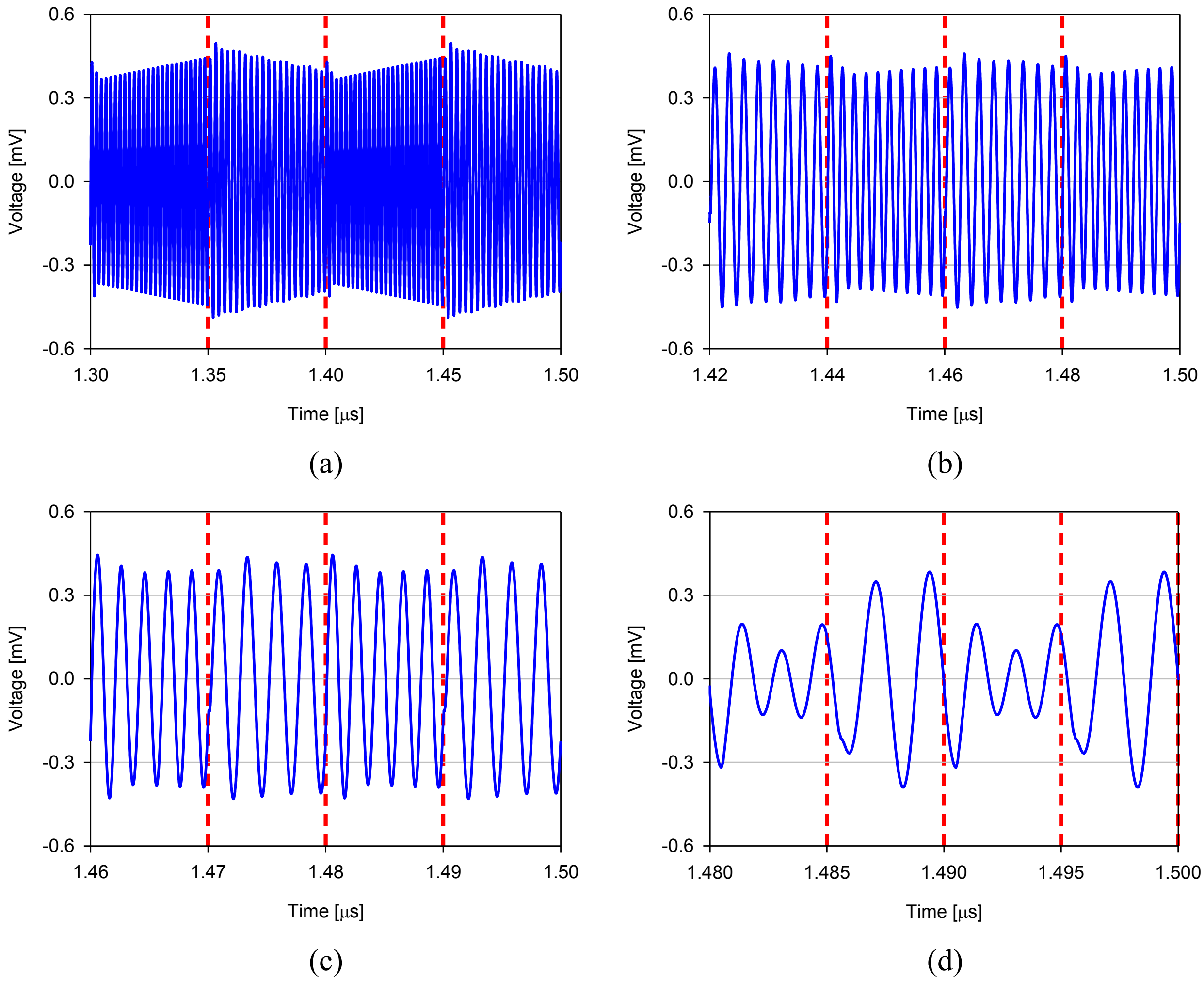

Figure 4.12: Simulated received voltages by the measuring dipole at the switching frequencies: (a) 10 MHz, (b) 25 MHz, (c) 50 MHz and (c) 100 MHz. Antenna is fed by a sinusoidal at 500 MHz and magnitude 100 mV.

Starting from t=0, the antenna is tuned to 500 MHz and fed by a 500 MHz source with 0 dBm power. At t=1 us, antenna is switched to the capacitor associated with resonant frequency 400 MHz. Figure 4.15 shows the entire simulated voltage from t=0 to t=2 us at the isolation port which represents the reflected signal. Since the reflection after the switching is of interest, the voltage waveform from t=1 us to t=2 us is extracted from the total response. Figure 4.16 shows the frequency-domain of the reflection calculated within the time window t=1 us to t=2 us. A narrowband component at 500 MHz and a wider band component at 400 MHz can be seen in the frequency response. This indicates that the duration of source frequency component (500 MHz) is longer than that of the 400 MHz component. In other words, the 500 MHz component which is due to the impedance mismatch is present in the reflected waveform without decaying while the 400 MHz component which is tied to the new pole of the antenna exponentially decays. The time-domain reflected waveform after the switching instant is decomposed into two frequency components as illustrated in Figure 4.17. As explained, the reflection is composed of a constant magnitude waveform at the source frequency and an exponentially decaying waveform at the new resonant frequency. The damping factor of the decaying signal is dictated by the new Q factor of the antenna after the switching instant.

4.6 Effect of non-Ideal Components on the Radiation

Since switched-antennas are required to have a relatively high Q factor, it is important to know how loss can affect the radiated power. The main loss mechanism as will be discussed later is the insertion loss of the RF switches. In addition, the switched capacitors have limited Q factors as well and always impose some loss on the total performance of the antenna. To study the effect of switching insertion loss, small resistors (r_1) are added to the switch model in series as depicted in Figure 4.18. Equivalent series resistance of the capacitors is represented by r_2 and therefore, the overall equivalent resistance can be modeled by $R= r_1+r_2$. Figure 4.19 compares the time and frequency domain waveforms of the received voltage at the open-circuited input port of the measuring dipole for different R values at the switching frequency 25 MHz.

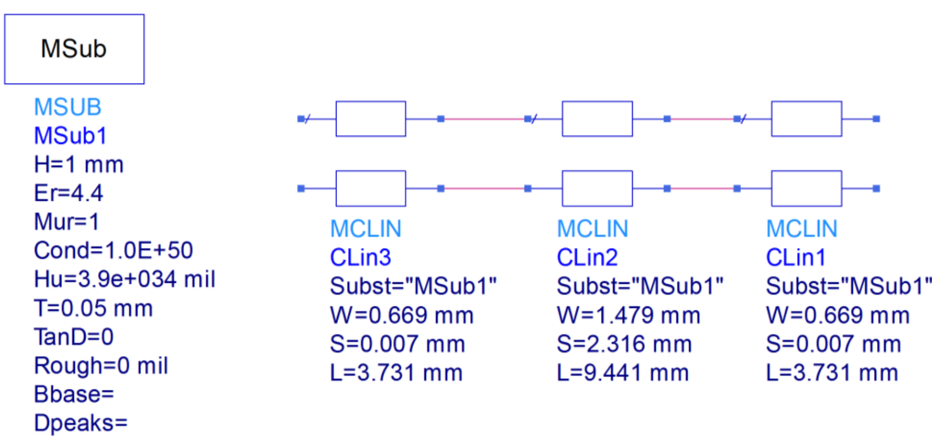

(a)

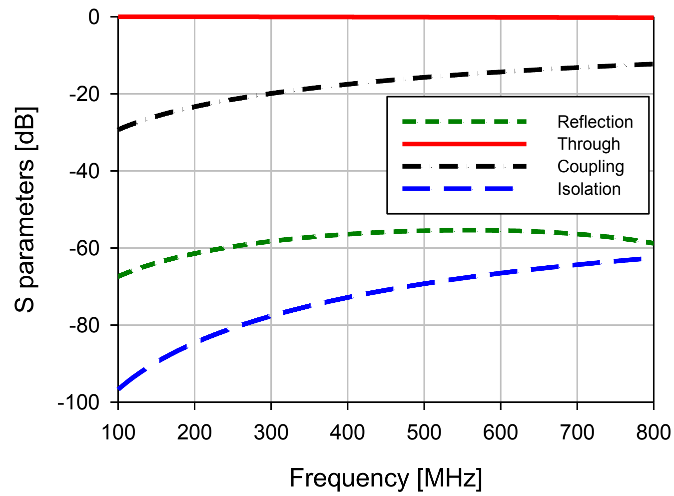

(b)

Figure 4.13: A three-section directional coupler for simulating the reflection at the input port of the antenna: (a) ADS model, and (b) Scattering parameters.

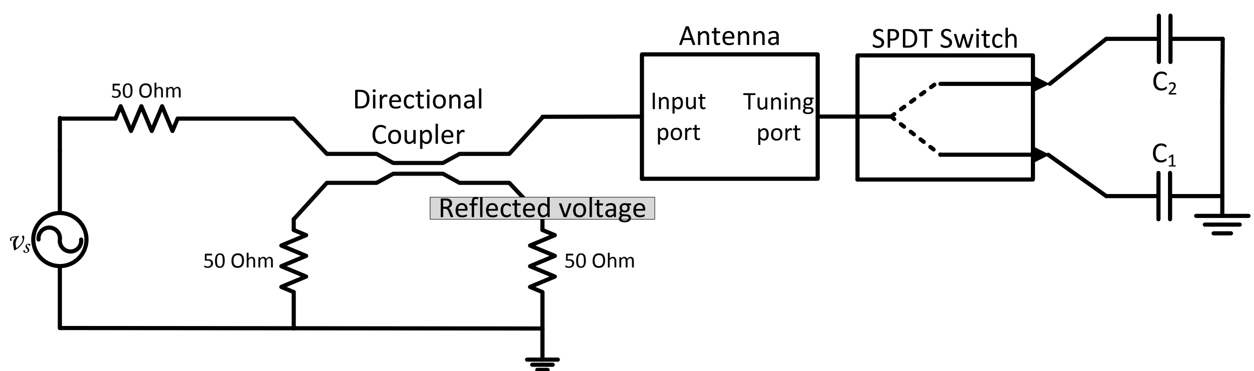

Figure 4.14: Simulation set-up for calculation of reflected voltage waveform.

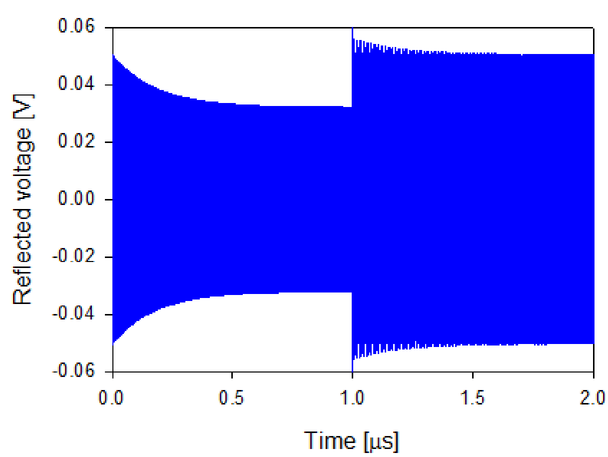

Figure 4.15: Simulated voltage waveform from t=0 to t=2 us at the isolation port. Switching occurs at t=1 us.

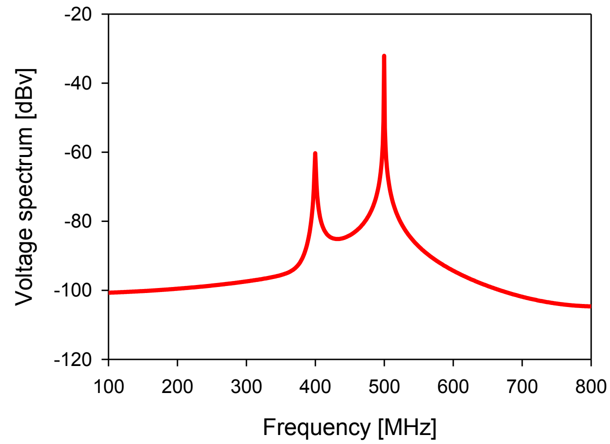

Figure 4.16: Frequency-domain of the reflected voltage calculated after the switching instant within the time window t=1 *us* to t=2 *us*.

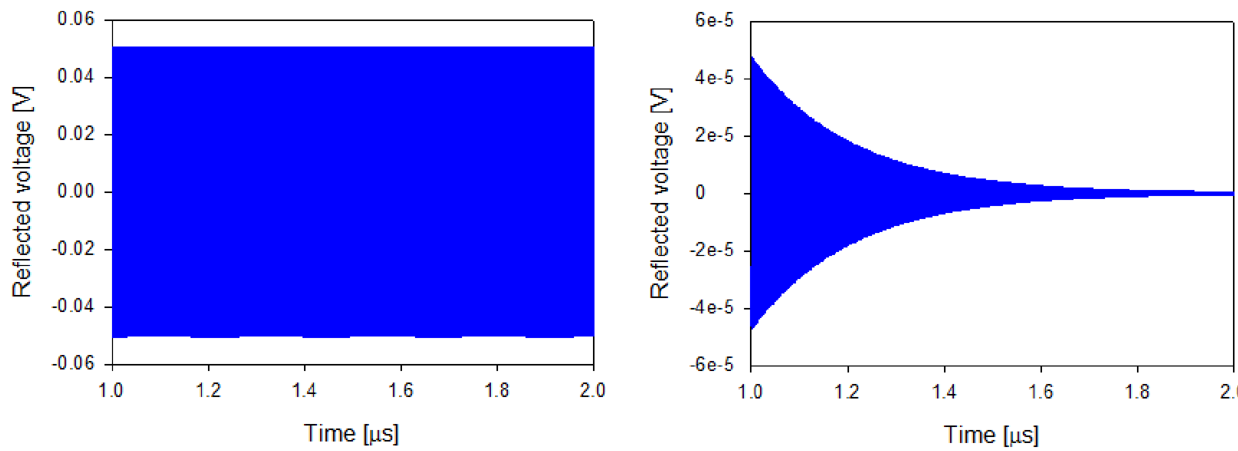

(a) (b)

Figure 4.17: Decomposition of time-domain reflection after the switching instant: (a) 500 MHz component and (b) 400 MHz component.

The amount of voltage reduction due to the series resistor at each resonant frequency is summarized in Table 4.2. It is obvious that loss has a substantial impact on the received voltage. This problem becomes a challenging showstopper as will be discussed in the experimental results.

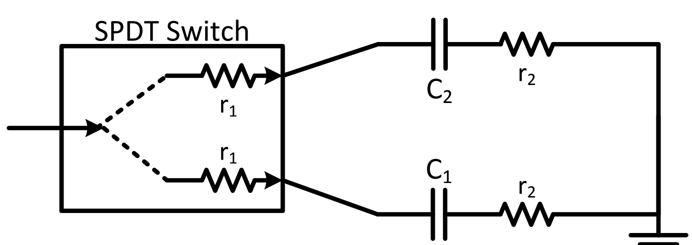

Figure 4.18: Simulation set-up for to study the loss effect.

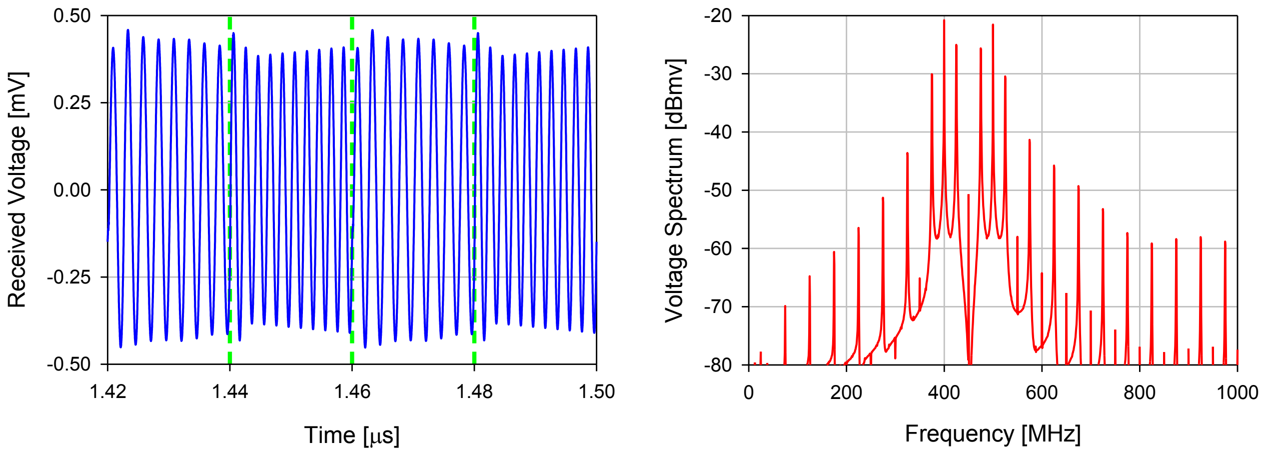
Received Voltage [mV]
0.50
0.25
0.00
-0.25
-0.50
1.42
1.44
1.46
1.48
1.50
Time [μs]
Voltage Spectrum [dBmv]
-20
-30
-40
-50
-60
-70
-80
0
200
400
600
800
1000
Frequency [MHz]

(a)

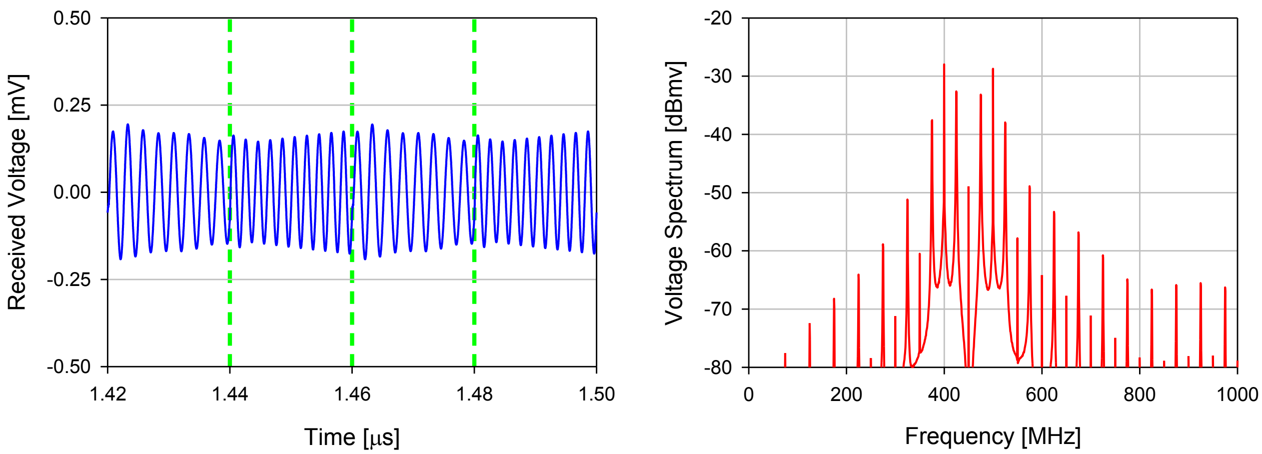
Received Voltage [mV]
0.50
0.25
0.00
-0.25
-0.50
1.42
1.44
1.46
1.48
1.50
Time [μs]
Voltage Spectrum [dBmv]
-20
-30
-40
-50
-60
-70
-80
0
200
400
600
800
1000
Frequency [MHz]

(b)

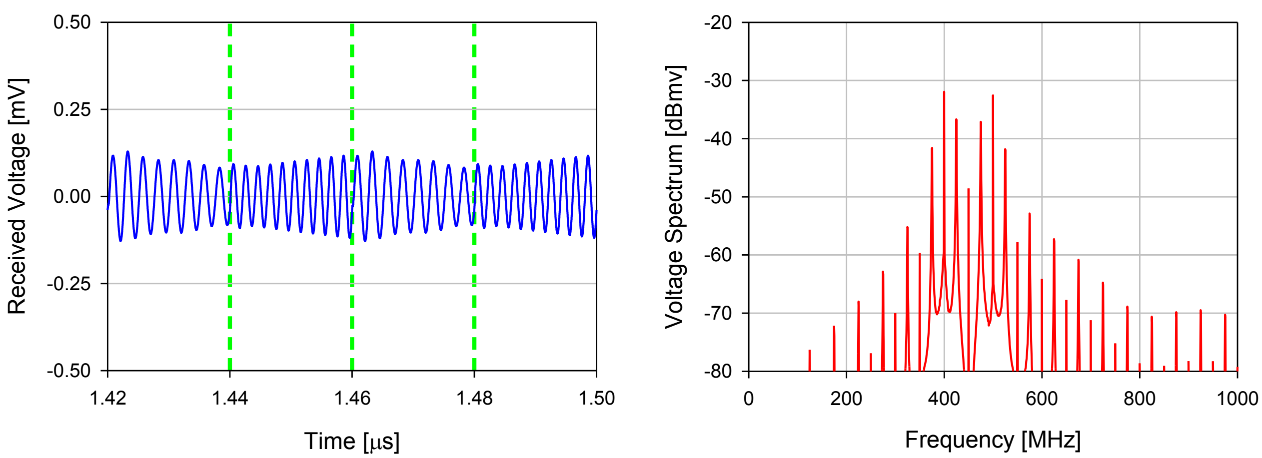
Received Voltage [mV]
0.50
0.25
0.00
-0.25
-0.50
1.42
1.44
1.46
1.48
1.50
Time [μs]
Voltage Spectrum [dBmv]
-20
-30
-40
-50
-60
-70
-80
0
200
400
600
800
1000
Frequency [MHz]

(c)

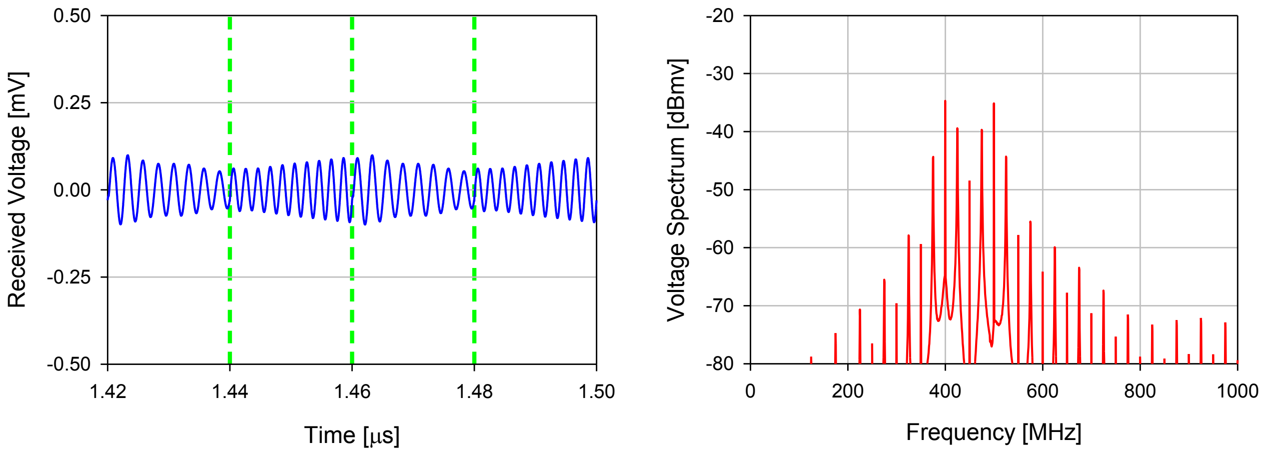

(d)

Figure 4.19: Time and frequency domain waveforms of the received voltage at the open-circuited input port of the measuring dipole for different *R* values at the switching frequency 25 MHz: (a) *R*=0 Ω, lossless case, (b) *R*=1 Ω, (c) *R*=2 Ω, and (d) *R*=3 Ω.

Table 4.2: Amount of voltage reduction due to the series resistor.

R (Ω)	0	1	2	3
Voltage level at 400 MHz (dB)	-20.8	-28.0	-31.9	-34.7
Voltage level at 500 MHz (dB)	-21.5	-28.7	-32.6	-35.1

4.7 Switched-Antenna with Tunable Resonant Frequency

One desirable characteristics of any transmitting system is the capability of tuning the carrier frequency on demand. Since the analysis of the proposed switched antenna is totally independent of the switched capacitor values, resonant frequency of the antenna can be tuned by using variable capacitors. However, it is important to arrange a mechanism for the switching frequency such that it can be automatically discretized and locked to the resonant frequencies such that the switching frequency always remains a common divisor of both resonant frequencies.

A straightforward technique to achieve a tunable resonance is using varactor diodes which are voltage-controlled capacitors. Technically, a proper choice of varactor diode for this purpose is the one that has minimum loss and enough tunability range regarding the available variation of

DC bias voltage. Figure 4.20 shows an example of tuning circuitry for tunable switched antenna. Two varactors independently control the resonant frequencies of the antenna through a variable biasing DC voltage. A low pass filter composed of L_B and C_B is used to prevent the RF leakage from the antenna to the DC source and capacitors C_{DC} provide the DC isolation for the antenna. The antenna is excited by a 500 MHz sinusoidal with magnitude 200 mV. The SPICE model of the varactors is extracted from SMV1247 varactor diode by Skyworks. The capacitance values versus reverse bias voltage based on factory data sheet is shown in Figure 4.21. Figure 4.22 shows the simulated time and frequency domain of the received voltage waveform for transmitting varactor-loaded switched ECLA using Agilent ADS. In the simulation, the first capacitance (C_1) is kept constant around 1.93 pF by applying a 1.19 V DC voltage to diode D_1 so that the 500 MHz resonant frequency does not change. The other switched capacitance varies by changing the DC voltage at diode D_2. The DC values used to tune the second resonant frequency are 0.35 V, 2.4 V and 10 V to make capacitance values approximately equal to 9 pF, 1.2 pF and 0.6 pF. Resonant frequencies associated with this arrangement are 350 MHz, 550 MHz and 600 MHz, respectively. The switching frequency for all cases is 25 MHz. As expected, the carrier frequencies of the FSK signal can be easily tuned to the required frequency.

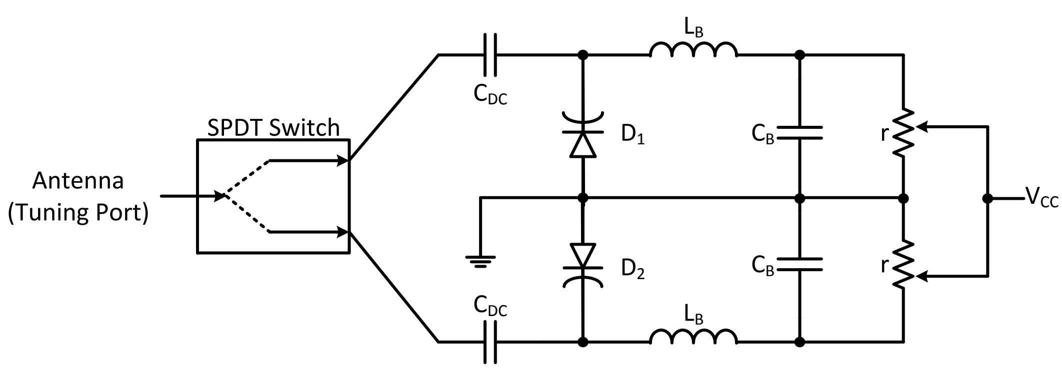

Figure 4.20: Tuning circuitry for tunable switched antenna.

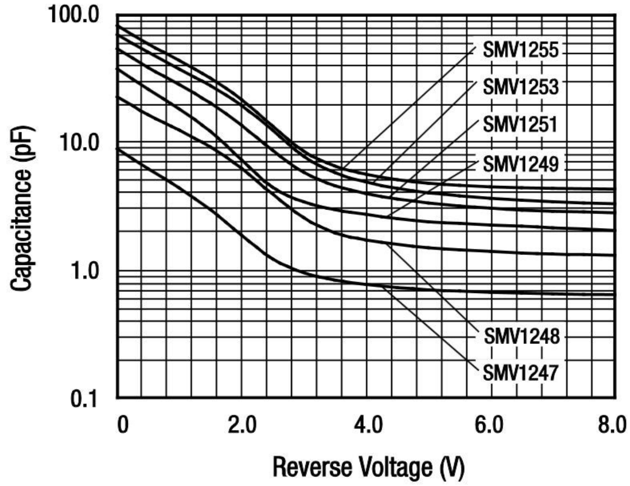

Figure 4.21: Capacitance values versus reverse bias voltage for SMV series varactor diodes, from Skyworks at:
http://www.skyworksinc.com/uploads/documents/SMV1247_SMV1255_Series_200061N.pdf

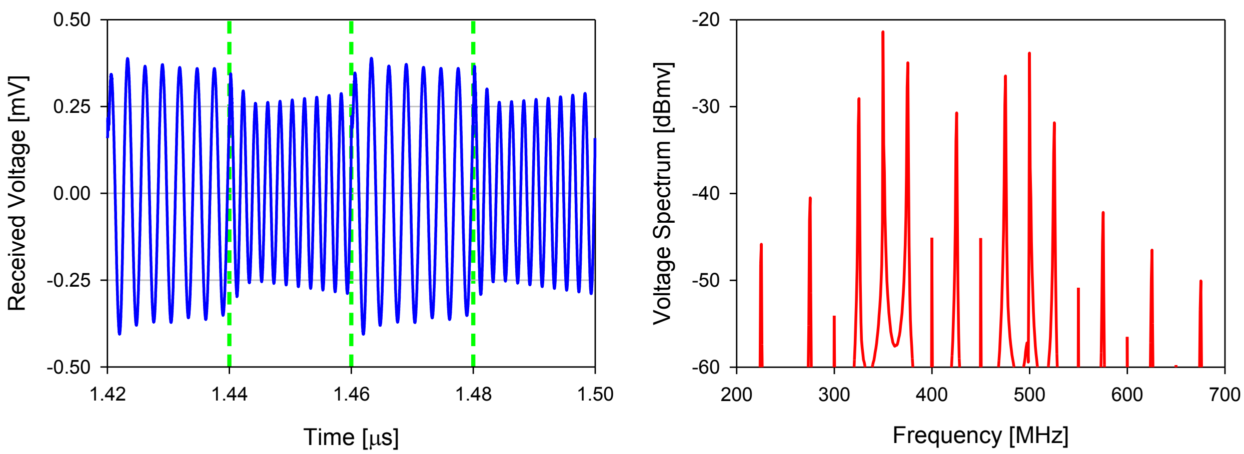

(a)

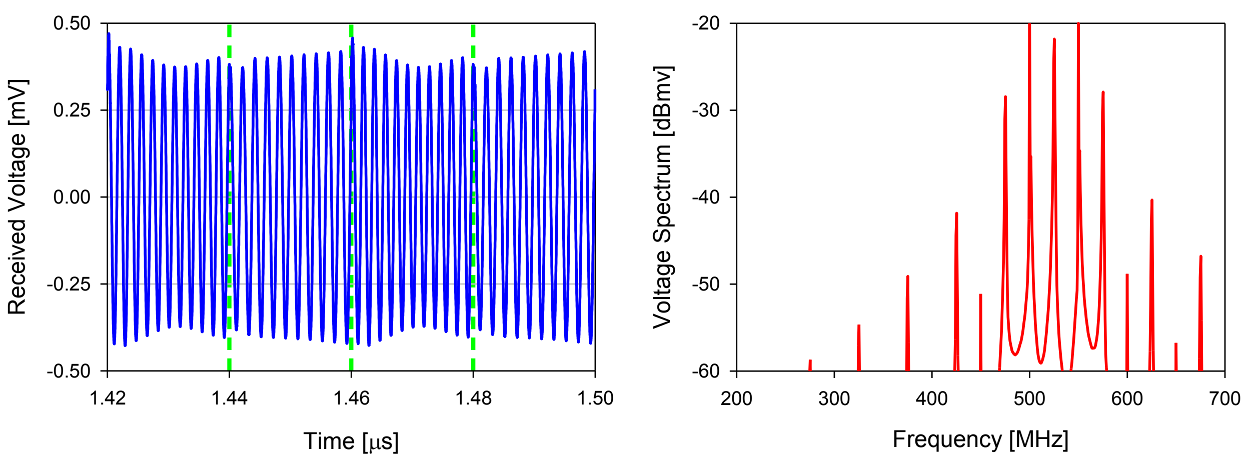

(b)

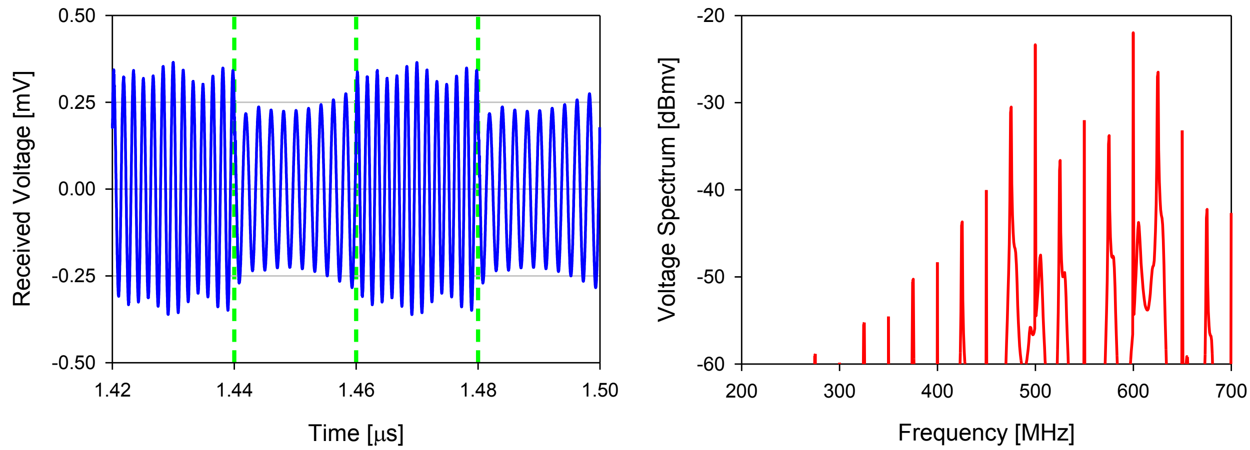

(c)

Figure 4.22: Simulation results for tunable switched antenna. The reverse bias voltage for D_1 is constant at 1.19 V and for D_2 is: (a) 0.35 V, (b) 2.4 V and (c) 10 V.

4.8 Chapter Summary

A new technique to realize a wideband data-transmission by using a narrowband antenna was presented. The proposed technique uses the transient property of a high-Q antenna to implement a binary FSK modulation with a high data-rate. It was shown that if the Q factor is sufficiently high such that the transient damping factor is small, the antenna can be switched between two resonant frequency and maintain a continuous radiation with minor power decay. The effect of lossy switching was also investigated and the capability of tuning the carrier frequencies by using variable switched capacitors was also explored.

Chapter 5

Switched Antennas II: Experiments

In Chapter 4 the theory of switched antennas was developed and simulation results were presented. It was shown that a high-Q small-size antenna can be employed in a time-varying fashion to realize a wideband transmission with high data-rate. One key point in the theory of switched antennas is maintaining a high radiation Q. In contrast with the conventional designs which in a low Q factor is desirable to increase the bandwidth, a switched antenna benefits from a high value of Q factor for two main reasons: first, in the cases that carrier frequencies have a small deviation it seems necessary for the antenna to have sufficiently high Q factor in order to prevent mixing the two frequencies. In fact, a high-Q switched antenna is able to transmit two independent frequencies when the modulating digital data change from 0 to 1 and vice versa. Second, the damping factor of the fields decreases as Q increases. This phenomenon is used to operate in the transient mode without a remarkable reduction in the radiated power. In the simulations, the switching mechanism assumed to be ideal without any loading effect. However in real life, there is no such an ideal switch. As a result, a low-loss switching mechanism should be used to demonstrate the validity of the switched antenna technique proposed in previous chapter. In this Chapter, challenges and solutions for such an experiment are discussed and the measured results for both Tx and Rx modes are presented.

5.1 RF Switch ICs

To validate the proposed technique, a switched electrically-coupled loop antenna (ECLA) is prototyped and measured. The experiments are performed at a low frequency in order to implement a high-*Q* radiation and achieve a good isolation between the two alternating frequencies. In addition, realizing an ultra-fast and high-*Q* switching mechanism is a challenge as most of the commercial RF switches suffer from a relatively high insertion loss and low speed. Nevertheless, ultra-fast switching can be addressed by recently developed technologies such as SiGe transistors [150]. It is also important to implement a very low-loss switching mechanism in order to maintain a high-*Q* radiation. To configure the required switching mechanism, three off-the-shelf RF switches have been used:

a) NJG1512V (JRC): GaAs single pole-double throw (SPDT) switch with nominal 8 ns switching speed and 0.6 ~ 1 dB insertion losses.
b) AS211-334 (Skyworks): pHEMT single pole-double throw (SPDT) with nominal 20 ns switching speed and 0.3 ~ 0.5 dB insertion loss.
c) ADG918 (Analog Devices): CMOS single pole-double throw (SPDT) with nominal 10 ns switching speed and 0.4 ~ 0.7 dB insertion loss with on-board CMOS control logic.

Figure 5.1 shows the switched antenna prototypes using each of these switches along with control logic circuitry and the pin configuration. All the switching circuits were used to make a switched ECLA. However, all switches have failed to maintain the required *Q* factor due to their insertion loss. Figure 5.2 displays the return loss of the ECLA design shown in Figure 5.1(c) when ADG918 is used to switch the antenna. By turning the switch ON and OFF, the resonant frequency switches between 192 and 237 MHz. A capacitance of 1.6 pF adds to the input RF port when the switch is ON. Also, the input capacitance of control pin is equal to 2 pF. Although the antenna won’t be impedance-matched after connecting the switch due to the input capacitance of the switch, the switch dramatically loads the antenna and reduces the measured *Q* factor from 22 to about 7.

Moreover, the switch loss increases with the switching frequency results in a very low *Q* when the antenna is switched at a high rate. In order to investigate the amount of loss caused by the switching circuitry, the input impedance of ADG918 switch has been measured.

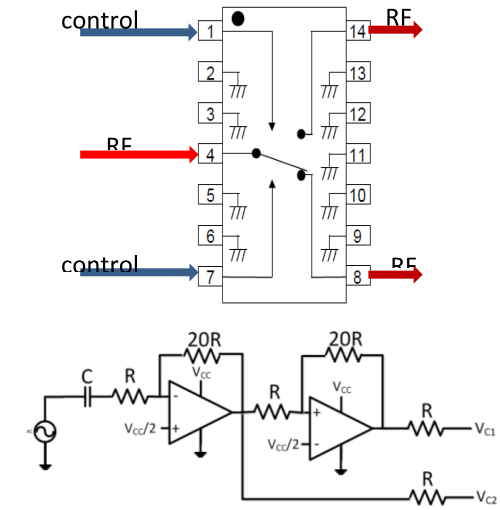

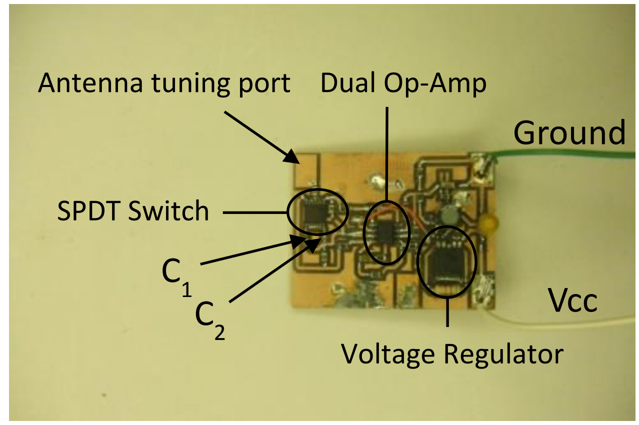

(a)

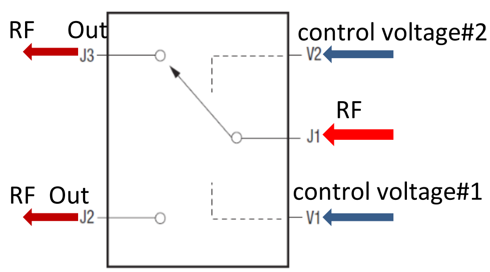

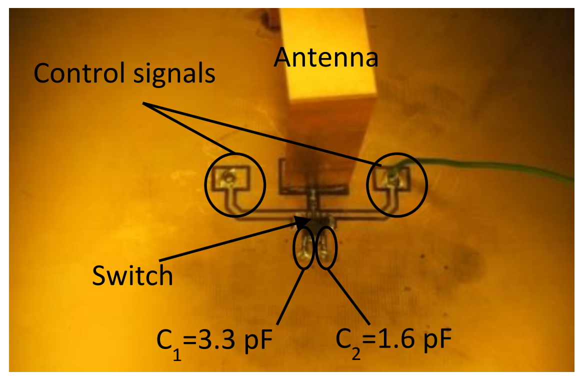

(b)

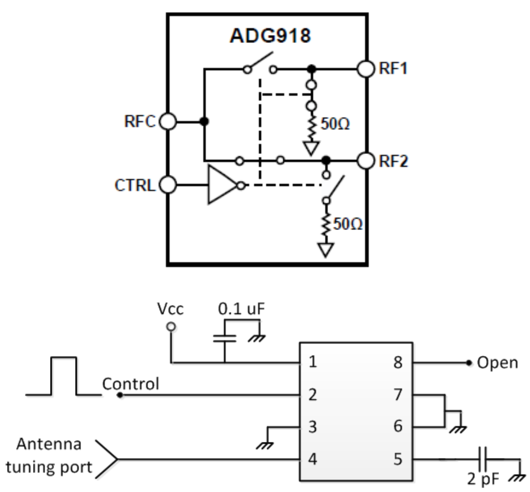

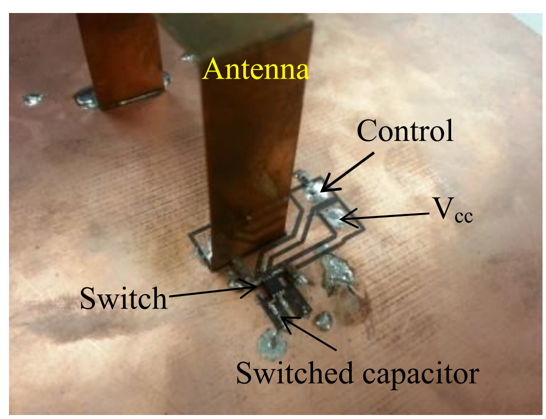

(c)

Figure 5.1: Switched antenna prototypes and switching circuitry using different switches: (a) NJG1512V (JRC), (b) AS211-334 (Skyworks), and (c) ADG918 (Analog Devices).

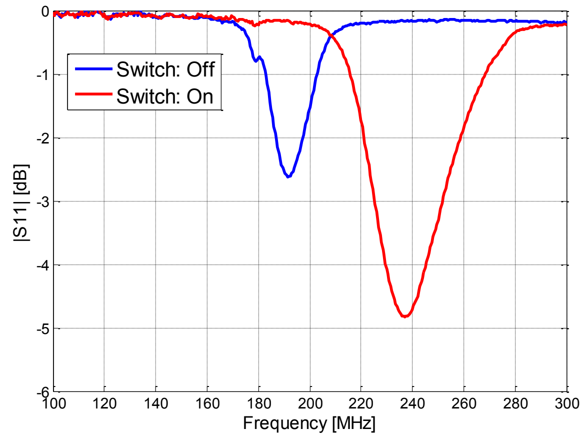

Figure 5.2: Measured return loss of the ECLA design shown in Figure 4.7(b) when ADG918 is used to switch the antenna.

Figure 5.3 shows the measurement set-up including a calibration arrangement on an FR4 board with and without the presence of switching circuit. The measured results shown in Figure 5.4 clarify why switch ICs would not be excellent choices to implement a high-*Q* switching mechanism. The input impedance of the switch is summarized in Table 5.1 for ON and OFF states as well as different switching frequencies measured at the RF frequency 265 MHz. At higher switching frequencies, input resistance of the switch increases substantially and makes the switch an unsuitable choice for realizing a high-*Q* radiation.

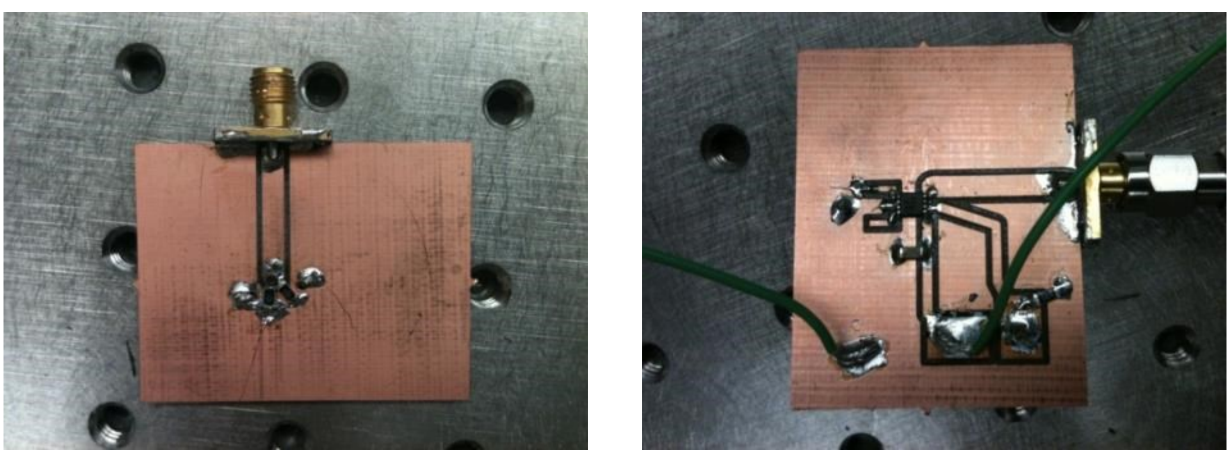

(a) (b)

Figure 5.3: Evaluating the switch loss: (a) calibration set-up and (b) measurement set-up.

Table 5.1: Input impedance of ADG918 (SPDT switch) at 265 MHz

	Input Resistance (Ohm)	Input Capacitance (pF)
ON-State	37	1.7
OFF-State	13	3.8
f_s=1 MHz	33	2.8
f_s=10 MHz	80	3.5
f_s=20 MHz	101	4.9
f_s=30 MHz	96	7.2

5.2 PIN Diode Switch

A PIN diode typically operates as a variable resistor at radio and microwave frequencies. In contrast with varactor diodes which are voltage-controlled capacitors, a PIN diode is controlled by the bias current. PIN diodes exhibit a small capacitor in reverse bias that blocks the RF signal. In forward bias, a PIN diode shows a very small resistor allowing the RF signal to pass through with a very low insertion loss. If the control current is switched ON and OFF, the PIN diode can be used for switching purposes. Due to the high speed, low package parasitic elements and low forward-bias resistance, PIN diodes are excellent choices to realize extremely low insertion-loss RF switches [151]. Since realizing a single pole-single throw switch (SPST) requires fewer components and hence, less loading effect on the antenna, we use a single switched capacitor in our experiment to tune the antenna to a desired resonant frequency. The second frequency is achieved by letting the antenna radiate at its own resonant frequency by opening the switch. Figure 5.5 shows series and shunt PIN diode circuits as the two common SPST switch configurations [152]. Since the shunt arrangement shows a better performance in terms of loss, we would carry out the measurements by a shunt switch. In our experiment, we use a low-loss PIN diode (Avago HSMP-482) in a shunt arrangement as depicted in Figure 5.6 which shows the switching schematic for the switched ECLA. Figure 5.7 displays the prototyped switching circuitry. The switching signal is separated from the antenna by a low pass filter (L_{lpf} and C_{lpf}). When the PIN diode is in reverse bias (switch-OFF), the tuning port is open-circuited and the antenna is not loaded. Therefore the antenna resonates at its original resonant frequency, f_1. In the forward-bias state (switch-ON), the antenna is loaded by the capacitor C_t through a 0.6 Ω resistance of the forward-biased PIN diode and resonates at the lower frequency, f_2.

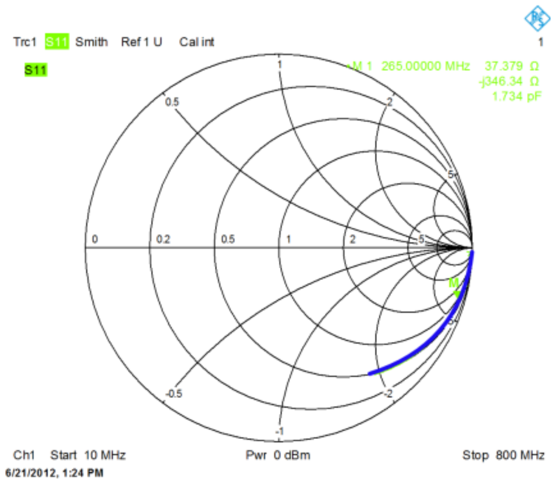

(a)

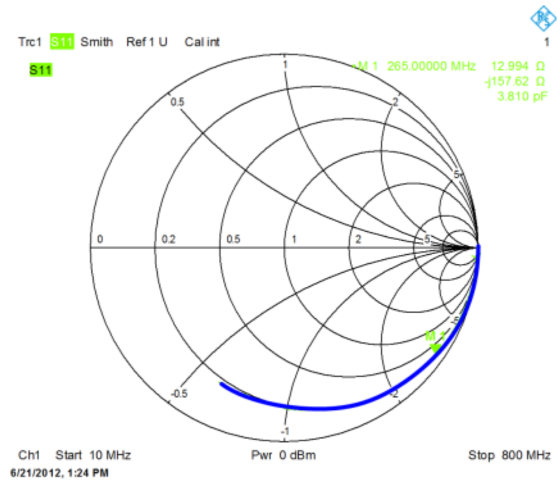

(b)

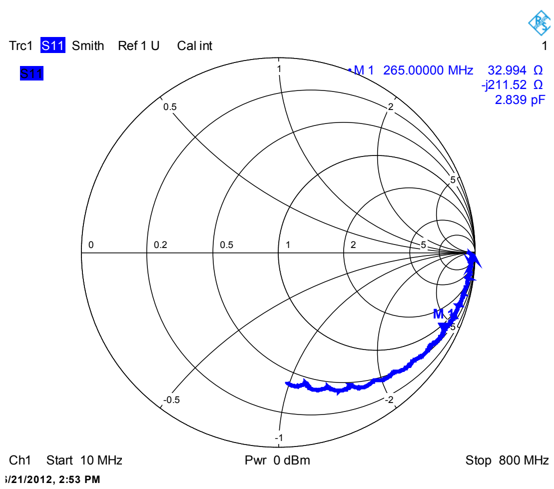

(c)

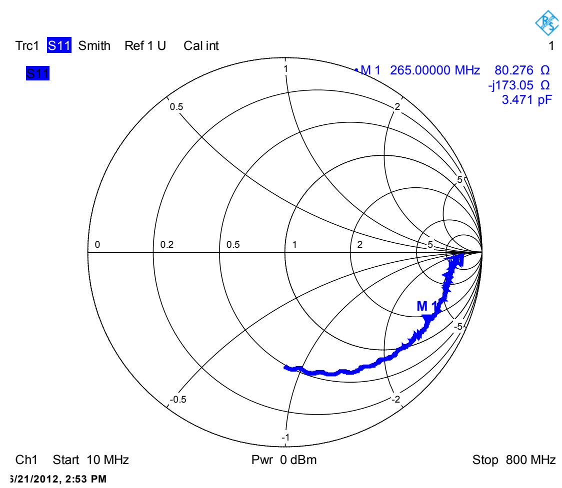

(d)

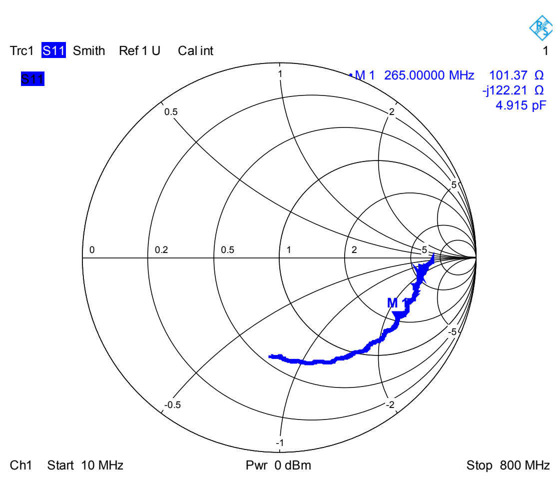

(e)

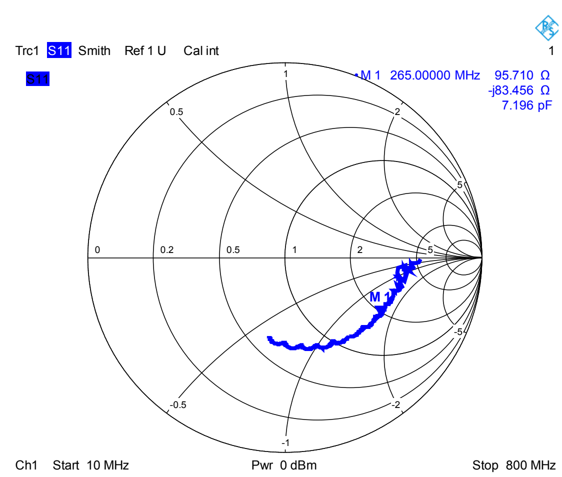

(f)

Figure 5.4: Measured input impedance of the switch ADG918 at (a) ON-state, (b) OFF-state, (c) f_s=1 MHz, (d) f_s=10 MHz, (e) f_s=20 MHz, and (f) f_s=30 MHz.

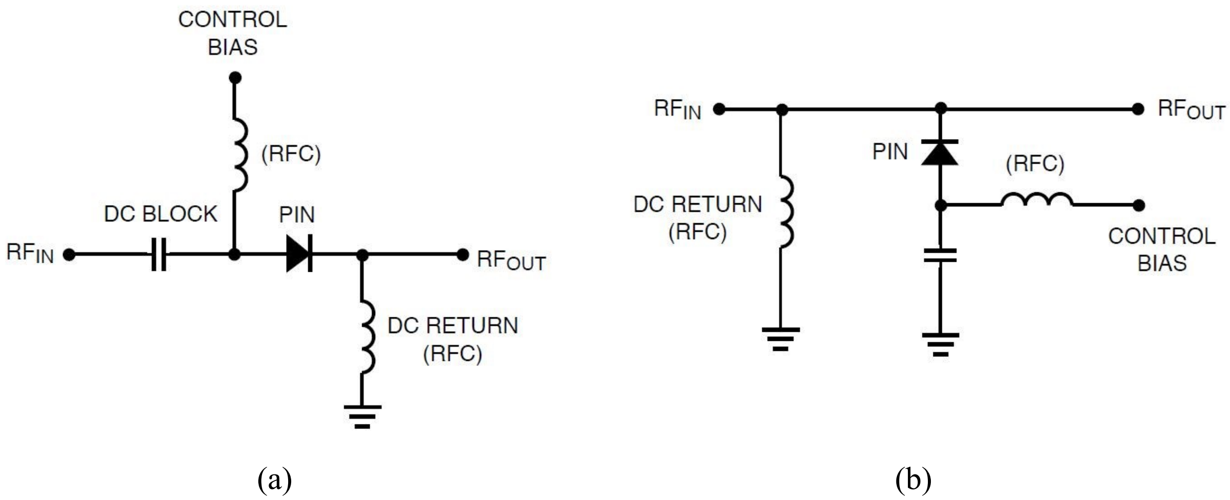

Figure 5.5: Two common SPST PIN diode switch configurations: (a) series and (b) shunt switch.

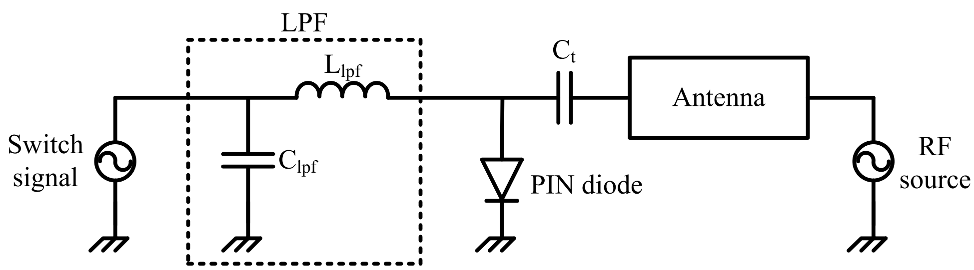

Figure 5.6: Switching schematic used in the experiments.

Figure 5.7: Prototyped switching circuitry.

5.3 Switched ECLA Prototype

The prototyped antenna is shown in Figure 5.8 with dimensions: L=100 mm, W=30 mm, w_f = 25 mm, h_c =0.51 mm, w_c = 30 mm and h_f =2.5 mm. The bottom side of the antenna that includes the switch circuitry is supported by a 20 mil Rogers RT/duroid 5880.

(a)

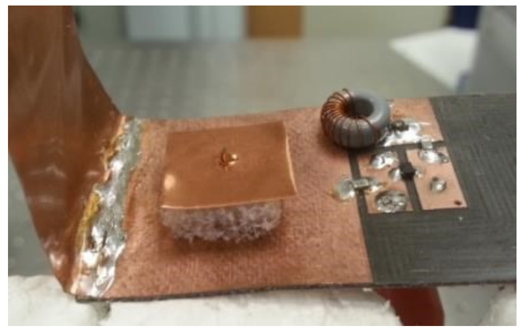

(b)

Figure 5.8: (a) Prototyped antenna with dimensions: L=100 mm, W=30 mm, w_f = 25 mm, h_c =0.51 mm, w_c = 30 mm and h_f =2.5 mm, (b) switching circuitry attached to the antenna on a RT/Duroid 5880 with thickness 20 mil.

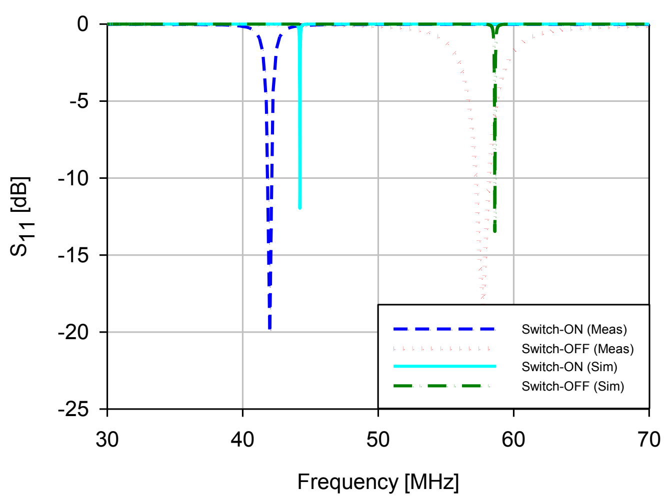

Figure 5.9: Measured and simulated return loss of the prototyped ECLA.

Although the capacitors and PIN diode are chip components, however due to the relatively low-Q properties, particularly for the capacitors, measurement shows that the loaded Q is considerably affected. Figure 5.9 compares the measured return loss with the results of full-wave simulation that uses an ideal capacitor. The measured resonant frequencies are f_1 =57.75 MHz and f_2 =42 MHz where the tuning capacitor is C_t =47 pF. Low pass filter with C_{lpf} =470 pF and L_{lpf} =1 uH provides an insertion loss equal to 30 dB and 25 dB at frequencies f_1 and f_2, respectively. Measured Q factors at f_1 and f_2 are Q_1 =18.6 and Q_2 =52.5 and the measured leakage from f_1 to f_2 and vice versa is less than 0.04 dB. Since the Q factors are still much greater than one and two resonant frequencies are well-isolated from each other, this configuration can be used to validate the proposed technique. The maximum practical bit-rate in our experiment depends on the switching speed which is determined by the PIN diode rise and fall time. Figure 5.10(a) shows the measured response of the PIN diode to a rectangular pulse function varying between ±2 V. The ON and OFF time based on 0 to 0.65 V and vice versa is measured about 65 ns. This limits the switching speed to about 15 MHz. Also, the PIN diode exhibits an overshoot about 1.5 times the biasing voltage at the falling edge causing the OFF time to be shortened. The switch signal measured as the anode voltage at frequency 2 MHz is shown in Figure 5.10(b). Even though the duty cycle of the pulse is %50 the switch-ON duration associated with the lower frequency, f_2, is approximately twice the switch-OFF duration that represents the higher frequency, f_1.

5.4 Transmitting Mode

A small dipole is used to capture the radiated fields from ECLA as displayed in Figure 5.11. Figure 5.12 shows the voltage waveform at the receiving dipole when the switched ECLA is in transmitting mode. The RF source is an R&S ZVA50 vector network analyzer in the CW mode which excites the antenna at the frequency f_2 =42 MHz. A Tektronix AFG3252 signal generator is used to provide a periodic pulse as the switching signal. Time-domain electric fields are measured by a Tektronix MSO4102 oscilloscope with 1 MΩ input impedance. The electric fields shown in Figure 5.12 are measured at switching frequencies 2 MHz, 4 MHz, 8 MHz and 12 MHz. It can be seen that even though the antenna bandwidth is measured about 3 MHz at the upper band, an FSK modulation with a bit-rate equal to R=2×12=24 Mb/s is realized. The restriction on the switching frequency is due to the time constant of the low-pass filter and also the ON and OFF time of the PIN diode. Hence, the bit-rate can be further improved by using a faster switch and improving the filter performance.

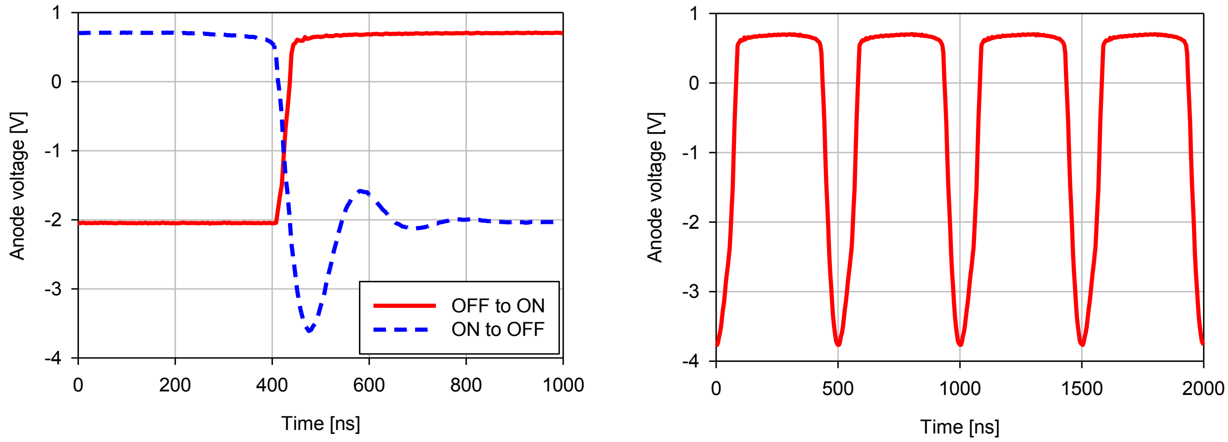

(a) (b)

Figure 5.10: Measured voltage waveform across the PIN diode: (a) comparison between ON and OFF times and (b) switch signal is a 2 MHz periodic pulse varying between ±2 V with %50 duty-cycle.

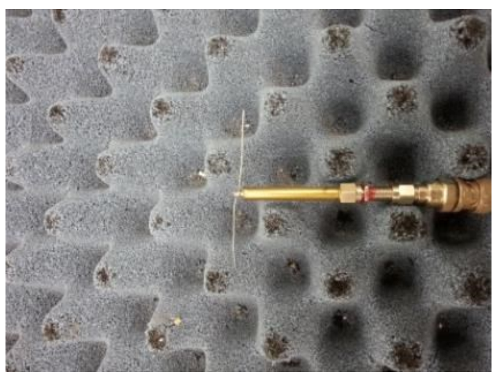

Figure 5.11: Measuring dipole.

5.5 Receiving Mode

For demonstration purposes, the antenna has also been measured in the receiving mode. Figure 5.13 shows the measurement set-up. An HP8648D function generator and an HP8625A synthesized RF sweeper are connected via a power combiner to provide a dual-tone excitation for a small dipole which is used as the transmitting antenna. Since the received power by the ECLA is different at each frequency due to different impedance matching, the transmitted power is tuned at each RF source such that the ECLA receives both frequencies at the same power level. Source 1 feeds the dipole at 58 MHz and power level 13 dBm and Source 2 is set to 42 MHz at power level 20 dBm. Figure 5.14 shows the frequency spectrum of the received voltage at the input port of the ECLA when connected to a 1 MΩ oscilloscope. Figure 21(a) depicts the switch-OFF state where the ECLA receives the higher frequency (58 MHz) signal and the switch-ON state is shown in Figure 21(b) where lower frequency (42 MHz) is received. At each state, the out-of-tune frequency component is about 29 dB below the level of tuned frequency. However, both frequencies are evenly received by the ECLA at the level -41 dB. Figure 5.14 shows the received signals when both frequencies are on the air and the antenna is switched at frequencies 1 MHz, 5 MHz and 10 MHz. Similar to the transmitting mode, the switched antenna receives both frequencies according to the switching frequency.

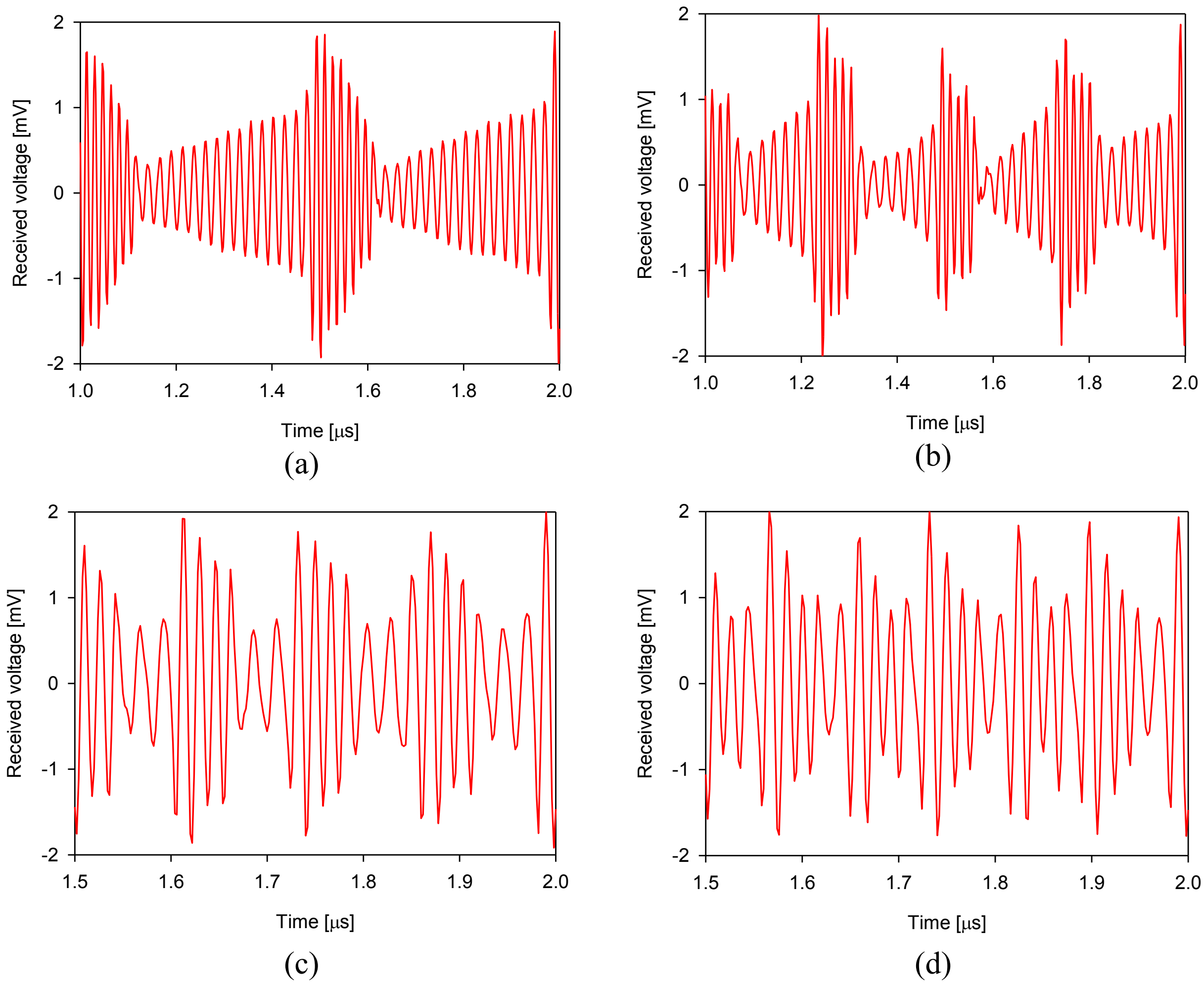

Figure 5.12: Measured voltage waveform received by a small dipole for different switching frequencies: (a) f_s=2 MHz, (b) f_s=4 MHz, (c) f_s=8 MHz, and (d) f_s=12 MHz.

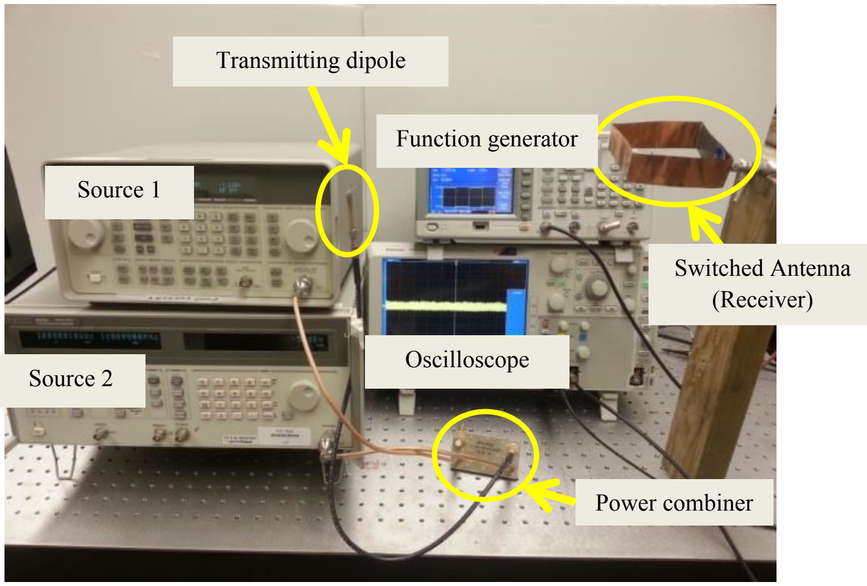

Figure 5.13: Measurement set-up for receiving mode.

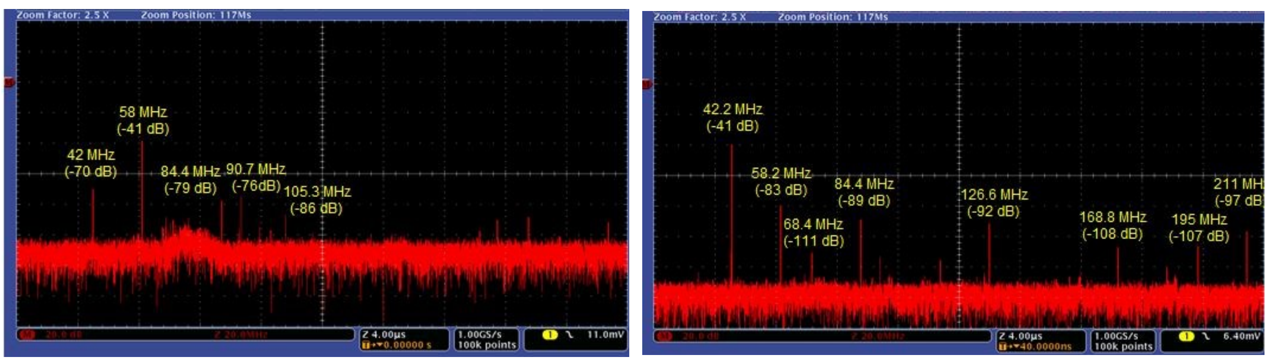

Figure 5.14: Frequency spectrum of the received voltage at the input port of the ECLA when connected to a 1 MΩ oscilloscope: (a) switch-OFF state and (b) switch-ON state.

It is necessary to mention that when the switching frequency increases, the radiation is fully in transient mode. It means that the received voltage by the antenna in Rx mode or radiated fields in Tx mode are due to the transient response of the antenna caused by the momentary current distribution right after the switching moment, when the location of fundamental pole of the antenna changes. To study this phenomenon more closely, one of the source frequencies is turned off when the antenna operates in Rx mode and the received voltage is measured. Figure 5.16 shows the open-circuit terminal voltage at the receiving ECLA when the higher frequency source (58 MHz) is turned off and only 42 MHz signal is on the air. The switching frequency is chosen to be very small in order to have long intervals between two consequent switching states and hence, the transient response at each state is fully observable. Figure 5.16(a) shows the switch-OFF moment when the resonant frequency of the antenna shifts to the 58 MHz which is not supported by the RF source. It can be seen that an exponentially-decaying voltage waveform can be measured at 58 MHz. The damping factor of this transient response is inversely related to the *Q* factor of the antenna at 58 MHz, as discussed in Chapter 2. In Figure 5.16(b) the switch-ON moment is shown when the resonant frequency of the antenna changes from 58 MHz to 42 MHz. The voltage waveform for this case is composed of the transient response and the steady state whose magnitude is dictated by the received power level. A similar phenomenon occurs when the lower frequency source (42 MHz) is turned off and the 58 MHz signal is on the air. Receiving voltage for this case is shown in Figure 5.17.

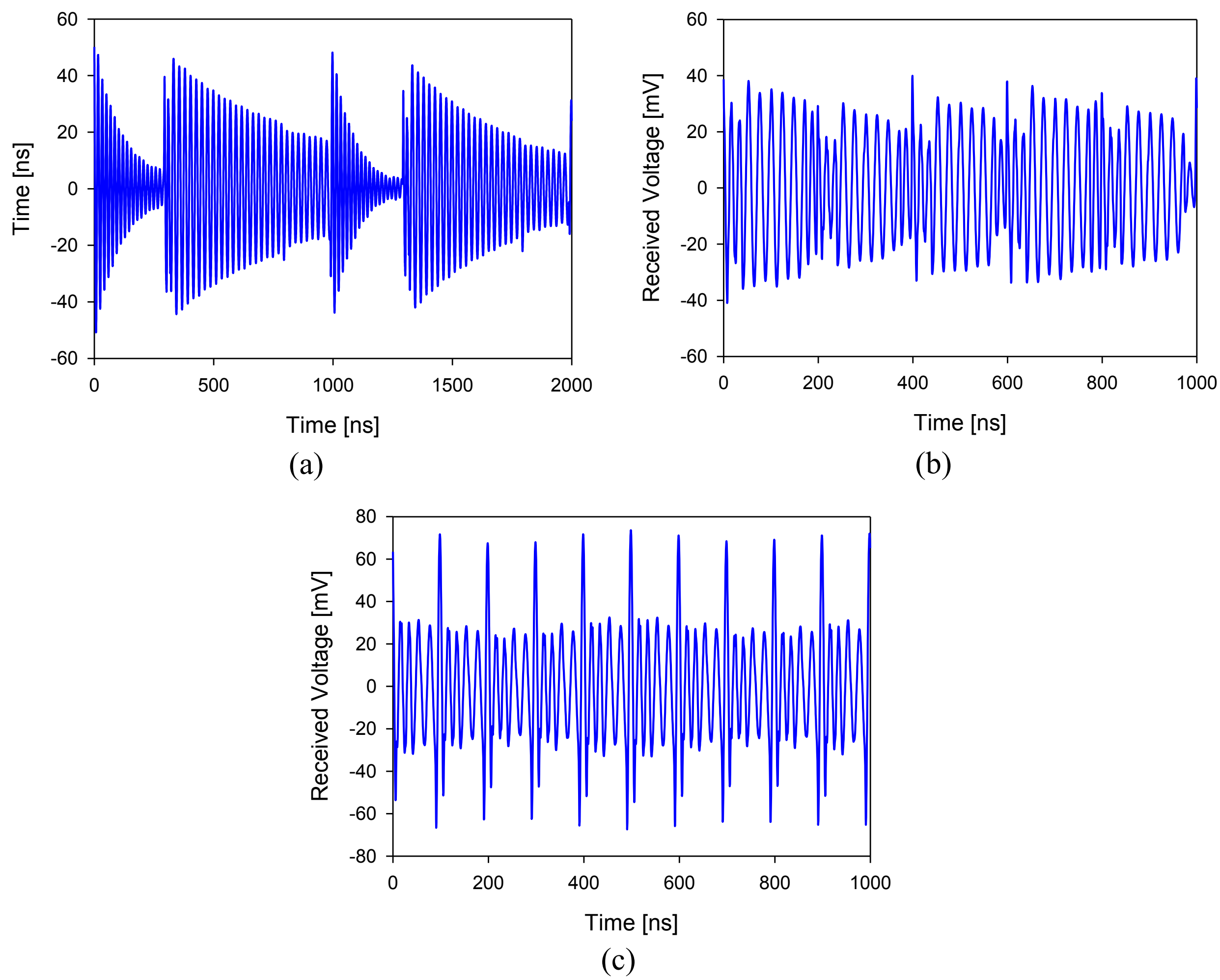

Figure 5.15: Measured voltage waveform received by the ECLA when operating in Rx mode at different switching frequencies: (a) f_s=1 MHz (b) f_s=5 MHz, and (c) f_s=10 MHz.

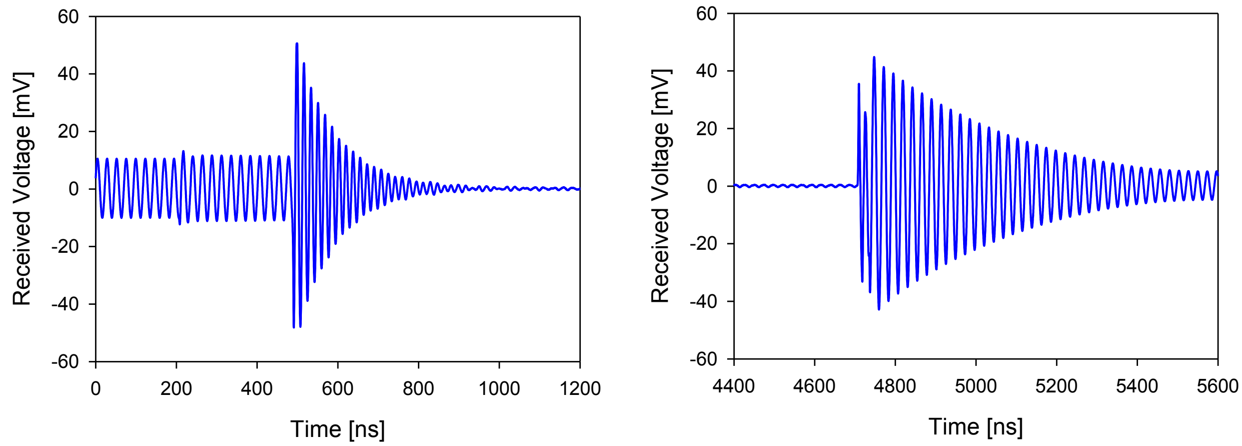

(a) (b)

Figure 5.16: Measured voltage waveform received by the ECLA when the higher frequency source (58 MHz) is turned off and only the 42 MHz signal is on the air. Antenna is switched at 100 KHz: (a) switch-OFF instant and (b) switch OFF instant.

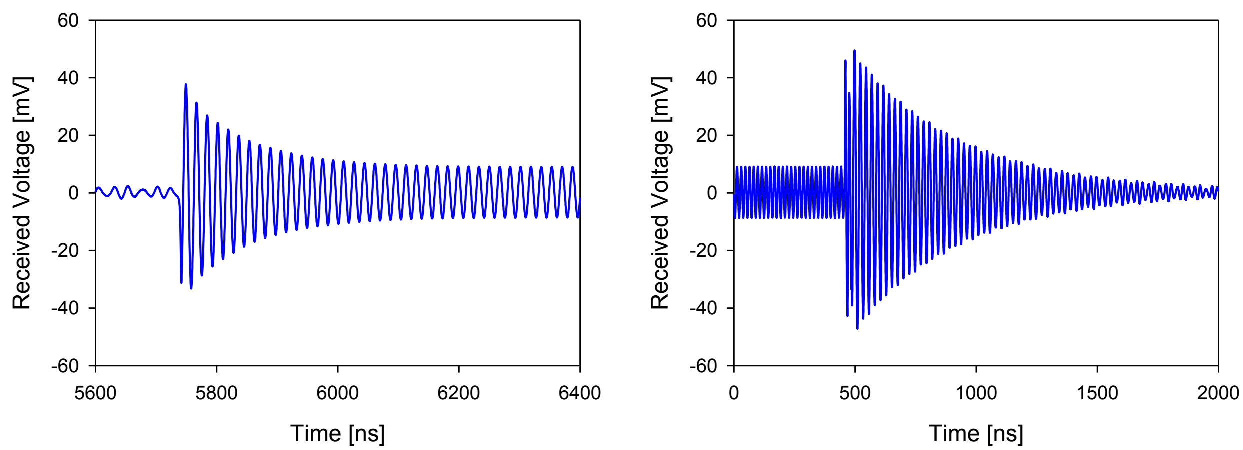

(a) (b)

Figure 5.17: Measured voltage waveform received by the ECLA when the lower frequency source (42 MHz) is turned off and only the 58 MHz signal is on the air. Antenna is switched at 100 KHz: (a) switch-OFF instant and (b) switch OFF instant.

The measurement results indicates that if a single transmitting frequency is on the air, the other frequency component can be generated by switching the resonant frequency of the antenna. It suggests that if the switching rate is high enough such that the antenna operates in transient mode at both frequencies, one of the sources can be removed and only a single source is sufficient to receive a signal which alternatively shifts between two frequencies. This can be seen in Figure 5.18 that shows the measured terminal voltage of the ECLA when switched at 5 MHz.

Figure 5.18(a) shows the case that higher frequency source (58 MHz) is removed and Figure 5.18(b) is the received voltage waveform when the lower frequency (42 MHz) is turned off. It is interesting to notice that these waveforms are similar to Figure 5.15(b) where both frequencies are on the air. Since each frequency component requires an initial current distribution to be transmitted or received in the transient mode, further simplification can be carried out to minimize the architecture of the antenna as a self-contained frequency modulation transmitter. In the next chapter a new technique to remove both sources will be introduced and it will be demonstrated that basically a transient mode radiation doesn't require to be supported by an RF source and an impulse excitation is sufficient to transmit an FSK signal by a switched antenna.

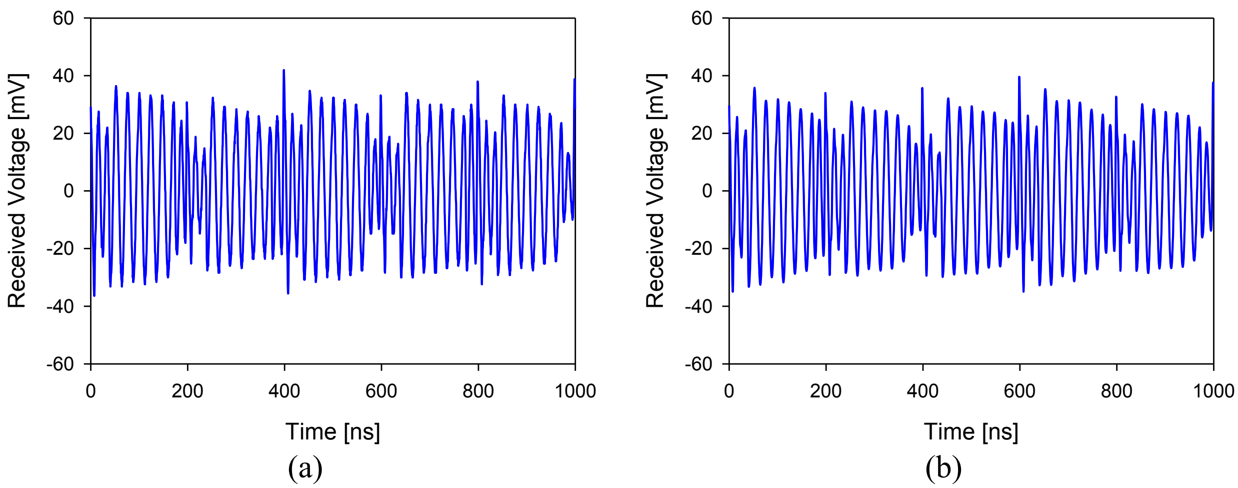

Figure 5.18: Measured voltage waveform received by the ECLA at switching frequency 5 MHz when (a) 58 MHz source is removed and (b) 42 MHz source is removed.

5.6 Chapter Summary

This chapter discusses the efforts toward the validation of frequency modulation technique proposed in Chapter 4. The impact of lossy switch ICs on the performance of the antenna was studied and a PIN diode switching circuitry with a low loss level was introduced as a suitable approach to carry out the experiments. The ECLA was prototyped and measured in both Tx and Rx mode and it was verified that a high-*Q* antenna can be used to transmit a high-rate data beyond the conventional limits of FSK modulation. Although the switching speed was limited to 12 MHz (24 Mb/s) due to technical limitations, a higher data-rate can be achieved by using a faster switching mechanism with minimized insertion loss.

Chapter 6

Self-Contained Transmitter with Direct Excitation

In previous chapter it was shown that a single-mode small antenna can operate in transient state if there is an initial current distribution on the antenna. This property was used to employ a single RF source in order to achieve a frequency-shift keying modulation where a carrier frequency was supported by the source and the second frequency was generated through the switching procedure. This phenomenon brainstorms the idea of implementing a transmitter with no RF oscillators. Basically, if the antenna radiates only transient EM waves, an impulsive excitation may be sufficient to generate the required frequencies. As a matter of fact, the idea of impulsive transmitters has been established years ago as “spark-gap transmitters”. Spark-gap transmitters were composed of LC resonators with a narrow gap in between where an instantaneous high voltage was applied to send a single pulse. This chapter focuses on the idea of realizing a self-contained transmitter which is fed by only a DC power source and results in a high-rate FSK modulation produced by the switching mechanism. A switched capacitor is used not only to tune the resonant frequency, but also as an intermediate component to transfer the energy from the DC source to the antenna.

6.1 Introduction

Spark-gap transmitters are known as the oldest transmitters made by man in 1880's. The structure of a spark-gap transmitter is as simple as an inductor and capacitor in series with an air gap. When a spark takes place across a narrow gap by applying a momentarily high voltage that for example can be achieved by discharging a capacitor, the spark energy will be released in the form of heat and electromagnetic radiation. An example of early spark-gap radio from 1917 is shown in Figure 6.1 [153].

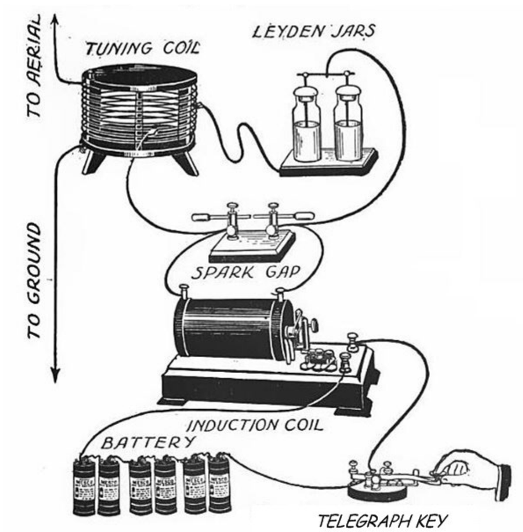

(a)

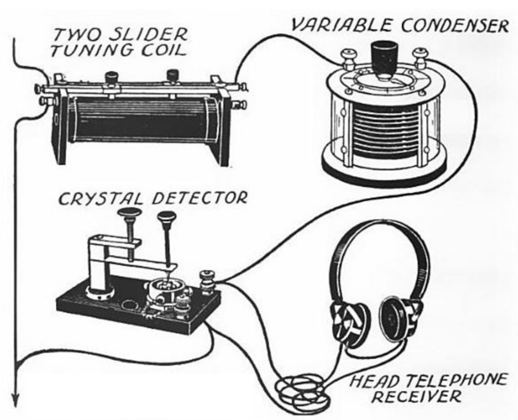

(b)

Figure 6.1: Schematic of early spark-gap radios: (a) transmitter and (b) receiver.

In 1857, Berend W. Feddersen realized that an electric spark is composed of damped oscillations. He managed to experience this phenomenon by using magnetic coils and a Leyden jar (early capacitors) and wrote an article "On the Electric Discharge of the Leyden Jar" where he demonstrated that oscillating currents can be produced by discharging an electrical condenser into a metal [154]. Later in 1868, James C. Maxwell assumed that the energy during the condenser discharge is partly dissipated as heat and partly conserved as current energy in the circuit. He solved the describing 1st order differential equation for an RLC circuit excited by an impressed current and showed that a maximum in the response occurs when $\omega L=1/(\omega C)$ [155]. David Hughes in 1879 accidentally realized that due to a loose wire in his induction balance, a spark is generated which results in hearing a burst of noise in his earphone [156]. He made a primitive transmitter by interrupting the coil current and hearing the noise burst within the range of several rooms, but never published his discoveries. Several years later in 1887, Heinrich Hertz made his first spark-gap transmitter and successfully tested it [157]. A year later in 1888, he verified the radiation caused by a spark gap by calculating the electromagnetic fields due to an rectilinear current element as predicted by Maxwell [158]. In 1893, Nikola Tesla introduced a spark-gap transmitter with capability of tuning the receiving coil in order to achieve a higher efficiency [159]. In late 1890's, Guglielmo Marconi was inspired by Hertz's and Tesla's findings and demonstrated a series of his radio systems. In 1901, he developed a practical wireless telegraphy using high-powered spark-gap transmitter and managed to transmit and receive radio signals across the Atlantic [160]. Although the use of spark-gap transmitter was a technological breakthrough at the time, due to their interference with other radio signals, spark-gap transmitters were restricted after the invention of vacuum tube technology. In recent decades, spark-gap feeding is used in several applications such as transient radars and high-power ultra wideband systems [161, 162]. In these applications, various techniques such as gas or oil switching are employed to generate high-power short pulses.

6.2 Theory of Self-Contained Transmitter

Here we use the concept behind the spark-gap transmitters in a different fashion in order to realize a wideband transmission through a small antenna. We employ the switched capacitor for two purposes: first, transferring the energy from the DC power source to the antenna and second, changing the resonant frequency of the antenna. With this configuration, we can build a self-contained transmitter by using the antenna in transient mode. While the radiation power is obtained from a DC source, an RF oscillator is no longer needed. On the other hand, the switching mechanism is used to move between two resonant frequencies and realize an FSK modulator and hence, a modulating component such as a VCO is not required either. Since the switch is controlled by a sequence of digital signals, the transmitter can operate by only the baseband data.

Either early transmitters or recent high-power UWB systems use the stored energy inside a capacitor to energize the antenna and send a pulse. At each spark, the stored energy which is provided by a DC power supply converts to a radiating energy in the form of damped resonating electromagnetic fields. In other word, a capacitor is charged by the power supply over a certain amount of time and then the stored energy is injected into the antenna by a fast switching mechanism. However, if the antenna is high-*Q*, a high amount of stored energy within the capacitor will be stored again in the near-zone of the antenna and a portion of it radiates. The near-field stored energy will keep radiating while the antenna is disconnected from the capacitor. This radiation will be exponentially decaying. The damping factor of the fields is inversely related to the *Q* factor of the antenna. Hence, if the antenna has a high *Q*, a small decay in the radiating power occurs during the time that the capacitor is recharged by the battery. Figure 6.2 demonstrates the radiation mechanism of the antenna. In order to transmit the maximum power, the capacitor must be fully charged as shown in Figure 6.2(a). Once the maximum electric energy is stored, the capacitor is switched to the antenna port and provides an impulse-like excitation. Depending on the antenna *Q* factor and the switching period, the entire or part of the stored energy within the capacitor will be injected into the near-zone of the antenna if we neglect the loss. Simultaneously, antenna starts to radiate the injected power in the form of an exponentially damped oscillation. Since the capacitor contributes to the tuning mechanism, the frequency of radiated power will be determined by the loading effect of the capacitor as shown in Figure 6.2(b). Depending on the time constant of the fields, the radiated power stays above a certain level for a specific amount of time. The criteria for the lower limit of the radiated power may be determined by the required total radiated power. In the next phase, the capacitor is again connected to the DC source to be recharged. During this time, the antenna near-zone stored energy provides the radative power which is again exponentially decaying. However, since the capacitor is not connected to the antenna, the resonant frequency is the same as original resonant frequency of the antenna as shown in Figure 6.2(c). If the switching period is short compared to the time constant of the fields, the antenna will radiate continuously while alternating between two resonant frequencies and the radiated power will remain above a certain level. Minimum radiated power level is a function of switching speed. In other words, if the switching rate is high enough, the magnitude of the fields doesn't drop dramatically and the stored energy around the antenna continues to radiate with slight variations in the magnitude. Since the stored energy is already built up in the near-zone, the variation of the resonant frequency at each switching state immediately appears in the far field and therefore, similar to the previously discussed method, the high-*Q* property of the antenna won't be a limiting factor for the radiation bandwidth.

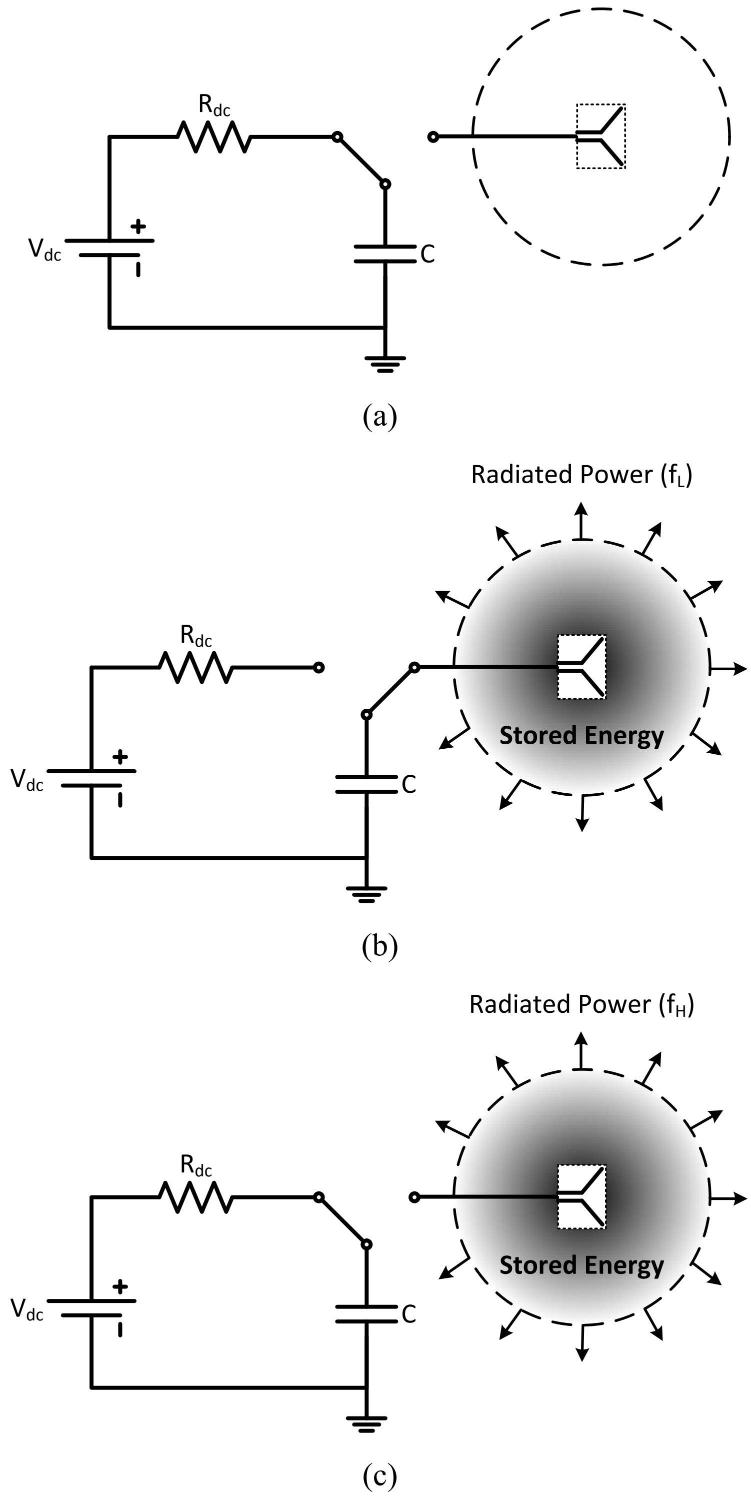

Figure 6.2: Radiation mechanism of self-contained transmitter: (a) initial charging phase, (b) injecting the energy into the antenna and simultaneously tuning the resonant frequency at f_L, (c) radiation by pre-stored near-zone energy at frequency f_H while the capacitor is being recharged.

6.3 Circuit Model

Figure 6.3 show the circuit model of the proposed self-contained transmitter. Capacitor C_2 is switched between a DC power source and a high-Q RLC resonator composed of C_1, L, and R_L. R_{dc} is the source impedance and plays a critical role in determining the upper limit of the switching rate. The major difference of this configuration with the one presented in Chapter 3 is in this case, the switched capacitor is not only a tuning component but also an intermediate element to collect the electric charge from the DC source during the charging phase and inject it into the resonator during the discharging phase. The total charge accumulated in the switched capacitor will be used to excite the resonant frequency of the resonator which determined by the value of inductor and sum of C_1 and C_2. Therefore, an efficient power transfer from the source to the load occurs if the switching period is long enough such that the switched capacitor is charged up to a certain maximum DC level. Since the time constant of the charging phase is equal to $R_{dc}C_2$, the DC impedance, R_{dc}, must be small in order to achieve a high switching rate with an efficient power transfer. Another difference of this configuration with the switched resonator of Chapter 3 is that the switching moment here is intended to be when the capacitor C_2 is sufficiently charged and its voltage is at maximum. Therefore no zero-crossing switching is required here. In addition, if the voltage across the switched capacitor is at maximum at the beginning of charging phase, i.e. the moment that C_2 is connected to the battery, required time to achieve a full charge can be substantially reduced and hence the switching rate can be increased. This is clarified in the following example which is obtained by the transient simulator of ADS software.

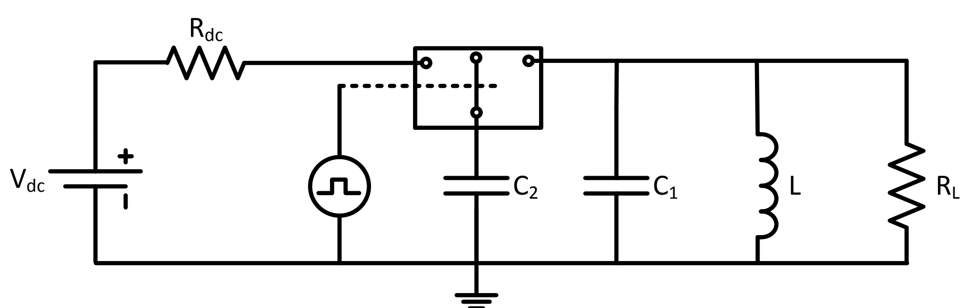

Figure 6.3: Circuit model of the self-contained transmitter.

Component values in Figure 6.3 are chosen as C_1=2546 pF, C_2=1431 pF, L=39.8 pH, R_L=50 Ω, and R_{dc}=2 Ω. These values result in two resonant frequencies at 400 MHz and 500 MHz with Q factors equal to 500 and 400, when the switched capacitor, C_2, is connected and disconnected to the RLC circuit, respectively. Within the first several cycles, the stored energy in the resonator is built up and afterward, the charging and discharging phases are similarly repeated. Figure 6.4 and Figure 6.5 show the voltage waveforms across the switched capacitor and the load as well as the consumed power which is supplied by a 1 V DC power supply. The switching frequency is a 50 MHz periodic pulse with %50 duty cycle. In Figure 6.4 initial switching cycles are shown where the stored energy in the LC pair is being built up while Figure 6.5 shows the same waveforms when they are settled down. It can be seen in Figure 6.5(b) that the load voltage is a frequency modulated waveform whose amplitude is close to 1 V for both frequencies. The voltage across the switched capacitor as depicted in Figure 6.5(a) indicates that if the switching moment is coincided with the maximum voltage, the charging time will be shorter that the case of zero voltage and therefore the rate of switching can be increased.

To study the impact of DC source resistor on the switching rate, we would consider a case in which the actual time for a full-charge is longer than the duration of charging phase. Figure 6.6 shows the switched capacitor voltage when the DC level and DC resistance are equal to 1 V and 10 Ω respectively and the switching frequency is 50 MHz. The charging curve associated with the switched capacitor voltage can be expressed as

$$V_{cha} = V_{dc} - (V_{dc} - V_R)e^{-\frac{t'}{\tau_{cha}}}, \tag{6.1}$$

where V_R is the voltage of the switched capacitor at the beginning of charging phase and t' is the delayed time originated at an arbitrary starting point of the charging phase. τ_{cha} is the charging time constant and is equal to $\tau_{cha} = R_{dc}C_2$. The envelope of exponentially decaying oscillations during the previous discharge phase can be represented by

$$V_{discha} = V_{max}e^{-\frac{t'+T_b}{\tau_{discha}}}, \tag{6.2}$$

where V_{max} is the maximum voltage during the charging phase and T_b is the bit period which is equal to a half-pulse or charging/discharging duration.

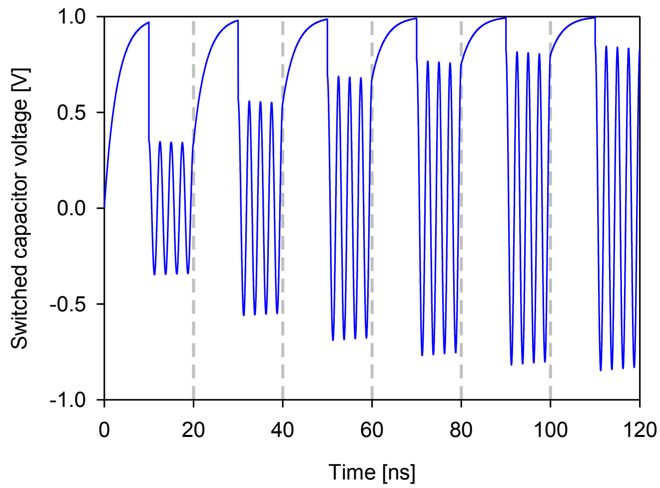

(a)

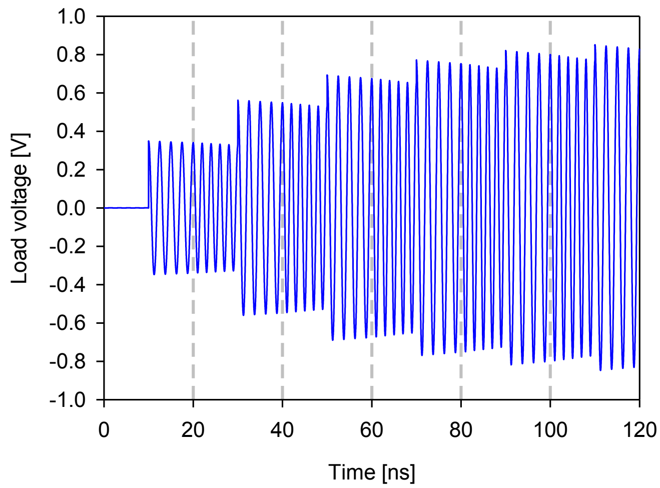

(b)

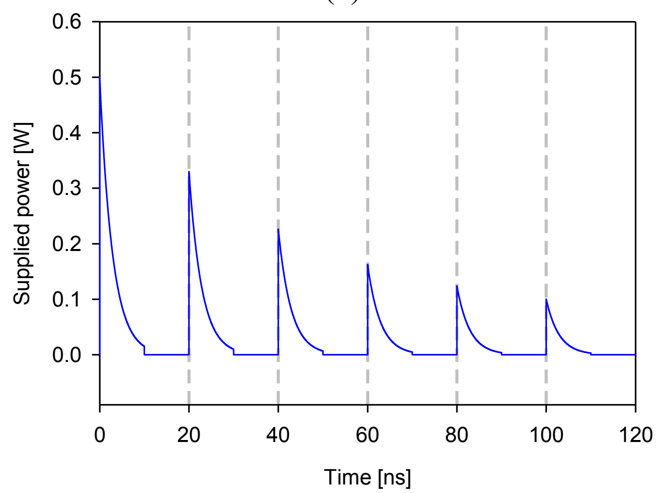

(c)

Figure 6.4: Initial switching cycles when the stored energy is being built up: (a) voltage waveform across the switched capacitor, (b) voltage waveform across the load, and (c) supplied power by the DC source.

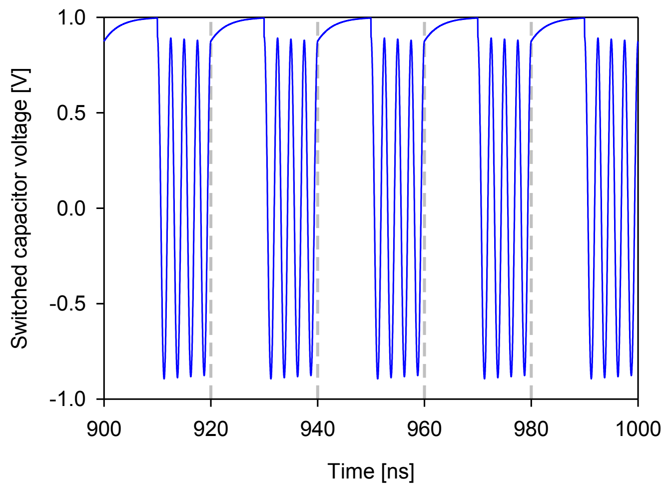

(a)

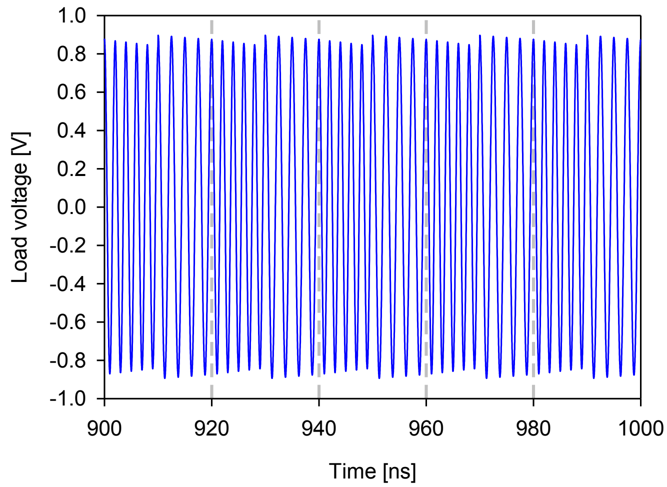

(b)

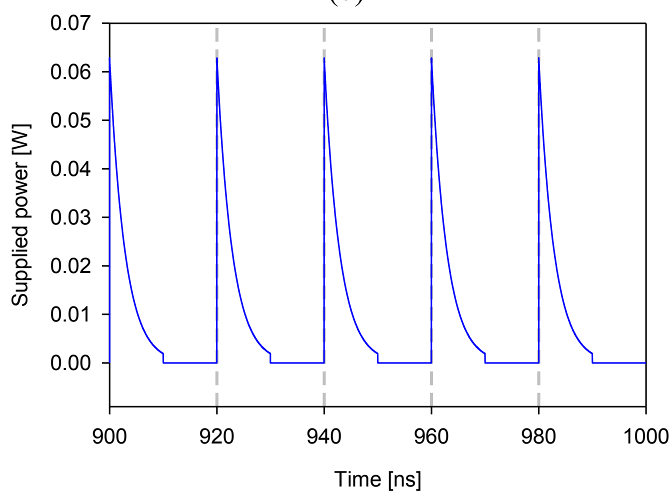

(c)

Figure 6.5: Switching cycles after the stored energy is built up: (a) voltage waveform across the switched capacitor, (b) voltage waveform across the load, and (c) supplied power by the DC source.

The τ_{discha} is the discharging time constant and is equal to $\tau_{discha} = R_L(C_1 + C_2)$. Equating (6.1) and (6.2) at $t' = 0$ results in

$$V_R = V_{max} e^{-\frac{T_b}{\tau_{discha}}}. \tag{6.3}$$

Therefore, t_0, the required time for the switched capacitor voltage to rise from V_R to V_{max} can be found by substituting (6.3) into (6.1) as

$$V_{max} = V_{dc} - \left(V_{dc} - V_{max} e^{-\frac{T_b}{\tau_{discha}}}\right) e^{-\frac{t_0}{\tau_{cha}}} \tag{6.4}$$

or

$$t_0 = R_{dc} C_2 \cdot ln\left(\frac{V_{dc} - V_{max} e^{-\frac{T_b}{R_L(C_1+C_2)}}}{V_{dc} - V_{max}}\right). \tag{6.5}$$

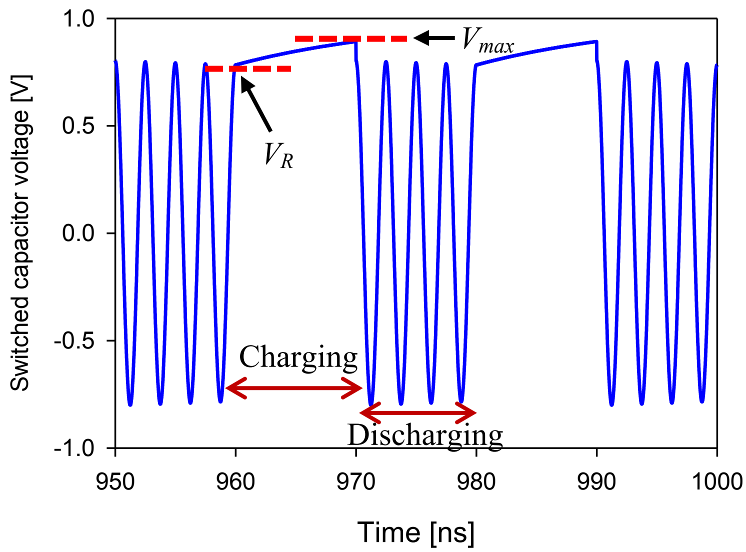

Figure 6.6: Voltage waveform across the switched capacitor in Figure 6.3, where V_{dc}=1 V and R_{dc}=10 Ω at the switching rate 50 MHz.

Equation (6.5) gives the condition which in the bit-rate is sufficiently long such that the switched capacitor voltage can reach from V_R to V_{max}

$$\frac{T_b}{ln\left(\frac{V_{dc} - V_{max} e^{-\frac{T_b}{R_L(C_1+C_2)}}}{V_{dc} - V_{max}}\right)} \geq R_{dc} C_2 \cdot \tag{6.6}$$

If we assume $V_{max} = kV_{dc}$, since $T_b = \frac{1}{2f_s}$, then (6.6) can be rewritten in terms of switching frequency as

$$f_s \cdot ln\left(\frac{1 - ke^{-\frac{1}{2f_s R_L(C_1+C_2)}}}{1-k}\right) \leq \frac{1}{2R_{dc}C_2}. \tag{6.7}$$

6.4 Direct Excitation of Electrically-Coupled Loop Antenna (ECLA)

Figure 6.7 displays the geometry of the ECLA which is used to demonstrate the directly-excited FSK modulation using a small antenna. The dimension of the antenna is the same as the one used in Section 4.4 except that the RF feeding port is eliminated and the excitation is applied directly to the edge of the capacitive plate. The antenna is simulated in CST Microwave Studio and the scattering parameters are taken into Agilent ADS for transient simulations. The measuring probe is located 1 mater away from the antenna along the co-pol electric fields as described in Section 4.4. Figure 6.8 shows the ADS circuit simulation set-up which uses an ideal single pole-double throw (SPDT) switch to switch a 3 pF capacitor between the antenna and a 1 V DC power source with a 2 Ω resistance. Figures 6.9 and 6.10 show the far field, voltage across the switched capacitor and the power supplied by the DC source for two switching frequency 25 MHz and 50 MHz, respectively. It can be seen that the far field for both cases is an FSK modulated signal with the same rate as the switching. Carrier frequencies are around 458 MHz and 648 MHz. The switched capacitor voltage quickly approaches the DC level in charging phase and resonates during the discharging phase which indicates that it contributes to the resonant frequency of radiated fields. Since the switched capacitor is small compared to the resonator model in previous section, the time constant of the charging capacitor is very short (2×3 pF=6 ps) and hence, the DC resistance is not a limiting factor in this case. Instead, the *Q* factor of the antenna is required to be high enough such that during the charging phase of the switched capacitor, the far field benefits from a small damping factor and the amount of power decay decreases. In practical cases as will be shown in the next section, a lower *Q* antenna must be switched at a higher rate to prevent the far field falling off to low levels. Therefore, similar to switched antenna presented in previous chapters, higher *Q* will be a desirable design parameter which results in maintaining an almost consistent power in the far field. It is interesting to notice that a very high-rate FSK modulation with desired frequencies is realized by a small antenna and a DC power source. The consumed power as depicted in Figures 6.9(c) and 6.10(c) shows that due to the current spikes which occur once a switching cycle, an impulse-like power is transferred from the source to the antenna at the beginning of every charging phase, provided that a high-Q switched capacitor is used. Nevertheless, a continuous radiation is achieved by using the stored energy within the near-field (during the charging phase) and the stored energy within the switched capacitor (during the discharging phase) and simultaneously the resonant frequency can be tuned according to the switched capacitance.

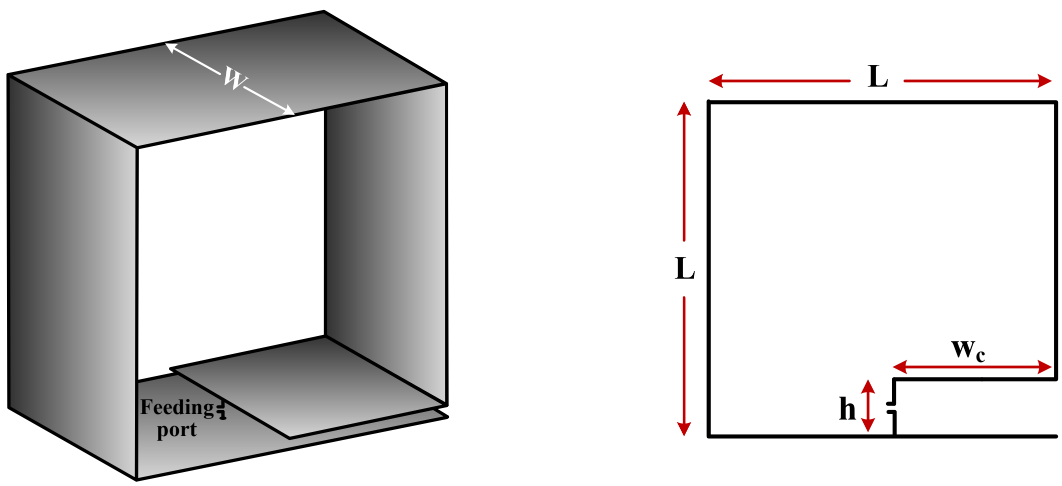

(a) (b)

Figure 6.7: Direct excited ECLA: (a) perspective view and (b) side view.

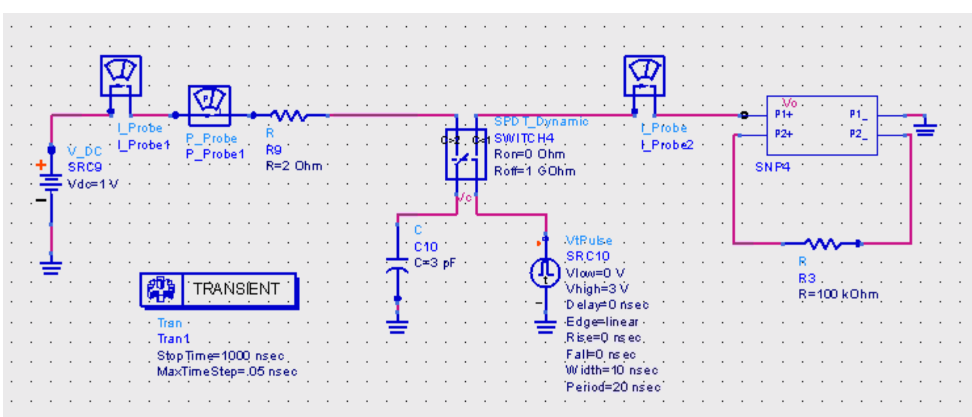

Figure 6.8: ADS simulation set-up for the direct excited ECLA.

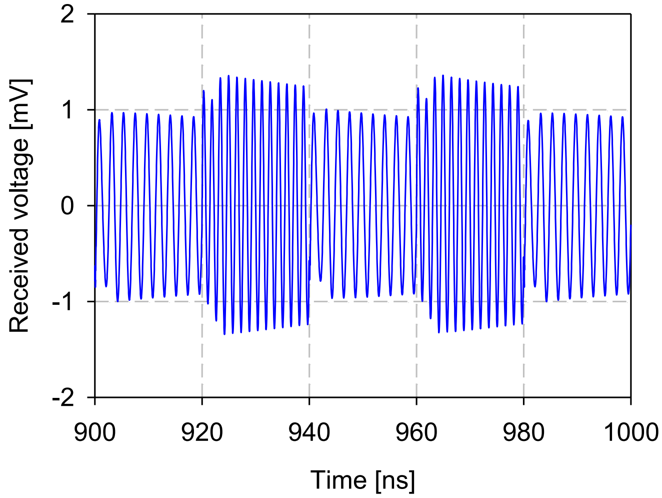

(a)

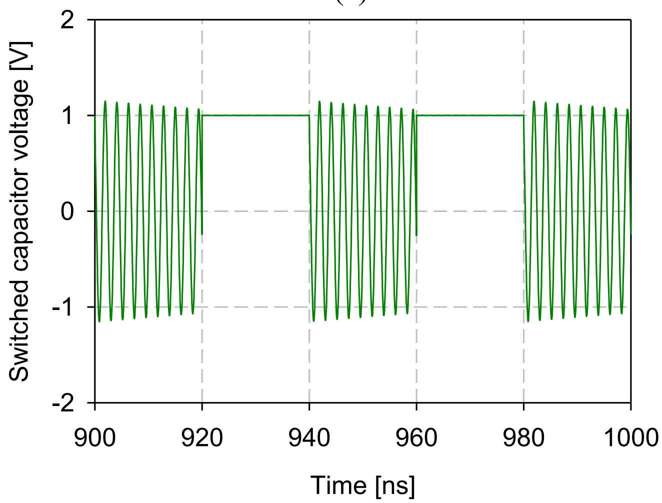

(b)

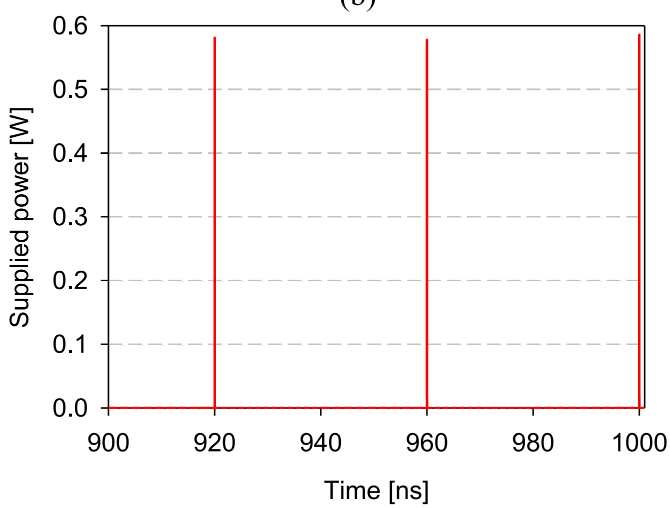

(c)

Figures 6.9: Simulation results for the switched ECLA at the rate of 25 MHz: (a) received voltage by the measuring dipole, (b) voltage across the switched capacitor, and (c) supplied power by the DC source.

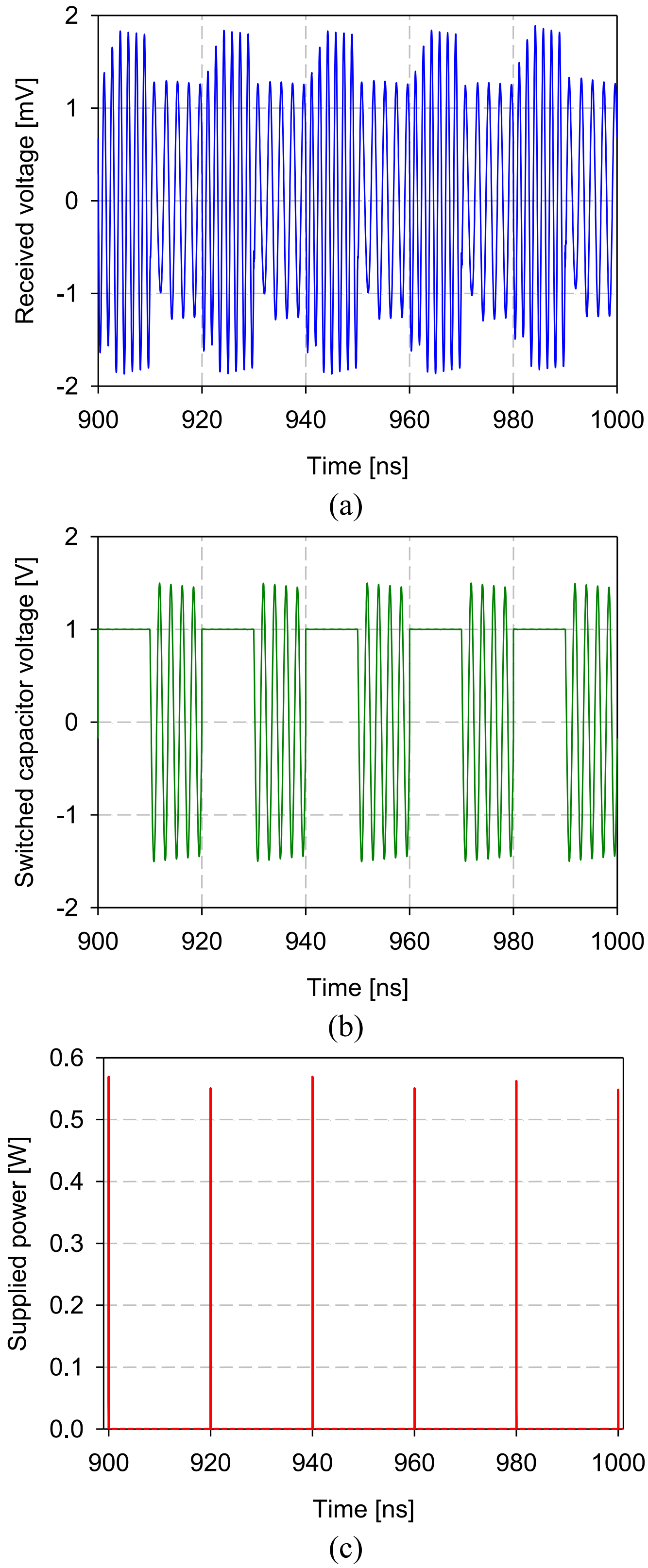

Figures 6.10: Simulation results for the switched ECLA at the rate of 50 MHz: (a) received voltage by the measuring dipole, (b) voltage across the switched capacitor, and (c) supplied power by the DC source.

6.5 Measurements

In order to implement the direct-excited antenna and demonstrate the feasibility of the proposed idea, an ECLA is prototyped according to Figure 6.7 with dimensions L=5 cm, W= 1.5 cm, w_c=1.5 cm, and h= 0.79 mm. Figure 6.11 shows the prototyped ECLA with the switching circuitry which is supported by an Rogers RT/Duroid 5870 substrate with thickness 31 mils and dielectric constant 2.33. The SPDT switch is HMC194MS8 from Hittite Microwave Corp. which is a reflective switch (i.e. open circuit when Off, versus absorptive switches which are terminated by a match load when Off) with On/Off time about 24 ns which supports a switching frequency up to 40 MHz. It should be noted that it is important to use a reflective switch in this case because during the discharging phase the battery is open circuited and therefore, no power is consumed. Also, during the charging phase the antenna is open circuited with a higher Q compared to the case that it is terminated by a 50 Ω load. The switched capacitor is 10 pF which is switched between a 3 V DC power source and the edge of capacitive plate as depicted in Figure 6.7. The voltage across the switched capacitor is shown in Figure 6.12 for two switching frequencies, 2 MHz and 8 MHz. As expected, the capacitor stores the electric energy by collecting electric charges during the charging phase and transfers the energy to the antenna during the discharging phase and at the same time contributes to the antenna resonance and causes a continuous FSK signal whose rate is a function of switching frequency rather than the antenna bandwidth. Two resonant frequencies are measured about 140 MHz and 205 MHz for the loaded and unloaded antenna, respectively. Figure 6.13 shows the measured voltage at the receiving dipole at different switching frequencies. As illustrated in the measurement results, a switching rate of 25 MHz (50 Mb/s) can be easily obtained and it can be even further increased by using a low-loss switch with improved performance along with a high-Q capacitor.

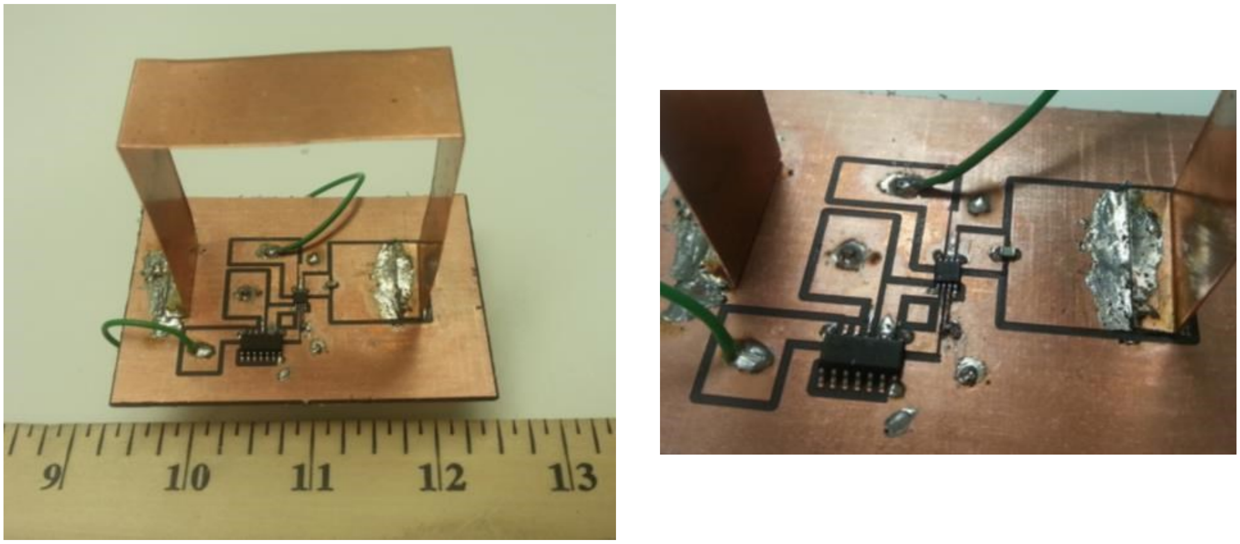

Figures 6.11: Prototyped ECLA on Rogers RT/Duroid 5870 (31 mils) for demonstration of direct-excited antenna.

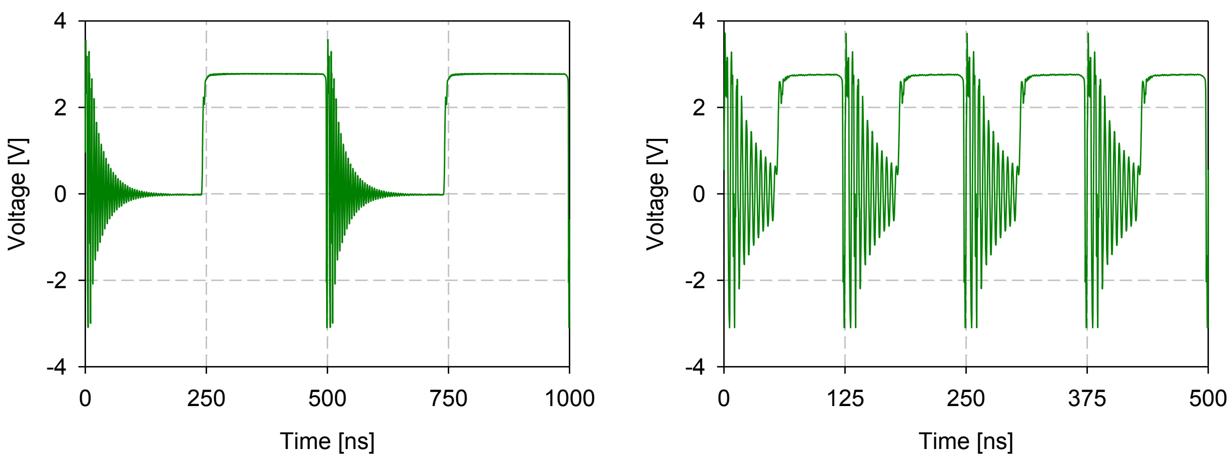

(a) (b)

Figure 6.12: Measured voltage across the switched capacitor at two switching frequencies: (a) 2 MHz and (b) 8 MHz.

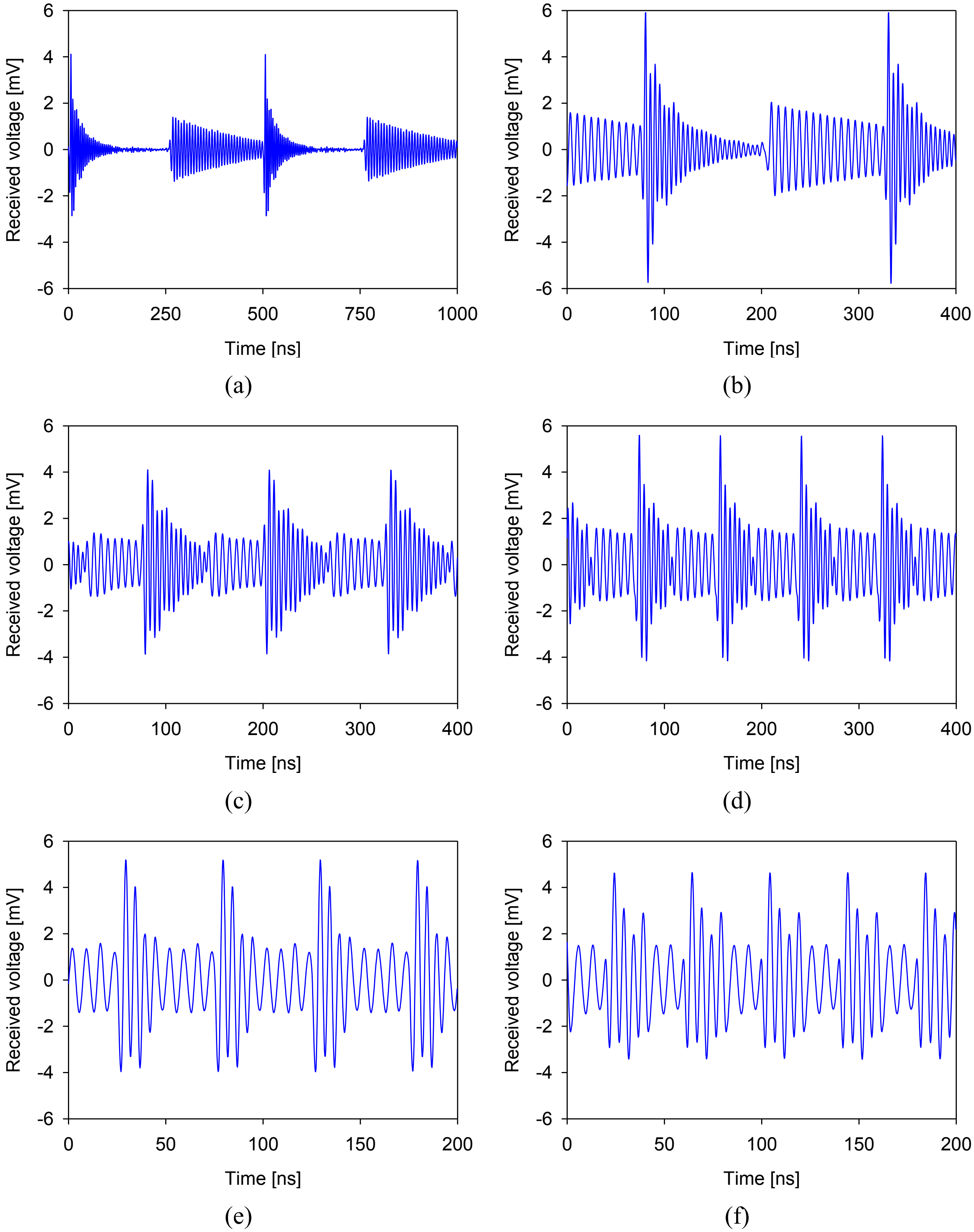

Figure 6.13: Measured voltage at the receiving dipole for different switching frequencies: (a) 2 MHz, (b) 4 MHz, (c) 8 MHz, (d) 12 MHz, (e) 20 MHz, and (f) 25 MHz.

6.6 Chapter Summary

This chapter demonstrates a minimized architecture for high-rate transmission through a small antenna. It is shown that since a transient radiation can be achieved by an initial excitation of the antenna, the proposed switched antenna in the previous chapters can be further simplified by removing the RF source and applying a DC power supply to excite the fundamental resonance of the antenna at the tuning port. A switched capacitor is used to transfer the required energy from the DC source to the antenna and provide a fast frequency-shift keying modulation without using a VCO. This technique directly utilizes the DC power supply to deliver the radiation power with minimum number of components and hence, the overall size of the transmitter is reduced. Furthermore, the battery is used only to charge the switched capacitor and therefor has a very short duty cycle if the capacitor is high-Q. Experimental results were also presented for validation.

Chapter 7

Conclusion & Future Work

This dissertation presents the time-domain characteristics of high-Q antennas and offers a neat time-varying technique to significantly increase the information bandwidth using narrowband antennas. Despite the fact that antenna designers generally tend to implement miniaturized antennas with a Q factor as low as possible, the presented work takes advantage of high-Q properties of small antennas to realize a fast frequency-shift keying modulation where the data rate is not limited by the impedance bandwidth of the antenna. A high-Q radiator is modeled by an equivalent RLC resonator and it is shown that if the natural resonant frequencies of any arbitrary narrowband antenna are switched at a proper rate by loading the antenna with a switched capacitor, the frequency of the radiated fields changes accordingly. Therefore, information data can be transmitted at a rate up to the carrier frequencies with no limitations due to the impedance bandwidth. Additionally, it is demonstrated that if the damping factor associated with the fundamental resonance is sufficiently small (which is the case for high-Q antennas), the antenna can be used completely in the transient state and switched back and forth between two resonant frequencies. If the time constant of the fields is much smaller than the switching period, a DC voltage can be used to excite the fundamental frequencies and the reactive energy stored outside of the antenna region will be sufficient to maintain a continuous radiation with minimized decaying at each resonant frequency. This chapter summarizes this dissertation and outlines the potential future work.

7.1 Summary of the Dissertation

As there are only a few attempts to decouple the impedance bandwidth of the antenna from the information bandwidth, a brief background and literature review was presented. A time-varying technique was proposed in order to modulate the resonant frequency of a small antenna such that the rate of data-transmission is not tied to the antenna bandwidth. Since it is essential to understand the time-domain characteristics of small antennas, a comprehensive survey of small antennas was presented in time domain. By using Chu's equivalent circuit for the fundamental TM_{01} mode, the radiation mechanism and the concept of stored energy in the near-zone of antennas and its relation with antenna Q was investigated. Planar inverted-F antennas (PIFA) were used as typical examples of low-profile antennas to demonstrate the transient response of small antennas and the impact of the Q factor on the near-fields as well as radiated electric fields in the far-zone. In addition, the effect of excitation signal and the source impedance on the early-time response and time constant of the fields was studied. As an essential introductory exploration, it was shown that the damping factor and time constant of the electromagnetic fields in both near and far-fields are identical and can be mimicked by an equivalent RLC resonator. This property was used to analyze a switched antenna using a circuit approach.

The theory of switched resonators was presented and it was shown that switching a reactive component in a network changes the location of the poles and causes a variation in damping factor and resonant frequency. It was demonstrated that in order to avoid switching loss due to the impulsive terms in the response of a switched resonator, it is important that the switching occurs at the zero-crossing instant of the capacitor voltage for a switched-capacitor circuit (or inductor current in case of switched-inductor circuit).

The analogy between a narrowband high-Q antenna and its equivalent resonator was used to present the theory of switched antennas. Using full-wave simulation along with the transient circuit simulations, it was proposed that if a small antenna is loaded by a switched capacitor, it is possible to modulate the resonant frequency of the antenna at a high rate up to the carrier RF frequency and realize a wideband data transmission through a miniaturized antenna. It was also shown that a single RF source is sufficient to excite both carrier frequencies. The feasibility of this idea was also investigated and experimental results were presented.

Finally, a new type of self-contained compact transmitter with dispensed RF sources was presented that resulted in a minimized architecture. Inspired by the primitive spark-gap radio transmitters, a switched capacitor was used to collect electric energy from a DC source and transfer the stored energy to the antenna in order to excite the fundamental resonance. A proper feeding position was used such that the switched capacitor contributes to the resonant frequency while injecting the stored energy into the antenna. Once the capacitor delivers a certain amount of stored energy to the antenna, it is switched back to the DC source to be charged again. On the other hand, knowing that a high amount of energy is stored in the near-zone of a high-Q antenna, this energy was used to maintain an exponentially decaying radiation when the antenna input current was switched off. Consequently, after several switching cycles the stored energy in the near-zone of the antenna is built up and provides the radiative power during the time that capacitor is being recharged. Since the frequency of this radiation is determined by the natural resonant frequency of the antenna, an FSK radiating signal similar to what presented in Chapter 4 was generated.

7.2 Suggestions for Future Work

The research in this dissertation can be extended in different ways. One of the most important keys in characterizing an antenna is the radiation pattern. Even though small antennas that excite only the fundamental TM or TE modes generally have omnidirectional doughnut-shaped radiation pattern similar to a Hertzian dipole, but that is the case in a steady-state regime. Since this research is focused on the transient-state operation of small antennas, it would be interesting to investigate how the radiation pattern evolves over the time to reach the steady state. That indicates a "time-domain radiation pattern" can be defined based on the radiated fields due to an impulse excitation. Obviously, such a radiation pattern is a superposition of all excited frequencies at a certain time and approaches the steady-state radiation pattern of the fundamental mode according to the damping factors of the higher-order modes. Consequently, some other parameters that are conventionally defined in frequency domain such as gain, directivity and radiation efficiency need to be investigated in time domain as well.

The presented research has laid the foundation for the ultimate goal of high-speed wireless communication through electrically small antennas by using a time-varying technique. However, antenna integration with RF frontends can be further studied. Implementation of other types of digital modulations using the proposed technique can be also perused. In addition to the traditional modulation schemes, this technique can be used to introduce "polarization modulation" and "*Q* modulation" as well by switching the feeding point and source impedance, respectively.

Adaptability of different types of miniaturized antennas with the proposed approach can be also examined in order to improve the antenna performance. In particular, planar antennas would be the most important class of antennas as they are widely used in many applications. For example, a planar form of electrically coupled loop antenna (ECLA) that has been used in this dissertation is demonstrated in Figure 7.1. As previously pointed out, a proper antenna choice for the presented time-varying technique is a high-*Q* and single-mode antenna.

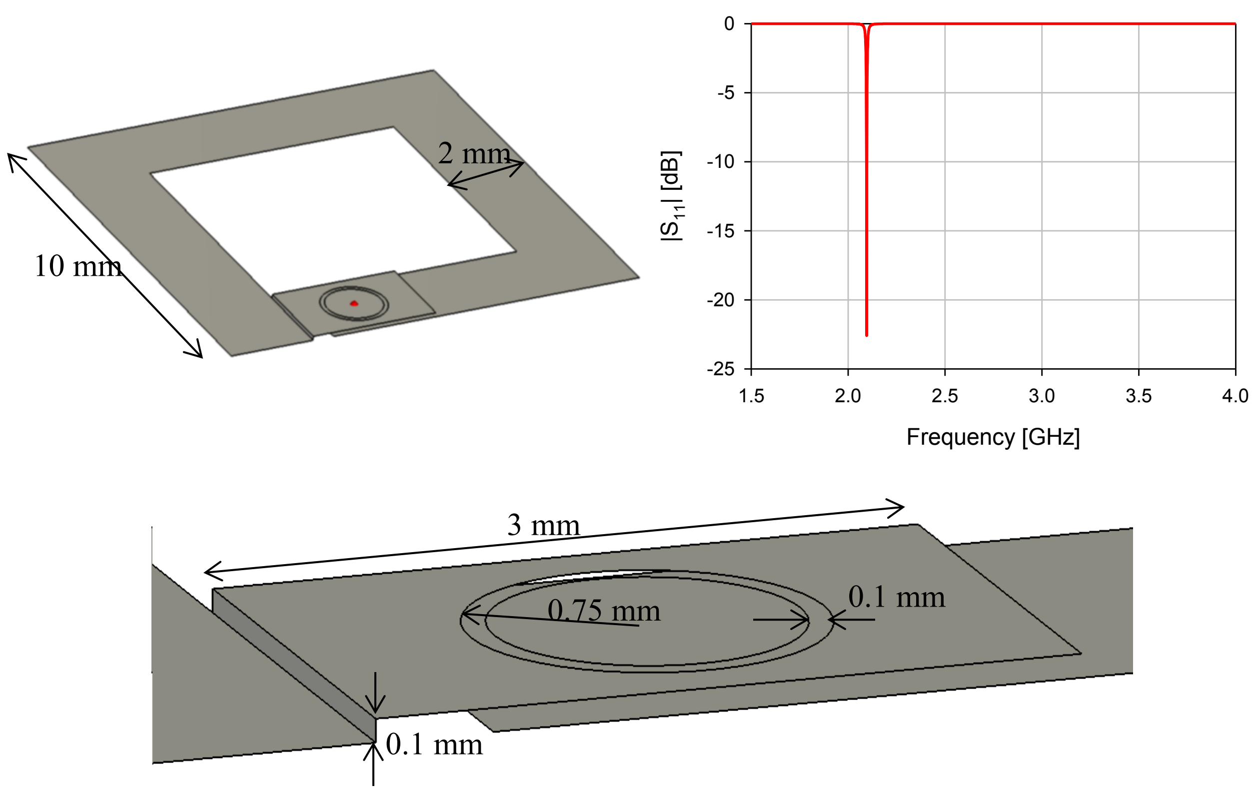

Figure 7.1: Planar form of the electrically coupled loop antenna (ECLA).

The modulation scheme used in this dissertation was a binary FSK with a single bit per symbol. However, it is possible to further increase the data rate by using a multi-tone FSK modulation. For example, a dual band antenna can be used to implement a 4-level FSK modulation with two bits per symbol which results in a doubled data rate compared to binary FSK modulation. Figure 7.2 suggests a dual-band version of planar ECLA as a good candidate for this purpose. A dual-band PIFA is also demonstrated in Figure 7.3 as a potential candidate to implement a 4-level FSK modulation using the proposed technique in this dissertation.

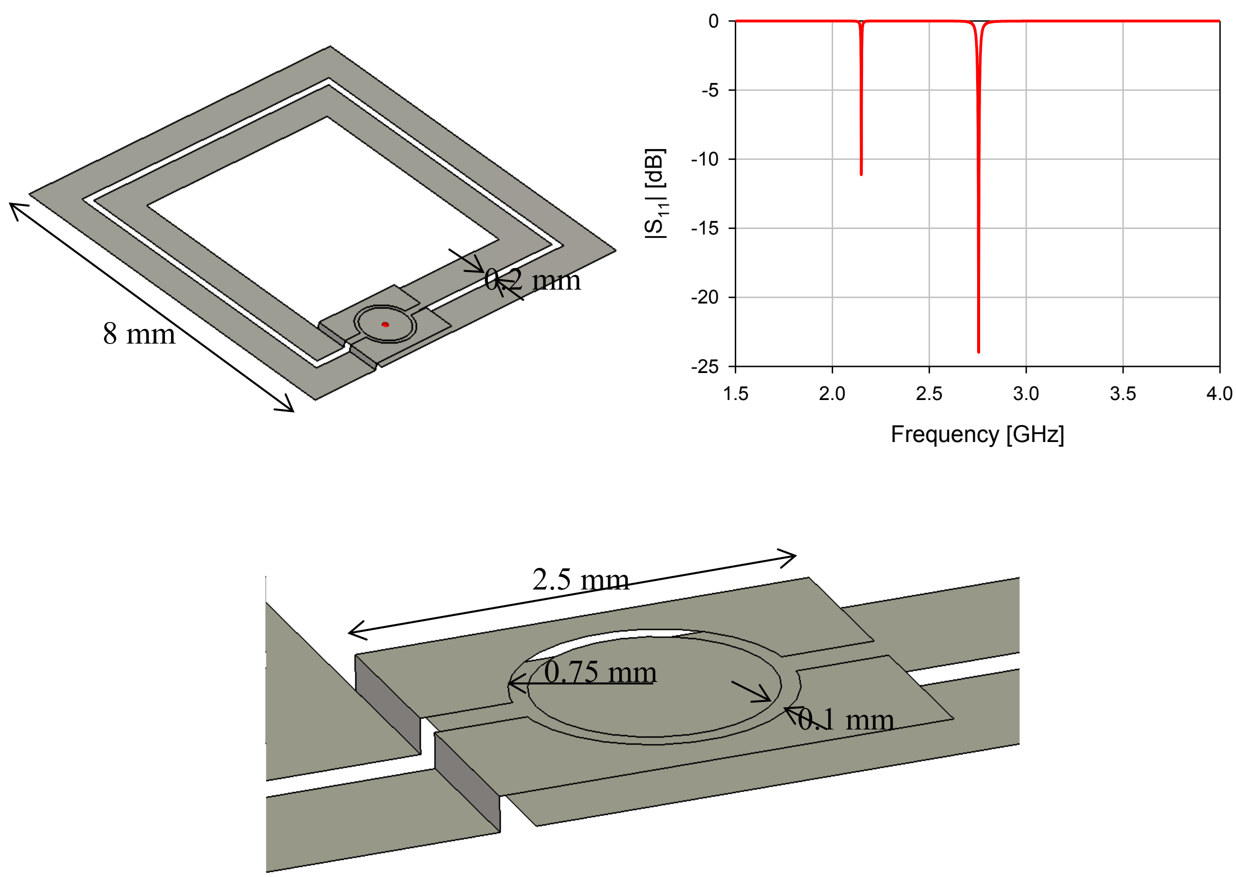

Figure 7.2: Dual-band version of the planar electrically coupled loop antenna (ECLA).

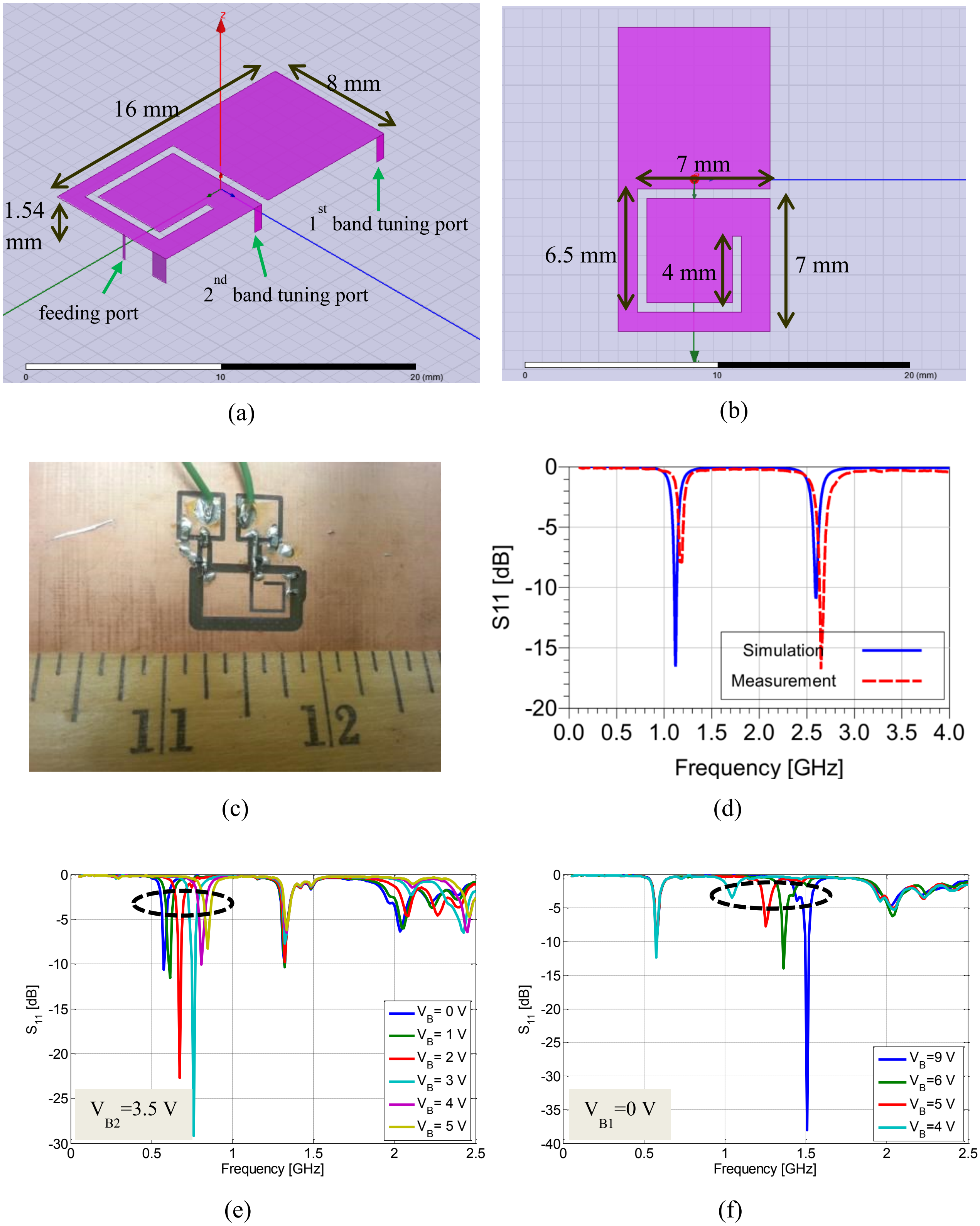

Figure 7.3: A dual-band PIFA as a potential candidate to implement a 4-level FSK modulation: (a) perspective view, (b) top view, (c) prototyped antenna, (d) return loss, (e) measured S_{11} as the 1st band is tuned, and (f) measured S_{11} as the 2st band is tuned.

References

[1] H. A. Wheeler, "Fundamental limitations of small antennas," *Proceedings of the IRE*, vol. 35, no. 12, pp. 1479-1484, 1947.

[2] L. J. Chu, "Physical limitations of omni-directional antennas," *Journal of Applied Physics*, vol. 19, no. 12, pp. 1163-1175, 1948.

[3] T.-Y. Yang, *Fundamental limits on antenna size for frequency and time domain applications*. 2012, PhD Dissertation, Virginia Polytechnic Institute and State University.

[4] H. A. Wheeler, "Fundamental limitations of small antennas," *Proceedings of the IRE*, vol. 35, no. 12, pp. 1479-1484, Dec. 1947.

[5] L. J. Chu, "Physical limitations of omni-directional antennas," *Journal of Applied Physics*, vol. 19, pp. 1163-1175, Dec. 1948.

[6] R. M. Fano, "Theoretical limitations on the broadband matching of arbitrary impedances," *MIT Tech Report 41, January 1948; also Journal of the Franklin Institute,*, vol. 249, no. 41, 1950.

[7] R. L. Tanner, "Theoretical limitations to impedance matching," *Electronics*, vol. 24, pp. 234-242, 1951.

[8] R. Harrington, "On the gain and beamwidth of directional antennas," *Antennas and Propagation, IRE Transactions on*, vol. 6, no. 3, pp. 219-225, 1958.

[9] R. F. Harrington, "Effect of antenna size on gain, bandwidth, and efficiency," *Journal of Research of the National Bureau of Standards*, vol. 64D, no. 1, pp. 1-12, 1960.

[10] R. Collin, and S. Rothschild, "Evaluation of antenna q," *Antennas and Propagation, IEEE Transactions on*, vol. 12, no. 1, pp. 23-27, 1964.

[11] R. Fante, "Quality factor of general ideal antennas," *Antennas and Propagation, IEEE Transactions on*, vol. 17, no. 2, pp. 151-155, 1969.

[12] R. Fante, and J. Mayhan, "Bounds on the electric field outside a radiating system," *Antennas and Propagation, IEEE Transactions on*, vol. 16, no. 6, pp. 712-717, 1968.

[13] R. Fante, and J. Mayhan. *Some bounds on the near electric field of a radiating system*. in *Antennas and Propagation Society International Symposium, 1968*. 1968.

[14] R. Fante, and J. Mayhan, "Bounds on the electric field outside a radiating system--ii," *Antennas and Propagation, IEEE Transactions on*, vol. 18, no. 1, pp. 64-68, 1970.

[15] H. A. Wheeler, "The radiansphere around a small antenna," *Proceedings of the IRE*, vol. 47, no. 8, pp. 1325-1331, 1959.

[16] H. Wheeler, "Small antennas," *Antennas and Propagation, IEEE Transactions on*, vol. 23, no. 4, pp. 462-469, 1975.

[17] H. Wheeler, "The wide-band matching area for a small antenna," *Antennas and Propagation, IEEE Transactions on*, vol. 31, no. 2, pp. 364-367, 1983.

[18] R. C. Hansen, "Fundamental limitations in antennas," *Proceedings of the IEEE*, vol. 69, no. 2, pp. 170-182, 1981.

[19] J. S. McLean, "A re-examination of the fundamental limits on the radiation q of electrically small antennas," *Antennas and Propagation, IEEE Transactions on*, vol. 44, no. 5, pp. 672, 1996.

[20] W. A. Davis, T. Yang, E. D. Caswell, and W. L. Stutzman, "Fundamental limits on antenna size: A new limit," *IET Microwaves, Antennas & Propagation*, vol. 5, no. 11, pp. 1297-1302, 2011.

[21] W. Geyi, "Physical limitations of antenna," *Antennas and Propagation, IEEE Transactions on*, vol. 51, no. 8, pp. 2116-2123, 2003.

[22] G. A. Thiele, P. L. Detweiler, and R. P. Penno, "On the lower bound of the radiation q for electrically small antennas," *Antennas and Propagation, IEEE Transactions on*, vol. 51, no. 6, pp. 1263-1269, 2003.

[23] A. R. Lopez, "Fundamental limtations of small antennas: Validation of wheeler's formulas," *Antennas and Propagation Magazine, IEEE*, vol. 48, no. 4, pp. 28-36, 2006.

[24] A. R. Lopez, "Review of narrowband impedance-matching limitations," *Antennas and Propagation Magazine, IEEE*, vol. 46, no. 4, pp. 88-90, 2004.

[25] P. S. Kildal, "Fundamental directivity and efficiency limitations of single- and multi-port antennas," *Antennas and Propagation, 2007. EuCAP 2007. The Second European Conference on*, pp. 1-6, 2007.

[26] P. S. Kildal, and S. R. Best, "Further investigations of fundamental directivity limitations of small antennas with and without ground planes," *Antennas and Propagation Society International Symposium, 2008. AP-S 2008. IEEE*, pp. 1-4, 2008.

[27] T. K. Sarkar, and O. Pereira, "Using the matrix pencil method to estimate the parameters of a sum of complex exponentials," *Antennas and Propagation Magazine, IEEE*, vol. 37, no. 1, pp. 48-55, 1995.

[28] A. J. Compston, J. D. Fluhler, and H. G. Schantz. *A fundamental limit on antenna gain for electrically small antennas*. in *Sarnoff Symposium, 2008 IEEE*. 2008.

[29] H. D. Foltz, and J. S. McLean. *Limits on the radiation q of electrically small antennas restricted to oblong bounding regions*. in *Antennas and Propagation Society International Symposium, 1999. IEEE*. 1999.

[30] M. C. Villalobos, H. D. Foltz, and J. S. McLean, "Broadband matching limitations for higher order spherical modes," *Antennas and Propagation, IEEE Transactions on*, vol. 57, no. 4, pp. 1018-1026, 2009.

[31] M. C. Villalobos, H. D. Foltz, J. S. McLean, and I. Sen Gupta. *Boadband tuning limits on uwb antennas based on fano's formulation*. in *Antennas and Propagation Society International Symposium 2006, IEEE*. 2006.

[32] A. D. Yaghjian, and S. R. Best, "Impedance, bandwidth, and q of antennas," *Antennas and Propagation, IEEE Transactions on*, vol. 53, no. 4, pp. 1298-1324, 2005.

[33] W. Kuntz, "A new sample-and-hold device and its application to the realization of digital filters," *Proceedings of the IEEE*, vol. 56, no. 11, pp. 2092-2093, 1968.

[34] D. L. Fried, "Analog sample-data filters," *Solid-State Circuits, IEEE Journal of*, vol. 7, no. 4, pp. 302-304, 1972.

[35] J. T. Caves, S. D. Rosenbaum, M. A. Copeland, and C. F. Rahim, "Sampled analog filtering using switched capacitors as resistor equivalents," *Solid-State Circuits, IEEE Journal of*, vol. 12, no. 6, pp. 592-599, 1977.

[36] G. C. Temes, H. J. Orchard, and M. Jahanbegloo, "Switched-capacitor filter design using the bilinear z-transform," *Ieee Transactions on Circuits and Systems*, vol. 25, no. 12, pp. 1039-1044, 1978.

[37] Y. P. Tsividis, "Analytical and experimental evaluation of a switched-capacitor filter and remarks on the resistor/switched-capacitor correspondence " *IEEE Transactions on Circuits and Systems*, vol. 26, no. 2, pp. 140-144, Feb. 1979.

[38] H. M. Sandler, and A. S. Sedra, "Programmable switched-capacitor low-pass ladder filters," *IEEE Journal of Solid-State Circuits*, vol. 21, no. 6, pp. 1109-1119, Dec. 1986.

[39] C. W. Solomon, "Switched-capacitor filters: Precise, compact, inexpensive " *IEEE Spectrum*, vol. 25, no. 6, pp. 28-32, June 1988.

[40] R. W. Brodersen, P. R. Gray, and D. Hodges, "Mos switched-capacitor filters," *Proceedings of the IEEE*, vol. 67, no. 1, pp. 61-75, Jan. 1979.

[41] S. Bang-Sup, and P. R. Gray, "Switched-capacitor high-q bandpass filters for if applications," *IEEE Journal of Solid-State Circuits*, vol. 21, no. 6, pp. 924-933, Dec. 1986.

[42] T. Ndjountche, and R. Unbehauen, "Improved structures for programmable filters: Application in a switched-capacitor adaptive filter design " *IEEE Transactions on*

Circuits and Systems II: Analog and Digital Signal Processing, vol. 46, no. 9, pp. 1137-1147, Sep. 1999.

[43] J. T. Merenda, *Synthesizer radiating systems and methods*, in *USPTO*, U.S.P. Office, Editor. 1995, Hazeltine Corporation: USA. p. 28.

[44] J. T. Merenda, *Radiation synthesizer systems and methods*, in *USPTO*, U.S.P. Office, Editor. 2001, BAE Systems Advanced Systems: USA. p. 20.

[45] J. T. Merenda, *Radiation synthesizer feed configurations*, in *USPTO*, U.S.P. Office, Editor. 2003, BAE Systems Information and Electronic Systems Integration Inc.: USA. p. 12.

[46] J. T. Merenda, *Radiation synthesizer receive and transmit systems*, in *USPTO*, U.S.P. Office, Editor. 2003, Bae Systems Information and Electronic Systems Integration, Inc.: USA. p. 11.

[47] J. T. Merenda, "Waveform-synthesis method that reduces battery power in an electrically small wideband radiating system," *IET Microwaves, Antennas & Propagation*, vol. 2, no. 1, pp. 59-65, 2008.

[48] V. F. Fusco, and Q. Chen, "Direct-signal modulation using a silicon microstrip patch antenna," *IEEE Transactions on Antennas and Propagation*, vol. 47, no. 6, pp. 1025-1028, June 1999.

[49] H. C. Jing, and Y. E. Wang, "Efficient monocycle pulse transmitting from patch antennas," *Antennas and Propagation Society International Symposium 2006, IEEE*, pp. 905-908, 2006.

[50] H. C. Jing, and Y. E. Wang, "A uwb pulse transmission scheme - switched resonant antenna," *Ultra-Wideband, The 2006 IEEE 2006 International Conference on*, pp. 551-555, 2006.

[51] Y. Weijun, and W. Yuanxun Ethan, "An integrated antenna for pulse modulation and radiation," *Radio and Wireless Conference, 2004 IEEE*, pp. 427-429, 2004.

[52] Y. Weijun, and W. Yuanxun Ethan, "Radiating beyond the bandwidth using direct antenna modulation," *Antennas and Propagation Society International Symposium, 2004. IEEE*, vol. 1, pp. 791-794 Vol.1, 2004.

[53] Y. Weijun, and W. Yuanxun, "Direct antenna modulation - a promise for ultra-wideband (uwb) transmitting," *Microwave Symposium Digest, 2004 IEEE MTT-S International*, vol. 2, pp. 1273-1276 Vol.2, 2004.

[54] X. Xiaojing, H. C. Jing, and Y. E. Wang, "High speed pulse radiation from switched electrically small antennas," *Antennas and Propagation Society International Symposium 2006, IEEE*, pp. 167-170, 2006.

[55] S. D. Keller, W. D. Palmer, and W. T. Joines, "Digitally driven antenna for hf transmission," *IEEE Transactions on Microwave Theory and Techniques*, vol. 58, no. 9, pp. 2362-2367, Sep. 2010.

[56] W. Xin, L. P. B. Katehi, and D. Peroulis. *Time-varying matching for receiving wideband pulse through electrically small antennas*. in *Antennas and Propagation Society International Symposium, 2008. AP-S 2008. IEEE*. 2008.

[57] W. Xin, L. P. B. Katehi, and D. Peroulis, "Time-varying matching networks for signal-centric systems," *Microwave Theory and Techniques, IEEE Transactions on*, vol. 55, no. 12, pp. 2599-2613, 2007.

[58] W. Xin, L. P. B. Katehi, and D. Peroulis. *Time-varying matching network for antennas in pulse-based systems*. in *Antennas and Propagation Society International Symposium, 2007 IEEE*. 2007.

[59] W. Xin, L. P. B. Katehi, and D. Peroulis. *Time-domain impedance adaptors for pulse-based systems with high q rc loads*. in *Microwave Symposium, 2007. IEEE/MTT-S International*. 2007.

[60] W. Xin, D. Peroulis, and L. Katehi. *Time-varying matching networks for antennas*. in *Antennas and Propagation, 2007. EuCAP 2007. The Second European Conference on*. 2007.

[61] X. Wang, L. P. B. Katehi, and D. Peroulis, "Signal-to-noise ratio performance of a time-varying matching network for pulse-based systems," *IEEE Transactions on Microwave Theory and Techniques*, vol. 59, no. 2, pp. 323-337, Feb. 2011.

[62] L. Yumin, L. P. B. Katehi, and D. Peroulis. *A novel mems impedance tuner simultaneously optimized for maximum impedance range and power handling*. in *Microwave Symposium Digest, 2005 IEEE MTT-S International*. 2005.

[63] M. Manteghi, "Antenna miniaturization beyond the fundamental limits using impedance modulation," *IEEE Antennas and Propagation Society International Symposium (APSURSI)*, pp. 1-4, 2009.

[64] M. Manteghi, "Non-lti systems, a new frontier in electromagnetics theory," *IEEE Antennas and Propagation Society International Symposium (APSURSI)*, pp. 1-4, 2010.

[65] M. Salehi, and M. Manteghi, "Bandwidth enhancement using nonlinear inductors," *IEEE International Symposium on Antennas and Propagation (APSURSI)*, pp. 814-816, July 2011.

[66] M. Manteghi, "A switch-band antenna for software-defined radio applications," *Antennas and Wireless Propagation Letters* vol. 8, pp. 3-5, 2009.

[67] M. Manteghi, "A tunable planar inverted-f antenna for digital video broadcast-handheld applications," *Microwave and Optical Technology Letters*, vol. 54, pp. 2635-2638, 2012.

[68] A. C. K. Mak, C. R. Rowell, R. D. Murch, and C. L. Mak, "Reconfigurable multiband antenna designs for wireless communication devices," *IEEE Transactions on Antennas and Propagation*, vol. 55, no. 7, pp. 1919–1928, July 2007.

[69] F. Xiong, and R. R. Romanofsky, "Study of behavior of digital modulations for beam steerable reflectarray antennas," *IEEE Transactions on Antennas and Propagation*, vol. 53, no. 3, pp. 1083–1097, Mar. 2005.

[70] X. Wang, L. P. B. Katehi, and D. Peroulis, "Analysis and measurement of a time-varying matching scheme for pulse-based receivers with high-q sources," *IEEE Transactions on Microwave Theory and Techniques*, vol. 58, no. 8, pp. 2231–2243, Aug. 2010.

[71] L. Wang, M. Yuan, T. Xiao, W. T. Joines, and Q. H. Liu, "Broadband electromagnetic radiation modulated by dual memristors," *IEEE Antennas and Wireless Propagation Letters*, vol. 10, pp. 623–626, 2011.

[72] J. A. McGregor, E. M. Poulter, and M. J. Smith, "Switching system for single antenna operation of an s-band fmcw radar," *IEE Proceedings Radar, Sonar and Navigation*, vol. 141, no. 4, pp. 241–248, Aug. 1994.

[73] G. A. E. Vandenbosch, "Reactive energies, impedance, and q factor of radiating structures," *IEEE Transactions on Antennas and Propagation*, vol. 58, no. 4, pp. 1112-1127, Apr. 2010.

[74] H. L. Thal, "New radiation q limits for spherical wire antennas," *IEEE Transactions on Antennas and Propagation*, vol. 54, no. 10, pp. 2757-2763, Oct. 2006.

[75] D. Yaghjian, and S. R. Best, "Impedance, bandwidth and q of antennas," *IEEE Transactions on Antennas and Propagation*, vol. 53, no. 4, pp. 1298- 1324, Apr. 2005.

[76] J. S. McLean, "A re-examination of the fundamental limits on the radiation q of electrically small antennas," *IEEE Transactions on Antennas and Propagation*, vol. AP-44, pp. 672-675, May 1996.

[77] P. Hansen, and R. Adams, "The minimum q for spheroidally shaped objects: Extension to cylindrically shaped objects and comparison to practical antennas," *IEEE Antennas and Propagation Magazine*, vol. 53, no. 3, pp. 75-83, June 2011.

[78] G. A. E. Vandenbosch, "Simple procedure to derive lower bounds for radiation q of electrically small devices of arbitrary topology," *IEEE Transactions on Antennas and Propagation*, vol. 59, no. 6, pp. 2217-2225, June 2011.

[79] H. L. Thal, "Q bounds for arbitrary small antennas: A circuit approach," *IEEE Transactions on Antennas and Propagation*, vol. 60, no. 7, pp. 3120-3128, July 2012.

[80] M. Capek, P. Hazdra, and J. Eichler, "A method for the evaluation of radiation q based on modal approach," *IEEE Transactions on Antennas and Propagation*, vol. 60, no. 10, pp. 4556-4567, Oct. 2012.

[81] O. S. Kim, "Minimum q electrically small antennas," *IEEE Transactions on Antennas and Propagation*, vol. 60, no. 8, pp. 3551-3558, Aug. 2012.

[82] W. Geyi, P. Jarmuszewski, and Y. Qi, "The foster reactance theorem for antennas and radiation q," *IEEE Transactions on Antennas and Propagation*, vol. 48, no. 3, pp. 401-408, Mar. 2000.

[83] G. Kaiser, "The reactive energy of transient em fields," *arXiv:.1201.6575v2*, July 2012.

[84] G. A. E. Vandenbosch, "Radiators in time domain, part i: Electric, magnetic and radiated energies," *IEEE Transactions on Antennas and Propagation*, vol. 61, no. 8, pp. 3995–4003, Aug. 2013.

[85] G. A. E. Vandenbosch, "Radiators in time domain, part ii: Finite pulses, sinusoidal regime and q factor," *IEEE Transactions on Antennas and Propagation*, vol. 61, no. 8, pp. 4004–4012, Aug. 2013.

[86] A. Shlivinski, and E. Heyman, "Time-domain near-field analysis of short-pulse antennas – part i: Spherical wave (multipole) expansion," *IEEE Transactions on Antennas and Propagation*, vol. 47, no. 2, pp. 271-279, Feb. 1999.

[87] A. Shlivinski, and E. Heyman, "Time-domain near-field analysis of short-pulse antennas – part ii: Reactive energy and the antenna q," *IEEE Transactions on Antennas and Propagation*, vol. 47, no. 2, pp. 280-286, Feb. 1999.

[88] A. Shlivinski, E. Heyman, and R. Kastner, "Antenna characterization in the time domain," *IEEE Transactions on Antennas and Propagation*, vol. 45, no. 7, pp. 1140–1149, July 1997.

[89] C. E. Baum, and E. G. Farr, "Extending the definitions of antennas gain and radiation pattern into the time domain," *Sensor & Simulation Notes*, no. 350, 1992.

[90] R. F. Harrington, and J. R. Mautz, "Theory of characteristic modes for conducting bodies," *IEEE Transactions on Antennas and Propagation*, vol. Ap-19, no. 5, pp. 622–628, Sep. 1971.

[91] R. J. Garbaczand, and R. H. Turpin, "A generalized expansion for radiated and scattered fields," *IEEE Transactions on Antennas and Propagation*, vol. AP-19, no. 3, pp. 348–358, May 1971.

[92] C. E. Baum, "On the singularity expansion method for the solution of electromagnetic interaction problems," *AWFL Interaction*, no. 88, Dec. 1971.

[93] F. M. Tesche, "On the analysis of scattering and antenna problems using the singularity expansion technique," *IEEE Transactions on Antennas and Propagation*, vol. AP-21, no. 1, pp. 53–62, Jan. 1973.

[94] M. L. V. Blaricum, and R. Mittra, "A technique for extracting the poles and residues of a system directly from its transient response," *IEEE Transactions on Antennas and Propagation*, vol. AP-23, no. 6, pp. 777–781, Nov. 1975.

[95] S. Licul, and W. A. Davis, "Unified frequency and time-domain antenna modeling and characterization," *IEEE Transactions on Antennas and Propagation*, vol. 53, no. 9, pp. 2882–2888, Sep. 2005.

[96] R. Rezaiesarlak, and M. Manteghi, "Short-time matrix pencil method for chipless rfid detection applications," *IEEE Transactions on Antennas and Propagation*, vol. 61, no. 5, pp. 2801-2806 May 2013.

[97] R. Rezaiesarlak, and M. Manteghi, "Complex natural resonance-based design of chipless rfid tag for high density data," *IEEE Transactions on Antennas and Propagation*, DOI: 10.1109/TAP.2013.2290998, 2013.

[98] P. A. Tirkas, and C. A. Balanis, "Finite-difference time-domain method for antenna radiation," *IEEE Transactions on Antennas and Propagation*, vol. 40, no. 3, pp. 334–340, Mar. 1992.

[99] J. G. Maloney, G. S. Smith, and W. R. Scott, "Accurate computation of the radiation from simple antennas using the finite-difference time-domain method," *IEEE Transactions on Antennas and Propagation*, vol. 38, no. 7, pp. 1059–1068, July 1990.

[100] J. D. Jackson, *Classical electrodynamics*. 1998, Hoboken, NJ: Wiley.

[101] M. Manteghi, "Impulse response and transient near-field of a hertzian dipole," *Proc. 2013 Radio Science Meeting, USNC-URSI*, Jan. 2013.

[102] G. Kaiser, "Electromagnetic inertia, reactive energy, and energy flow velocity," *Journal of Physics A: Mathematical and Theoretical*, vol. 44, no. 34, pp. 1-15, 2011.

[103] H. Schantz, *The art and science of ultrawideband antennas*. 2005, Norwood, MA: Artech House.

[104] G. M. Rebeiz, *Rf mems: Theory, design, and technology*. 2003, Hoboken, NJ: Wiley.

[105] X. Wang, L. P. B. Katehi, and D. Peroulis, "Time-varying matching networks for signal-centric systems," *IEEE Transactions on Microwave Theory and Techniques*, vol. 55, no. 12, pp. 2599–2613, Dec. 2007.

[106] L. N. Pringle, P. H. Harms, S. P. Blalock, G. N. Kiesel, E. J. Kuster, P. G. Friederich, R. J. Prado, J. M. Morris, and G. S. Smith, "A reconfigurable aperture antenna based on switched links between electrically small metallic patches," *IEEE Transactions on Antennas And Propagation*, vol. 52, no. 6, pp. 1434-1445, June 2004.

[107] P. Scheele, A. Kilian, A. Giere, and R. Jakoby, "Switching-mode mixers based on tunable filters," *Electronics Lette*, vol. 42, no. 23, pp. 1-2, Nov. 2006.

[108] H. Darabi, A. Mirzaei, and M. Mikhemar, "Highly integrated and tunable rf frontends for reconfigurable multiband transceivers: A tutorial," *IEEE Transactions on Circuits and Systems I*, vol. 58, no. 9, pp. 2038–2050, Sep. 2011.

[109] J. A. Guinea, and D. Senderowicz, "A differential narrow-band switched capacitor filtering technique," *IEEE Journal of Solid-State Circuits* vol. SC-17, no. 6, pp. 1029–1038, Dec. 1982.

[110] J. Chen, and A. Ioinovici, "Switching-mode dc-dc converter with switched-capacitor-based resonant circuit " *IEEE Transactions on Circuits and Systems-I: Fundamental Theory and Applications*, vol. 43, no. 11, pp. 933-938, Nov. 1996.

[111] S. Kim, and Y. E. Wang, "Theory of switched rf resonators," *IEEE Transactions on Circuits and Systems I*, vol. 53, no. 12, pp. 2521–2528, Dec. 2006.

[112] Y. P. Tsividis, "Analysis of switched capacitive networks," *IEEE Transactions on Circuits and Systems*, vol. CAS-26, no. 11, pp. 935–947, Nov. 1979.

[113] D. Bedrosian, and J. Vlach, "Time-domain analysis of networks with internally controlled switches," *IEEE Transactions on Circuits and Systems I: Fundamental Theory and Applications*, vol. 39, no. 3, pp. 199–212, Mar. 1992.

[114] F. Yuan, and A. Opal, "Computer methods for switched circuits," *IEEE Transactions on Circuits and Systems I: Fundamental Theory and Applications*, vol. 50, no. 8, pp. 1013–1024, Aug. 2003.

[115] A. Opal, and J. Vlach, "Consistent initial conditions of linear switched network," *IEEE Transactions on Circuits and Systems*, vol. 37, no. 3, pp. 364–372, Mar. 1990.

[116] M. Keskin, U.-K. Moon, and G. C. Temes, "Switched-capacitor resonator structure with improved performance " *Electronics Letters* vol. 37, no. 4, pp. 212-213, Feb. 2001.

[117] K. Miyachi, H. Nakano, and T. Saito, "Response of a simple dependent switched capacitor circuit to a pulse-train input," *IEEE Transactions on Circuits and Systems—I: Fundamental Theory and Applications*, vol. 50, no. 9, pp. 1180-1187, Sep. 2003.

[118] J. G. Proakis, and M. Salehi, *Digital communications*. 5th ed. 2008, NY: McGraw Hill.

[119] L. J. Chu, "Physical limitations on omni-directional antennas," *Journal of Applied Physics*, vol. 19, pp. 1163-1175, Dec. 1948.

[120] R. F. Harrington, "Effect of antenna size on gain, bandwidth, and efficiency," *Journal of Research of the National Bureau of Standards*, vol. 64D, pp. 1-12, Jan.–Feb. 1960.

[121] M. Z. Win, D. Dardari, A. F. Molisch, W. Wiesbeck, and J. Zhang, "History and applications of uwb," *Proceedings of the IEEE*, vol. 97, no. 2, pp. 198-204, Feb. 2009.

[122] L. Liu, S. W. Cheung, and T. I. Yuk, "Compact mimo antenna for portable devices in uwb applications," *IEEE Transactions on Antennas and Propagation*, vol. 61, no. 8, pp. 4257-4264, Aug. 2013.

[123] A. Elsherbini, and K. Sarabandi, "Directive coupled sectorial loops antenna for ultrawideband applications," *IEEE Antennas and Wireless Propagation Letters*, vol. 8, pp. 576-579, 2009.

[124] A. Azari, A. Ismail, A. Sali, and F. Hashim, "A new super wideband fractal monopole-dielectric resonator antenna," *IEEE Antennas and Wireless Propagation Letters*, vol. 12, pp. 1014-1016, 2013.

[125] M. Ojaroudi, G. Ghanbari, N. Ojaroudi, and C. Ghobadi, "Small square monopole antenna for uwb applications with variable frequency band-notch function," *IEEE Antennas and Wireless Propagation Letters*, vol. 8, pp. 1061-1064, 2009.

[126] C.-Y.-D. Sim, W.-T. Chung, and C.-H. Lee, "Compact slot antenna for uwb applications," *IEEE Antennas and Wireless Propagation Letters*, vol. 9, pp. 63-66, 2010.

[127] C.-H. Wu, and K.-L. Wong, "Ultrawideband pifa with a capacitive feed for penta-band folder-type mobile phone antenna," *IEEE Transactions on Antennas and Propagation*, vol. 57, no. 60, pp. 2461-2464, Aug. 2009.

[128] K. Rambabu, H. A. Thiart, J. Bornemann, and S. Y. Yu, "Ultrawideband printed-circuit antenna," *IEEE Transactions on Antennas and Propagation*, vol. 54, no. 12, pp. 3908-3911, Dec. 2006.

[129] H. W. Alsawaha, and A. Safaai-Jazi, "Ultrawideband hemispherical helical antennas," *IEEE Transactions on Antennas and Propagation*, vol. 58, no. 10, pp. 3175-3181, Oct. 2010.

[130] N. Behdad, M. A. Al-Joumayly, and M. Salehi, *Ultra-wideband, low profile antenna*. 2012: US 8228251.

[131] N. Behdad, and K. Sarabandi, "A compact antenna for ultrawide-band applications," *IEEE Transactions on Antennas and Propagation*, vol. 53, no. 7, pp. 2185-2192, 2005.

[132] M. Ghovanloo, and K. Najafi, "A wideband frequency-shift keying wireless link for inductively powered biomedical implants," *IEEE Transactions on Circuits and Systems—I: Regular Papers*, vol. 51, no. 12, pp. 2374-2383, Dec. 2004.

[133] H. Miranda, V. Gilja, C. A. Chestek, K. V. Shenoy, and T. H. Meng, "Hermesd: A high-rate long-range wireless transmission system for simultaneous multichannel neural recording applications," *IEEE Transactions on Biomedical Circuits and Systems*, vol. 4, no. 3, pp. 181-191, Jun. 2010.

[134] S. B. Lee, M. Yin, J. R. Manns, and M. Ghovanloo, "A wideband dual-antenna receiver for wireless recording from animals behaving in large arenas," *IEEE Transactions on Biomedical Circuits and Systems*, vol. 60, no. 7, pp. 1993-2004, July 2013.

[135] H. A. Wheeler, "Fundamental limitations of small antennas," *Proceedings of the IRE*, vol. 35, pp. 1479-1484, Dec. 1947.

[136] D. H. Schaubert, "Application of prony's method to time-domain reflecto-meter data and equivalent circuit synthesis," *IEEE Transactions on Antennas and Propagation*, vol. 27, no. 2, pp. 180-184, March 1979.

[137] S. A. Schelkunoff, "Representation of impedance functions in terms of resonant frequencies," *Proceedings of the I.R.E.*, vol. 32, pp. 83-90, Feb. 1944.

[138] Y. Kim, and H. Ling, "Equivalent circuit modeling of broadband antennas using a rational function approximation," *Microwave and Optical Technology Letter*, vol. 48, no. 5, pp. 950-953, May 2006.

[139] R. S. Adve, T. K. Sarkar, S. M. Rao, E. K. Miller, and D. R. Pflug, "Application of the cauchy method for extrapolating/interpolating narrow-band system responses," *IEEE Transactions on Microwave Theory and Techniques*, vol. 45, no. 5, pp. 837-845, May 1997.

[140] K. A. Michalski, and L. W. Pearson, "Equivalent circuit synthesis for a loop antenna based on the singularity expansion method," *IEEE Transactions on Antennas and Propagation*, vol. 32, no. 5, pp. 433-441, May 1984.

[141] T. L. Simpson, J. C. Logan, and J. W. Rockway, "Equivalent circuits for electrically small antennas using ls-decomposition with the method of moments " *IEEE Transactions on Antennas and Propagation*, vol. 37, no. 12, pp. 1632-1635, Dec. 1989.

[142] M. Hamid, and R. Hamid, "Equivalent circuit of dipole antenna of arbitrary length," *IEEE Transactions on Antennas and Propagation*, vol. 45, no. 11, pp. 1695-1696, Nov. 1997.

[143] A. W. Love, "Equivalent circuit for aperture antennas," *Electronics Letters* vol. 23, no. 13, pp. 708 - 710.

[144] P. Vainikainen, J. Ollikainen, O. Kivekäs, and I. Kelander, "Resonator-based analysis of the combination of mobile handset antenna and chassis," *IEEE Transactions on Antennas and Propagation*, vol. 50, no. 10, Oct. 2002.

[145] T. G. Tang, Q. M. Tieng, and M. W. Gunn, "Equivalent circuit of a dipole antenna using frequency-independent lumped elements," *IEEE Transactions on Antennas and Propagation*, vol. 41, no. 1, pp. 100-103, Jan. 1993.

[146] G. W. Streable, and L. W. Pearson, "A numerical study on realizable broad-band and equivalent admittances for dipole and loop antennas," *IEEE Transactions on Antennas and Propagation*, vol. 29, no. 5, pp. 707-717, Sep. 1981.

[147] G. K. H. Liu, and R. D. Murch, "Compact dual-frequency pifa design using lc resonators," *IEEE Transactions on Antennas and Propagation*, vol. 50, no. 10, pp. 1433-1444, Oct. 2002.

[148] M. Salehi, and M. Manteghi, "A wideband frequency-shift keying modulation technique using transient state of a small antenna," *Progress In Electromagnetics Research*, vol. 143, pp. 421-445, 2013.

[149] M. Manteghi, "Electrically coupled loop antenna as a dual for the planar inverted-f antenna," *Microwave and Optical Technology Letters*, vol. 55, no. 6, pp. 1409-1412, June 2013.

[150] T. M. Hancock, and G. M. Rebeiz, "Design and analysis of a 70-ps sige differential rf switch," *IEEE Transactions on Microwave Theory and Techniques*, vol. 53, no. 7, pp. 2403-2410, July 2005.

[151] *The pin diode circuit designers' handbook*. 1998, Watertown, MA: Microsemi-Watertown.

[152] *Application note 922*, in *Applications of PIN Diodes*. Avago Technologies, http://www.avagotech.com/docs/5965-8666E.

[153] E. T. Seton, *The woodcraft manual for boys*. 1917, Garden City, NY: Doubleday, Page & Co.

[154] A. A. Huurdeman, *The worldwide history of telecommunications*. 2003, Hoboken, NJ: Wiley.

[155] J. Blanchard, "The history of electrical resonance," *Bell System Technical Journal* vol. 20, no. 4, pp. 415-433, Oct. 1941.

[156] "Prof. D. E. Hughes' research in wireless telegraphy," *The Electrician* vol. 3, pp. 40-41, May 1899.

[157] H. Hertz, "Ueber sehr schnelle elektrische schwingungen," *Ann. Physik usnd Chemie (Wiedeman) N. F.*, vol. 31, pp. 421-448, May 1887.

[158] H. Hertz, "Die kraft electrischer schwingungen, behandelt nach der maxwell'schen theorie," *Ann. Physik und Chemie (Wiedeman) N. F.*, vol. 36, pp. 1-22, Dec. 1888.

[159] J. Orton, *The story of semiconductors*. 2004, Oxford, England: Oxford University Press.

[160] G. Marconi, "Signals across the atlantic," *Elec. World*, vol. 38, pp. 1023-1025, Dec. 1901.

[161] F. J. Agee, C. E. Baum, W. D. Prather, J. M. Lehr, J. P. O'Loughlin, J. W. Burger, J. S. H. Schoenberg, D. W. Scholfield, R. J. Torres, J. P. Hull, and J. A. Gaudet, "Ultra-wideband transmitter research," *IEEE Transactions on Plasma Science*, vol. 26, no. 3, pp. 860-873, June 1998.

[162] W. D. Prather, C. E. Baum, J. M. Lehr, J. P. O'Loughlin, S. Tyo, J. S. H. Schoenberg, R. J. Torres, T. C. Tran, D. W. Scholfield, J. A. Gaudet, and J. W. Burger, "Ultra-wideband source and antenna research," *IEEE Transactions on Plasma Science*, vol. 28, no. 5, pp. 1624-1630, Oct. 2000.